Characterisation of Vanadium Species in Zeotypes for Redox Applications

Katrine Lie Bøyesen

Acknowledgements

The work on this Master thesis has been carried out at the Department of Chemistry at the Norwegian Unversity of Science and Technology, NTNU. I would like to acknowledge NTNU and the Norwegian Research Council for grants supporting the Swiss-Norwegian Beamlines (SNBL) and MaxLab. I would like to thank my two supervisors Prof. David G. Nicholson and Dr. Karina Mathisen for all of the support given to me through these two years. Prof. David G. Nicholson has always shown enthusiasm for my work and encouraged me to be ambitous ("think like a man"). Dr. Karina Mathisen for motivating and inspire me to always do my best. She has shown me the way of the scientific life, for instance one should always go to the pub when you have beamtime. (Everything are attempted solved after a couple of beers, even quadrupole transitions)

I would also like to thank Dr. Michael Stockenhuber from the University of Newcastle, for letting me come to Australia and do activity measurements. The staff at SNBL has also been very cooperative, even though vanadium can be a pain in the ass. Escpecially Wouter van der Beek for helping me with Raman, and Dr. Olga Safonova for coming up with the great idea that was the start of the second part of my master thesis, over a lunch in the cafeteria. Dr. Florian Meneau for helping us with beamtime difficulties. Syverin Lierhagen for helping me with ICP-MS is also much appreciated. Thanks to Camilla Nordhei for helping me with the start problems in Athena and Excurve, and for always being talkative in the hallway, when it was a great need of a break. A thanks to Gunnar who let me take the Jones

reductor to Grenoble, and helping me with the reduction of vanadium. A special thanks to Christer Løpstad for helping me with mass spectrometer issues.

Also a special thanks to my collegues in my research group, Mari T, Tina, Beate, Anlaug, Asmira and Mari N. I would never have thought doing my masters would be this fun. We have helped eachother during the exams and the finishing stage of our thesis. Thank you for doing these two years interesting and motivating. I would escpecially like to acknowledge my fellow students who have been with me from the start: Mari, Tina and Christina. I will never forget my great student years, and I shall always treasure our friendship.

Thanks to my parents and my sister for supporting me, even though they did not always understand what I was doing. They have always said as long as you do your best, nobody demands anything more. And last, but not least I would like to thank Jacob. I would not have made this without your support. Thank you for listening when I rehearsed my talks (and learning a bit about EXAFS yourself), for being patient when I got a bit preoccupied with the world of vanadium, you always managed to pull me back to reality.

Trondheim, May 2009.

Katrine Lie Bøyesen

Abstract

This thesis is divided into two parts. The first part is concerned with the synthesis and characterisation of VAPO-5 and VAPSO-5 for redox applications. Synthesis parameters were investigated in order to achieve optimal conditions. The effect of different structure directing agents (templates), various vanadium sources, different crystallisation times have been investigated. Aluminiumphosphates are microporous materials, and exhibit molecular sieving properties. The introduction of vanadium to the framework might create and acid site, which could lead to acid catalysis. Vanadium has also interesting redox properties, as it posess 5 oxidation states. Thereby with the molecular sieving properties of the support, a possible acid site, and the redox properties of vanadium, VAPO-5 and VAPSO-5 could be a possible bifunctional catalyst. A structural study on the materials have also been done, mainly using EXAFS and *in situ* XANES complementary. Activity measurements was done on the reduction of NOx, using propene as the reducing agent in an oxygen rich atmosphere.

In situ XANES studies was done to study the redox properties of VAPO/VAPSO-5. The *in situ* studies of VAPO-5 and VAPSO-5 did not reveal a pronounced reduction in the valence state in the presence of propene and oxygen. There was a change in the coordination number, thereby a change in the local geometry of vanadium. The activity measurements revealed very low activity towards the reduction of NOx in the presence of propene and oxygen, which can be explained by the *in situ* results.

The second part of this thesis is concerned with the deposition if vanadium pentoxide particles (V_2O_5-particles) onto microporous materials. H-ZSM-5 and H-Y were investigate for the selective oxidation of propene for the production of acrolein with *in situ* XANES. It has recently been a lot of focus on more efficient and envrionmentally friendly catalysts. Products from selective oxidation of hydrocarbons represents 24% of the most important industrial organic chemicals and intermediates used in manufacture of industrial products. H-ZSM-5 and H-Y with V_2O_5-particles have been ion enxchanged by regulating the pH and vanadia loading.

A combined Raman/XANES *in situ* study was done for the V_2O_5 particles. Mass spectra, Raman and XANES data were collected simultaneously. Mass spectra revealed the formation of acrolein, over V_2O_5/ZSM-5, however the formation of acrolein was not detected over V_2O_5/Y. A redox mechanism has been proposed for the oxidation of propene over V_2O_5/ZSM-5 and V_2O_5/Y.

Contents

Chapter 1

Theory

1.1 The origin of vanadium as catalyst

Vanadium is used as catalyst for several reactions. It is escpecially regarded as an oxidation catalyst for different organic reactions such as: Sulphur dioxide to trioxide, the sulphonation of aromatic hydrocarbons and the reduction of olefins.[1]Vanadium pentoxide (V_2O_5) on titania (TiO_2) is used as a catalyst for the reduction of NOx with ammonia as the reducing agent for stationary systems.[2] Vanadium and especially vanadium pentoxide is a good oxidation catalyst as it reversibly loses oxygen upon heating, thereby vanadium is able to participate in redox reactions.

Many transition metals have been incorporated into the framework of AlPO-n and SAPO-n.[3] By introding vanadium into the framwork, it could be a potensial bifunctional catalyst. The AlPO-n with its molecular siveing properties and vanadium with its catalytic properties. With the incorporation of vanadium it is suspected that vanadium will create acid sites and thereby there is a potential of acid catalysis, redox mechanisms and shape selectivity (due to the AlPO-n structural properties) for the desired products. The introduction of vanadium into AlPO-5 molecular sieves to form VAPO-5 and VAPSO-5 show special catalytic properties in the selective oxidation of hydrocarbons.[4] The catalytic properies of transition metal ion incorporated into molecular sieves are strongly dependent on the natur and location of the metal ions and their accessibitlity to and coordination with adsorbate molecules.[4] VAPO-5 has been found to catalyse oxidation reactions with tert-butyl hydroperoxide such as epoxidation of allylic alkohols, and oxidations

of aromatic compounds.[3]

1.2 Selective catalytic reduction of NOx[5]

Emissions of nitrogen oxides (NOx) are a problem globally. This issue is now becoming more important. The reason for this is the lean-burn technology which is now used in diesel powered cars. These cars operate in excess oxygen atmosphere, and are efficient in the conversion of carbon monoxide (CO) to carbon dioxide (CO_2). Unfortunately these lean-burn processes do not convert NOx, which is a growing problem environmentally and socially. For lean-burn engines there is a lot of research to find efficient and environmentally friendly catalysts. The U.S. Environmental Protection Agency (EPA) has as one of their main tasks to reduce the emissions of NOx. There are several health-related hazards concerning NOx emissions. Smog is formed when NOx and volatile compounds react in the presence of heat and sunlight. This can lead to damages in the lung tissue and reduced lung capacity; this is in particular for those with already problems with their respiratory system. In addition smog can be easily transported with the wind, which makes the danger real also for those not near the NOx emission. NOx also reacts with ammonia, moisture and other compounds to form nitric acid vapour and particles. These particles could lead to damages on the respiratory system if they are inhaled. Acid rain arises when NOx and sulphur dioxide (SO_2) reacts with other substances in the air and forms acid rain. Acid rain damages forests, cars and rivers. N_2O, which is a greenhouse gas, is emitted to the atmosphere, which leads to climate changes in the long run.[6]

In 1999 the Gøteborg protocol was signed. It is an international collaboration between several European countries including the U.S. The Gøteborg protocol became operative in 2005, and engaged the countries to reduce emissions of sulphur oxides, nitrogen oxides, ammonia and volatile compounds in 2010. In 1999 the emission of NOx was 219 000 ton, after restrictions from the protocol it was supposed to be 156 000 ton. In 2007 the emissions was reduced to 190 000 ton, which states that we have not yet reached the goal.[7]

Selective catalytic reduction of NOx with hydrocarbons has received a lot

of attention, as mentioned, because of the lean-burn processes.[8] There has also been a lot of research on the catalytic reduction using ammonia as the reducing agent. However for mobile units it is unpractical with an ammonia tank and it is also a risk for ammonia leakage. The advantage of using hydrocarbon is that hydrocarbons only react with nitrogen oxides, instead of oxygen.[9]

1.3 Selective Oxidation of Hydrocarbons

1.3.1 Introduction

There have recently been a lot of focus on more efficient and environmental friendly catalysts,which has given a demand for good catalysts. Products from selective oxidation of hydrocarbons represents 24% of the most important industrial organic chemicals and intermediates used in manufacture of industrial products. The products include intermediates such as acrolein, acrylic acid, acrylnitrile, methacrylic acid, MTBE, maleic anhydride, phtalic anhydride, ethylene and propene oxide.[10].

Catalysts for selective oxidation of unsaturated hydrocarbons need to follow certain criteria. Firstly it is important to supply a limited amount of oxygen to the reactant. It need only be enough for the reaction to happen, but not that much that complete oxidation occurs. Secondly the catalysts need suitable sites for adsorption of hydrocarbons in deformed reactive state. Third the catalysts should be able to transfer electrons from and to the reactants.[11]

The selectivity is defined as the ratio between the desired product formed, and the amount of converted reactant.[12] The selectivity is very much dependent on the reaction conditions, structure of the catalyst, support and the promoters.[11]

1.3.2 The Redox Cycle and Lewis acid-base[11]

The oxidation of hydrocarbons generally follows the Mars van Krevelen model. The model suggested by Mars van Krevelen states that the catalytic reaction consist of two steps:

1. The reaction between the oxidised catalyst and the hydrocarbon (R) which reduces the catalyst:

$$cat \times O + R \rightarrow RO + cat \tag{1.1}$$

2. Oxidation of reduced oxide with gas phase oxygen:

$$2cat + O_2 \rightarrow 2cat - O \tag{1.2}$$

For combined metal oxides as catalyst,this redox cycle is model of how the selective oxidation occurs.The reactant hydrocarbon is adsorbed on an metal ion site to form chemisorbed species. These adsorbed species reacts with lattice oxygen that is associated with the $M_1{}^{n+}$ site. This gives partially oxidised products. The lattice oxygen, from a neighbouring site $M_2{}^{m+}$, moves to the oxygen vacancy on $M_1{}^{n+}$. At the same time electrons that are produced at $M_1{}^{n+}$ are transported to $M_2{}^{m+}$. Molecular oxygen can be adsorbed on $M_2{}^{m+}$ site where it is converted to lattice oxygen. The redox cycle depends on the ability of the catalyst surface sites to accept and donate electrons. This is quite similar to Lewis acid and base theory. A Lewis acid is an electron pair acceptor, and a Lewis base is an electron pair donor.[13] The Lewis acid strength of a catalyst depends on its ability to convert a basic reactant to the corresponding acid through electron transfer. Similar with Lewis basic strength which depends upon its ability to convert an acid to the corresponding base through electron transfer. The partial oxidation reaction also depends on the nature of the reactant.

1.3.3 Selective oxidation of Propene

The mechanism of selective oxidation of propene and propane to oxygenates have been much studies in the recent years. Oxygenates refers to compounds which contain oxygen. Most oxygenates are used in gasoline as additives to reduce carbon monoxide which is created when the fuel is burned. It is mostly the products acrolein, acrynitrile and acrylic acid which is of interest.[10,11,14,15,16] It has been escpecially important to study the possibility to convert propane directly to oxygenates. This is because the products mentioned above are produced from propane in a two step process via propene. The high cost of production of propene make it more attractive to produce oxygenates from propane.[15] Different catalysts have been used for oxidation of propene, for instance BiMoO, SbSnO, Cu_2O, CoMoTeO, NiMOTeO, VPTeO and recently V_2O_5/Nb_2O_5.[15,14].

Nanoparticles of V_2O_5 on various micro and mesoporous supports have been reported to exhibit activity for the oxidation of propene.[16,17] Previous studies have revealed that different VOx species are formed depending on both the method of deposition, parent material and vanadia loading.[18,2]

The selective oxidation of propene follows a Langmuir-Hinshelwood mechanism during the dissosiative chemisorption step. Dissosiative chemisorption means that a bond i broken and that the components are bonded weakly to the surface as shown with hydrogen in figure 1.1. The Langmuir Hinshelwood mechanism assumes that the reaction occur between chemisorbed reactants with the surface reaction being the rate limiting step. It has previously been suggested that the the alloxy intermediate(CH_2=$CHCH_2O^*$) is present during the selective oxidation reaction with propene[15]. It was shown recently that the intermediate which is present during propene oxidation is $C_3H_5{}^*$.[14] The elementary reactions for the selective oxidation of propene to acrolein is showed in equation 1.7 to 1.6. The oxygen insertion to the surface allyl intermediate is from the lattice oxygen on the catalyst, and follows a Mars-Van-Krevelen mechanism as described above.

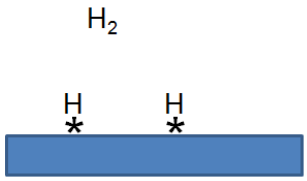

Figure 1.1: Dissosiative chemisorption of hydrogen(H_2)

$$CH_2 = CH - CH_3 + O^* + ^* \rightleftharpoons CH_2 = CH - CH_2^* + HO^* \tag{1.3}$$

$$CH_2 = CH - CH^* + O^* \rightarrow CH_2 = CH - CH^* + OH^* \tag{1.4}$$

$$CH_2 = CH - CH^* + O^* \rightarrow CH_2 = CH - CH = O + 2^* \tag{1.5}$$

$$HO^* + HO^* \rightleftharpoons H_2O + O^* + ^* \tag{1.6}$$

$$O_2 + 2^* \rightleftharpoons 2O^* \tag{1.7}$$

Reaction 1.3 shows that propene is reversibly dissociated and chemisorbed as surface $CH_2CHCH_2{}^*$ and HO^* intermediates. In the next step (1.4) the C-H bond in the allyl intermediate on the surface is broken, followed by the insertion of O^* through lattice oxygen from the catalyst(1.5). In the final step (1.6) the OH^* combine to H_2O.[14] It was found by Zhao*et al* that gas phase oxygen is required to achieve the product acrolein. It is assumed by Zhao *et al* that gas phase oxygen is required to oxidise the surface H^* to H_2O to prevent the reversible hydrogenation of surface $C_3H_5{}^*$ intermediate back to propene. Figure 1.2 shows an illustration of the reaction mechanisms:

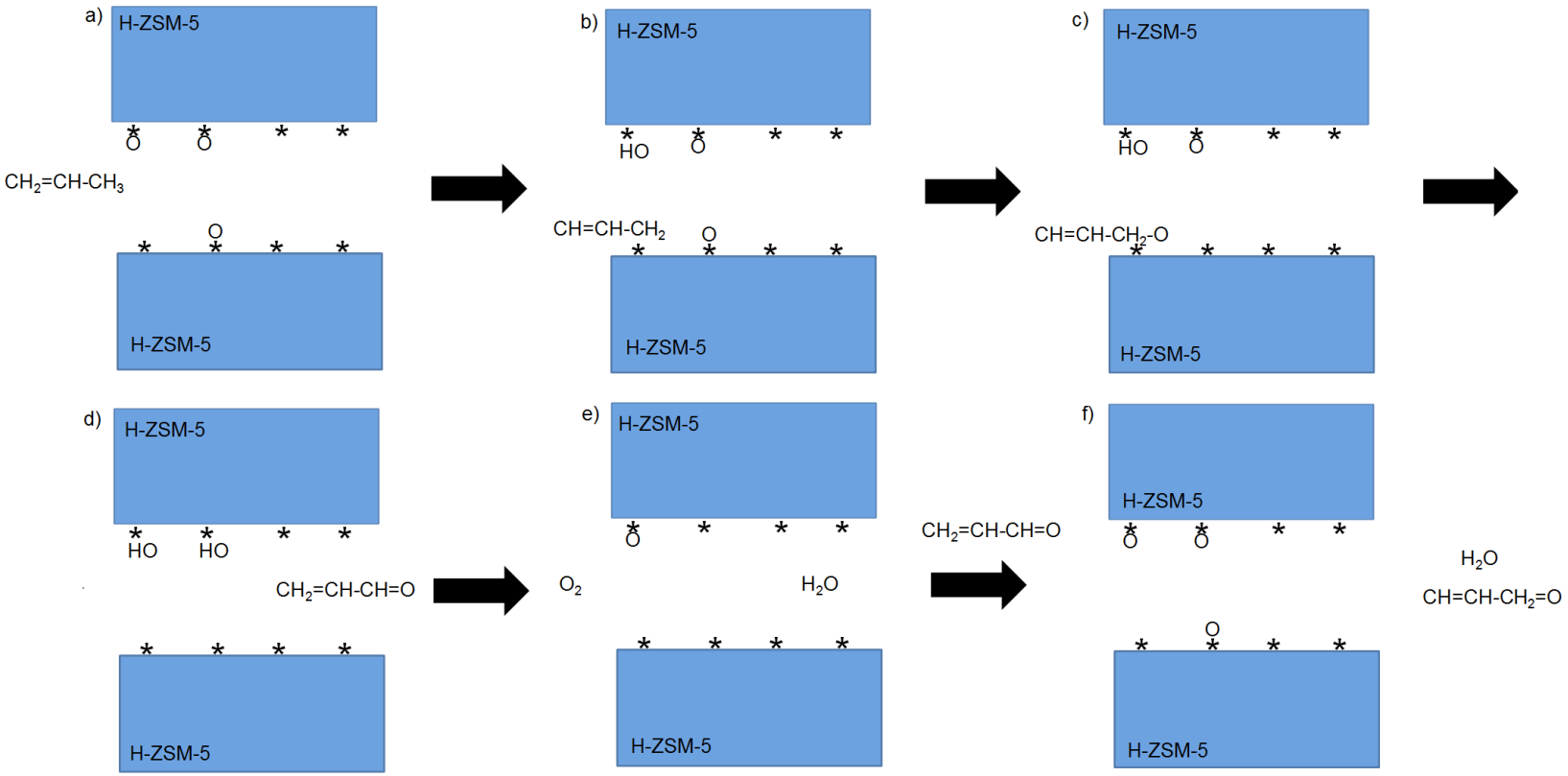

Figure 1.2: A suggestion for the reaction mechanism which occurs on the zeolite in which the vanadium species are the active site and are represented by *. a)Propene enters the H-ZSM-5 b)the formation of surface allyl species and an hydroxyl group, c) the insertion of an O* surface species, d)Extraction of another hydrogen to form a hydroxyl group and acrolein is formed and desorps from the surface, e) The two hydroxyl groups recombine and form water, f) The reduced surface vanadium is reoxidised.

1.4 Microporous Materials[19]

Microporous materials are defined as having a pore size below 20Å. There exist a lot of work to synthesise microporous materials with large pore size, since most of the microporous materials that exist today have a pore size below 10Å.

The term molecular sieves is often referred to when talking about microporous materials. Molecular sieves is a class of porous material that can distinguish molecules on the basis of size and shape.

Microporous materials are very interesting as they can selectively allow some molecules to enter their pores. This property make microporous materials such as zeolites interesting in catalysis as they can be very selective towards the desired reaction.

There are two important properties of microporous materals: Ion exchange and gas sorption. Ion exchange exchanges ions in the microporous material with the ions in a solution. Gas sorption is the ability of a microporous material to absorb and desorb molecules.

1.4.1 Zeolites[20,21,12,22,23]

The first zeolite was described by the swedish Axel Cronstedt in 1756. The word zeolite has its origin from 2 greek words: zeo and lithos, which means to boil and rock. It exist 34 natural ocurring zeolites, and in the recent years there have been synthesised a great number of zeolites. Natural ocurring zeolites are not interesting in catalytic applications as they contain pollutants such as Fe. Zeolites have three-dimensional structures which is build up by $[SiO_4]^{4-}$ and $[AlO_4]^{5-}$ coordination polyhedra linked by oxygen ions. The framework are very open and contain channels and cavities in which cations and water molecules are located. The cations often have a high degreee of mobility which make it possible with ion exchange, and the water molecules are lost and regained. Ion exchange is a reversible chemical reaction where an ion from a solution is exchanged with an equivalent amount of another ion from the same charge that is attached to an immobilised solid phase, such as naturally ocurring zeolites or synthetic zeolites.

In zeolites the ratio of $[SiO_4]^{4-}$ and $[AlO_4]^{5-}$ is vital. The highest possible amount of Al is limited by the $[AlO_4]^{5-}$ tetrahedra which can only be connected to $[SiO_4]^{4-}$ tetrahedra, and not to eachother. Therefore the lower boundry of the Si/Al ratio is 1. Since Al is trivalent, each $[AlO_4]^{5-}$ tetrahedra receives an excess of negative charge, which needs to be compensated by a cation. The unit cell in a zeolite can be described by equation 1.8:

$$M_x^{n+}/[(AlO_2^-)_x(SiO_2^-)_y]nH_2O \tag{1.8}$$

The M^{n+} is the cation which compensate for the negative charge. By removing the water in the zeolite structure, the cavities are formed, in which the reaction can progress.

Zeolites are usually referred to as molecular sieves. Only molecules that are smaller than the pore opening can be transported into the cavity. Zeolites are interesting in catalysis for several factors:

- Zeolites have micropores and cavitites, thereby they posess shape selective properties
- Zeolies are more acdic than silica alumina
- Different metals can be ion exchanged into the structure as the $[AlO_4]^{5-}$ tetrahedra are in need of a positive charge
- Zeolites can also be used as support for metals or metal oxides, thereby be a bifunctional catalyst

Zeolites are as mentioned shape selective, because of their well defined pore size. They posess reactant selectivity, product selectivity and transition state selectivity. These are shown in figure 1.3 below:

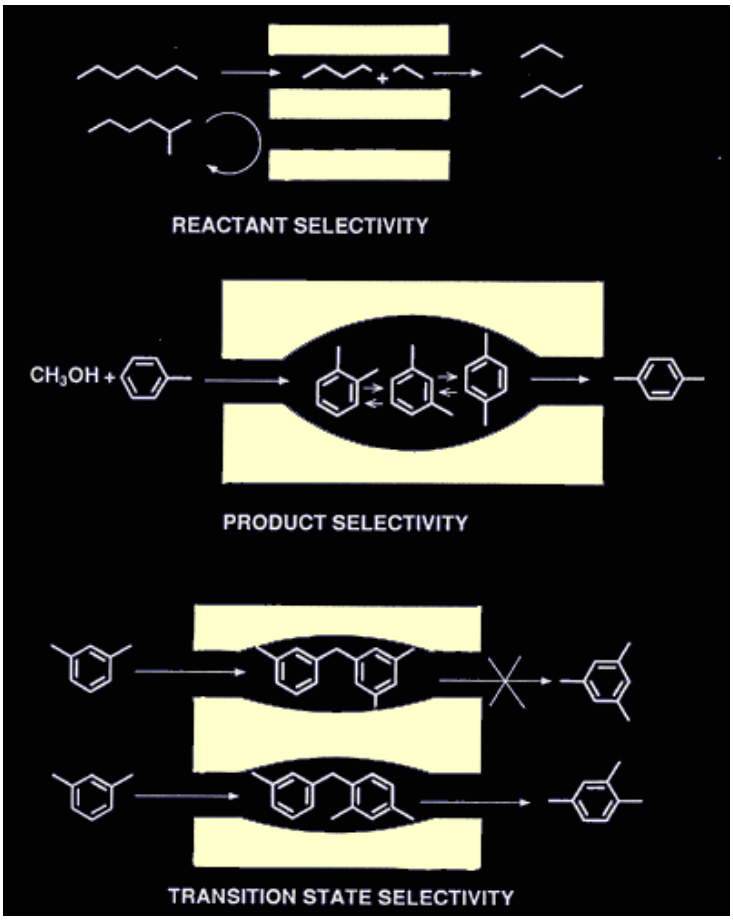

Figure 1.3: The shape selective properties of zeolites

Reactant selectivity occurs when the pore opening is so small that only small reactant molecules can be transported into the structure, as the bigger molecules are prevented. Product selectivity ocurrs when only one of many possible products can be transported out of the zeolite. The transition state selectivity is when it is not enough space for a transition state in a catalytic elementary reaction to form.

In this thesis the two zeolites H-ZSM-5 and H-Y are used. H-ZSM-5 was first synthesised in 1967, and was applied to numerous refining and petrochemical processes. In ZSM-5 there are two pore systems, one consisting of zig-zag channels of near-circular cross-section and another of straight channels of elliptical shape. All the intersections of ZSM-5 are of the same size. The

zeolite has low aluminium content, and the water content is low. Zeolite Y has has a tree dimensional structure as opposed fo ZSM-5 which is 2D. The pore diameter is large at 7.4Å. The zeolite has a so called supercage in the center. Figure 1.4 show the poretructure of ZSM-5

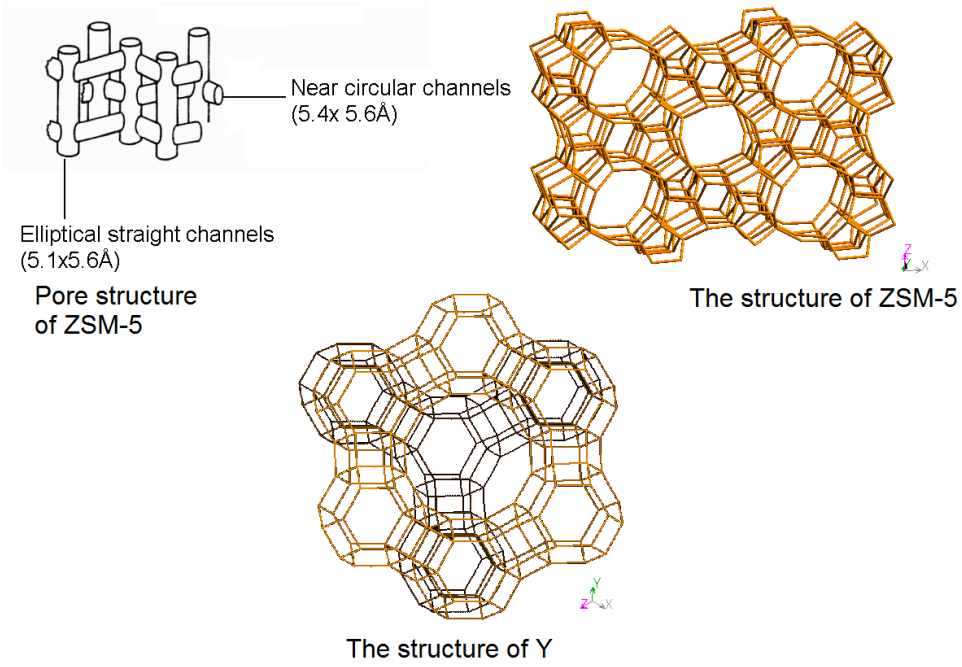

Figure 1.4: The zeolites ZSM-5 and Y.[24, 22]

1.4.2 Aluminiumphosphates, AlPO-n[3,4]

Aluminiumphosphate, AlPO-n,and aluminiumsiloconphosphate, SAPO-n, are microporous crystalline materials. It is important to point out that AlPO-5 is not a zeolite, as zeolites only have Al and Si as lattice atoms. A general term for zeolites and aluminumphosphates is zeotypes.

The framework of AlPO-5 is neutral. By replacing some phosphorous with silicon in the neutral framework in AlPO materials, produces SAPO materials with a negative framework charge. Transition metals can also be incorporated into the lattice og AlPO-5 and SAPO-5, these are metals like Ti, V, Cr, Mn, Fe, Co, Ni, Cu, Zn. As for the incorporation of silicon to AlPO-5, the transition metal will introduce a negative charge to the framework, as shown in figure **??** A metal can be ion exchanged with SAPO-5 as it has a negative charge. The difference with ion exchange and the incorporation of a metal is that by incorporating a metal, the metal is introduced into the framework. When a metal is ion exchanged the metal stays at the surface of the zeotype or zeolite.

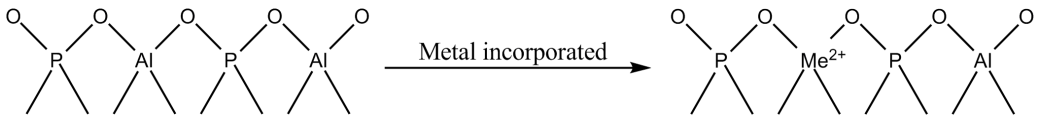

Figure 1.5: A divalent metal is incorporated and the framework becomes negative

The AlPO-5 and SAPO-5 molecular sieves are composed by a 4 ring, 6 ring, and 12 ring straight channels which are interconnected by 6 ring windows as shown in figure 1.6

The main channels of this structure type are nearly circular and have a diameter of 0.73nm. This type of structure is called the AFI structure and is characterised as having large pores. As a comparison the AlPO and SAPO-34 have a pore diameter of 0.38nm. These large pores in the AFI structure gives the AlPO/SAPO-5 av very large inner surface. Which means that these microprous materials could be interesting in catalytic reactions. The

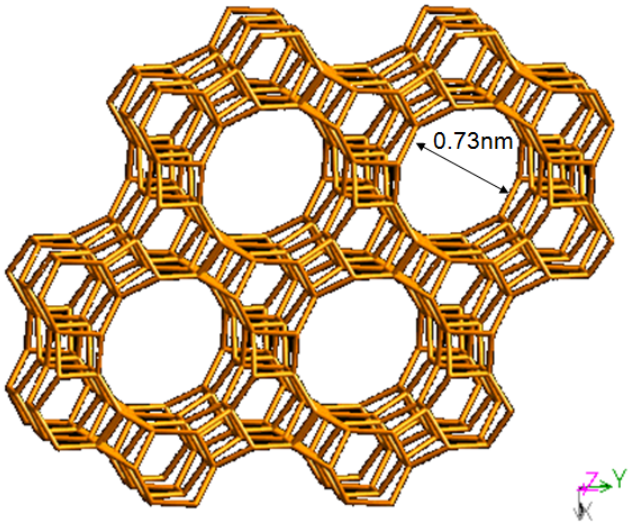

Figure 1.6: The AFI structure of AlPO-5.[22]

AlPO-5 in itself has structural properties which is interesting in catalysis, but incorporation of a metal may lead to acid sites. The molecular sieving properties of the AlPO-5 and the inctroduction of acid sites will possibly make the MeAlPO-5 a bifunctional catalyst. By EXAFS it might be possible to distinguish where the vanadium is incorporated, if phosphorous or aluminium are detected in outer shells. This is ascribed to Löwensteins rule which exludes Al-O-Al linkages. Thereby if aluminium is detected in outer shells, the vanadium subtitutes phosphorous and vice versa.[20]

1.5 Crystal field theory[13]

The crystal field theory is used to explain optical spectra, thermodynamic stability and magnetic properties of transition complexes. The crystal field theory treat the ligand as a negative point charge, which can lead to the splitting of orbitals. It is important to discuss this theory because vanadium is a d-block metal and the splitting of orbitals occurs when vanadium forms different complexes. It is also important to understand the different colors in the various vanadium oxidation states. The different d-orbitals are illustrated in 1.7 below:

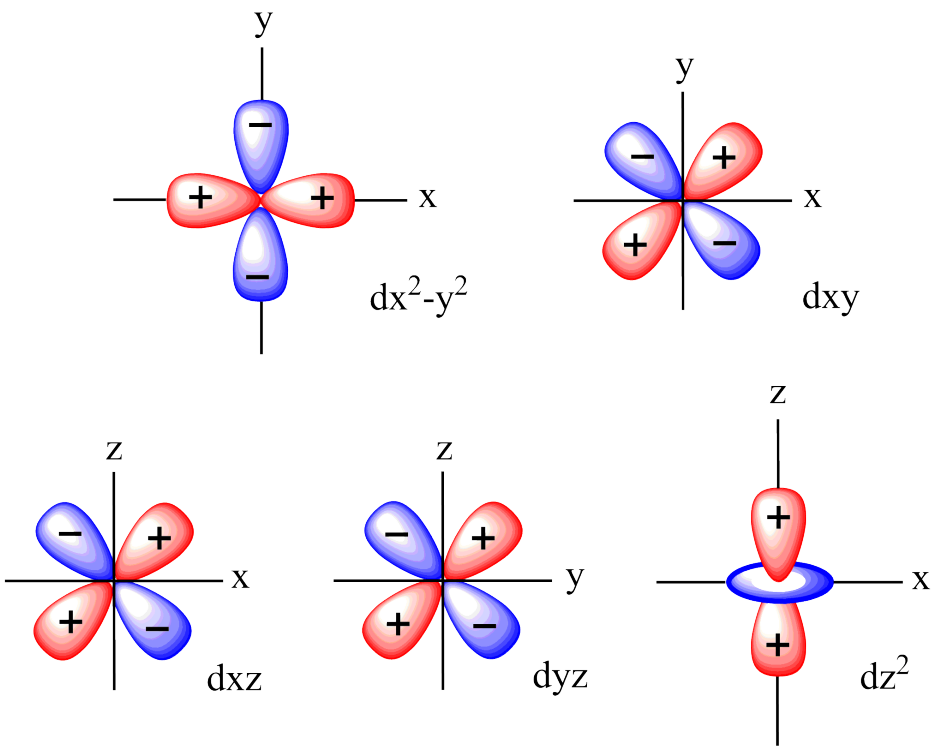

Figure 1.7: The five different d-orbitals

Octahedral field

In an octahedral field the ligand approaches the central atom in the d-orbital along its axis. As mentioned the crystal field theory considers the ligand as a negative point charge, and then the central atom and the ligand will repel each other. This causes a splitting in energies in the various d-orbitals, and gives repulsion between the different d-orbitals as shown in figure 1.8

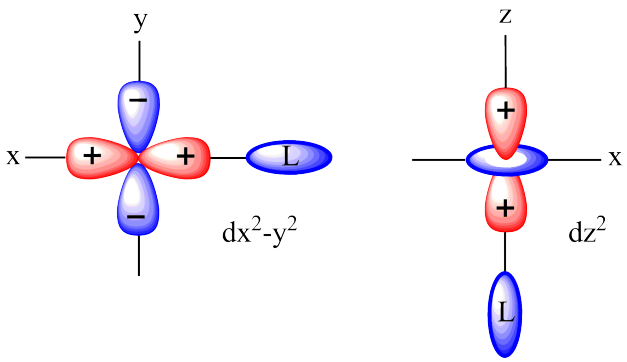

Figure 1.8: The negative ligand,L,approaches the d-orbitals at the axis, and this causes repulsion

The splitting of the orbitals is shown in figure 1.9

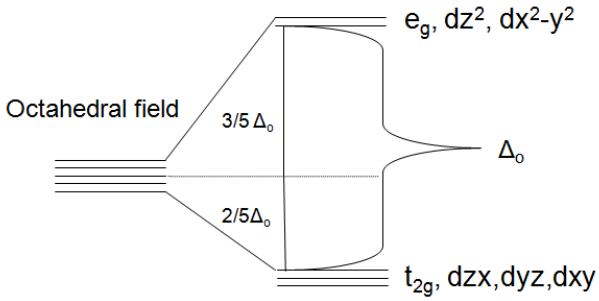

Figure 1.9: An illustration of the splitting that occurs when a ligand is repulsed by the central atom in an octahedral field

The Δ_o is the ligand field splitting parameter. It is only the two d-orbitals dz^2 and dx^2-y^2 that repels the ligand, since these orbitals are along the axis. That is why these orbitals have higher energies, eg, and dxy, dzy and dxz have lower energy, t_2g.

It should also be stated that the interaction with the electrons in the d-orbital depends on the ligand strength. The subsequent line is called the spectrochemical series. The ligands are here ordered after increasing energy of transitions that occur when they are present:I^-<Br^-<SCN^-<Cl^-<$NO_2{}^-$<N3−<F^- <OH^-<$C_2O_4{}^2-$<H_2O<NCS^-<CH_3CN<py<NH_3<en<bypy<phen<$NO_2{}^-$ <PPh_3<CN^-<CO. The crystal field theory cannot explain these ligand strengths alone, but the ligand field theory explains this phenomena.

The ligand field strength also depends on the identity of the metal ion. The order is as follows:
Mn^{2+}<Ni^{2+}<Co^{2+}<Fe^{2+}<V^{2+}<Fe^{3+}<Co^{3+}<Mo^{3+}<Rh^{3+}<Ru^{3+}<Pd^{4+}<Ir^{3+} <Pt^{4+} Value of the ligand field splitting parameter, Δ_o, increases with increasing oxidation state of the central atom. This is because with higher oxidation state the central metal ions are smaller, and then the interaction with the ligands increases.

Tetrahedral field

In a tetrahedral field, the ligands does not approach the central atom along the axis. Therefore in a tetrahedral field dxy,dxz and dyz is repelled by the ligand. This is shown in figure 1.10.The other d-orbitals dx^2-y^2 and dz^2 will not be repelled since the orbitals are along the axis. The d^3 orbitals favour

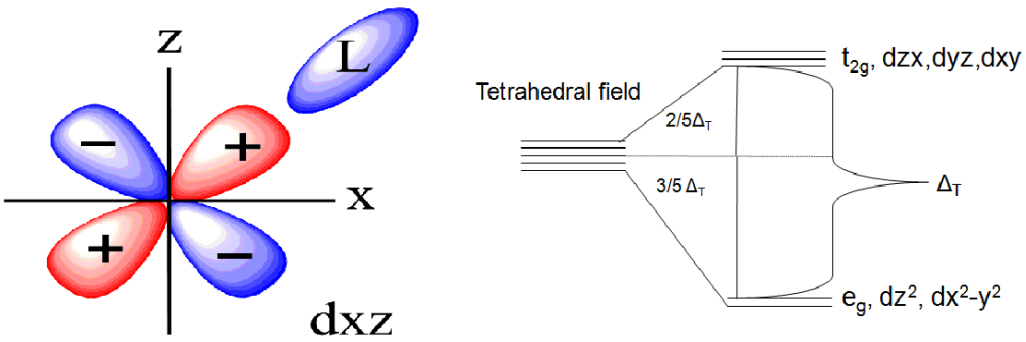

Figure 1.10: The splitting of orbitals in a tetrahedral field. The dz^2 and dx^2-y^2 is stabilised and dzx, dyz and dxy is destabilised.

octahedral fields because the ligand field stabilisation energies are higher for a octahedral structure. Although V^{2+} favour tetrahedral coordination in complexes with halides.

Colours as a result of splitting of orbitals

The crystal field theory is used to explain colours in various complexes. This theory can also be used to explain the different colours in the different oxidation states of vanadium. The splitting parameter Δo is in the order of visible light, hence various colours are observed in different complexes. A photon ejects an electron from t_{2g} to e_g as shown in figure 1.11. This electron absorbs some of the energy and the complementary colour is observed. There are some complexes like manganese(V) which has a weak colour. This is because the transition is spin forbidden, which means that the electron needs to change its spin in order to excite from $t_{2g} \rightarrow e_g$. Electrons have a spin of $\pm \frac{1}{2}$, and the electromagnetic field of the incident radiation cannot change the relative orientations of the spins of electrons in a complex, hence the transition becomes weak.[13]

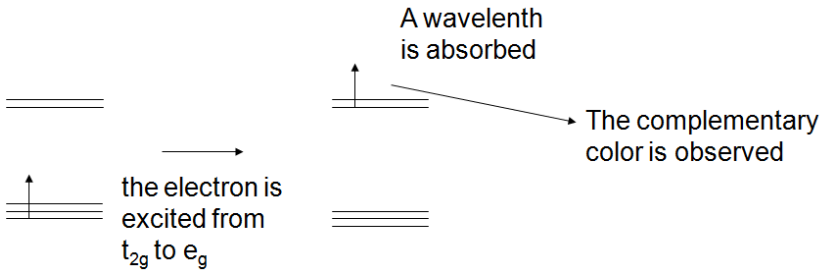

Figure 1.11: The excitation caused by a photon with a certain wavelength causes the different colours that is observed. Here V(IV) is used as an example, the colour that is observed is blue and the wavelength that is absorbed is then the complementary colour orange.

For vanadium in its highest oxidation state, V(V) with a low filled d-orbital (d^0), a charge transfer between the ligand and the metal occurs. Charge transfer bands in the visible region of the spectrum, a reason for the yellow colour in V(V), is a consequence of the lone pairs on the ligand, or if the metal

atom has low lying empty orbitals. Both of these phenomena is evident in the V(V) complex in water where it is apparent as $[VO_2(H_2O)_4]^+$. In this complex the V(V) has a d^0 configuration and exhibit acceptor properties, also the oxygen ligand has lone pairs and is very close to the vanadium atom because of the double bond with oxygen, which will be described in more detail under subsection 1.6. The oxygen transfer electrons to the vanadium atom, as shown in figure 1.12[13]:

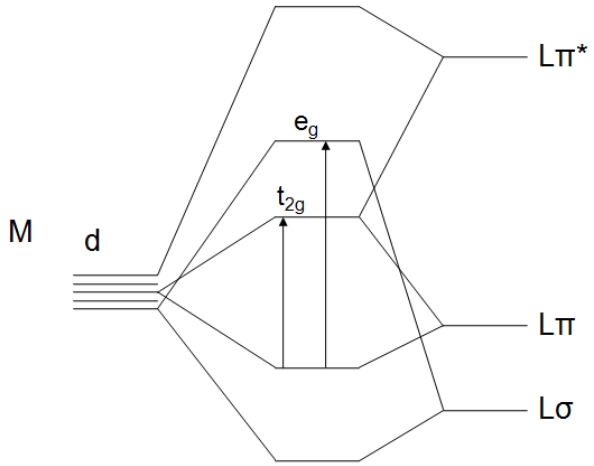

Figure 1.12: The ligand to metal charge transfer transitions that can occur when vanadium recieves an electron from oxygen. Thereby two transitions can occur. A transition to t_{2g} or a transition to e_g. As the oxygen is bonded to vanadium through a double bond, it is the π-bond that participates in the charge transfer. The σ-bond is when the electrons are mainly on the ligand.The antibonded π^* is when there are a metal to ligand charge transfer, which is not present in V(V)

The electrons can be excited to t_{2g} or e_g from the oxygen ligand to the vanadium atom. To explain the pale yellow colour observed in $[VO_2(H_2O)_4]^+$ the electrons will excite from the oxygen ligand to e_g in which a wavelength corresponding to the colour violet is absorbed and yellow is observed.

1.6 The chemistry of vanadium

Vanadyl sulphate is the most common vanadium source in the synthesis of VAPO-5 and VAPSO-5.[4,25,26,27] It has a chain of VO_6 octahdra cross-linked by SO_4 octahedra. Although is does not have perfect octahedral structure, because of the shorter bonding distance with the one oxygen as shown in figure 1.13. When $VOSO_4$ is dissolved in water the vanadyl ions (VO^{2+}) are

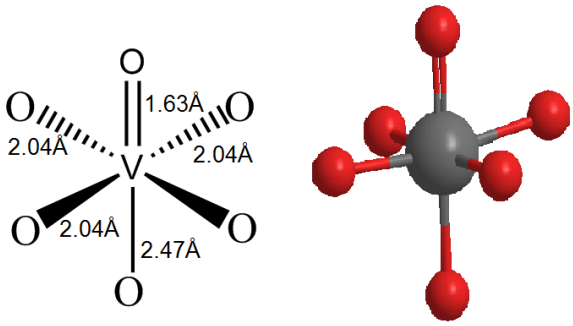

Figure 1.13: The structure of $VOSO_4$ and the corresponding 3D structure. The bond lengths of the four V-O are equal.

surrounded by water molecules which experiences compressed C_{4v} symmetry due to the loss of horisontal mirror plane when one of the axial bonds are shortened, and the other is lengthen.[28],as shown in figure 1.14. The Jahn-Teller effect is when for instance d^9 complexes depart from octahedral symmetry and show tetragonal distortions. These distortions are a result of the Jahn-Teller effect, when a non linear complex in the ground state is orbitally degenerate, and filled asymmetrically. The complex distorts to remove the degeneracy and lower the overall energy of the complex. Compressed C_{4v} symmetry experiences the opposite, the bonding in a octahedral complex is compressed with the double bond of the vanadium atom to the oxygen atom, which leads to C_{4v} symmetry. As a result the symmetry is lowered from octahedral symmetry to C_{4v} symmetry, and decrease in overall energy. The Jahn-Teller effect and compressed C_{4v} symmetry is illustrated in figure 1.15. Vanadyl complexes does generally contain four additional ligands and are square pyramidal. Many of these d^1 complexes are blue due to the

d-d transition which is spin allowed. The vanadyl ion may take on a weakly bond sixth ligand trans to the oxo ligand and is denoted $[VO(H_2O)_5]^{2+}$. The 3d π-orbital on vanadium is bonded to the 2p π-orbital on the oxygen. The oxygen acts as a π-donor which means it donates electrons from the oxide to vanadium.[13]

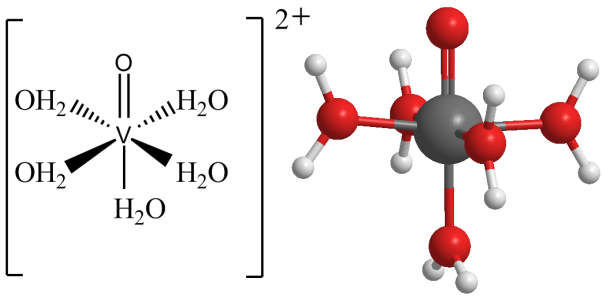

Figure 1.14: The structure of the $[VO(H_2O)_5]^{2+}$ ion and the corresponding 3D structure.

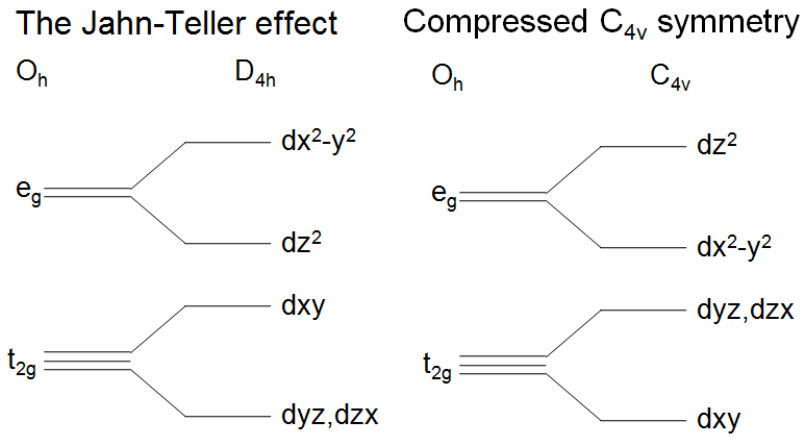

Figure 1.15: The Jahn-Teller effect and reversed Jahn-Teller. Both of them show a stabilisation of the complex and a lowering of the energy

Vanadium pentoxide (V_2O_5) is vanadium in its highest oxidation state (V). It is brick-red and is slightly soluble in water (0.07g/l), but dissolves in both acidic and alkaline environment.[1] The structure of V_2O_5 is shown in figure 1.16 and has a square pyramidal geometry, and a C_s symmetry.[29] The vanadium pentoxide loses oxygen reversibly in the temperature region 700-1125°C, a phenomenom which can account for many of vanadium pentoxide catalytic properties.[1]

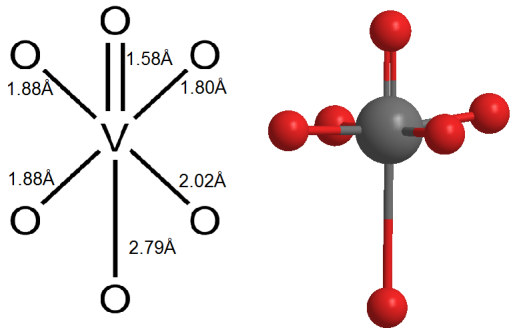

Figure 1.16: The structure of the vanadium in vanadium pentoxide.

When V_2O_5 is dissolved in either acid of base it can form an extensive series of oxo compounds. The simplest complex $[VO_2(H_2O)_4]^+$ exist in acidic solution. This is a pale yellow complex and has a cis geometry. The cis structure is shown in figure 1.17, and is a distorted octahedral geometry with a C_{4v} symmetry. Vanadates are compunds which contains oxoanion of vanadium in oxidation state V. These vanadates are dependent on the pH and the vanadium concentration. When vanadium pentoxide (V_2O_5) is dissolved in strong alkaline solution it forms the $VO_4{}^{3-}$ ion. When the pH is decreased until it becomes acidic, the $VO_2{}^+$ becomes dominant.[1] The different vanadates and their pH dependence are shown in figure 1.18.

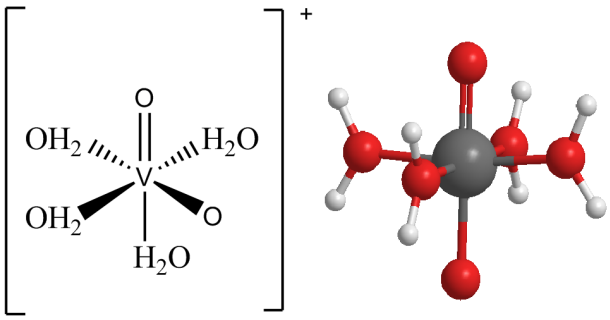

Figure 1.17: The cis structure of $[VO_2(H_2O)_4]^+$ which has a π-bond between one oxygen and vanadium.

When vanadium pentoxide in acidic solution is reduced by zinc and the following redox reaction occurs, as a simplification $[VO_2(H_2O)_4]^+$ will be denoted as the ${VO_2}^+{}_{aq}$ ion and $[VO(H_2O)_5]^{2+}$ is denoted VO^{2+}:

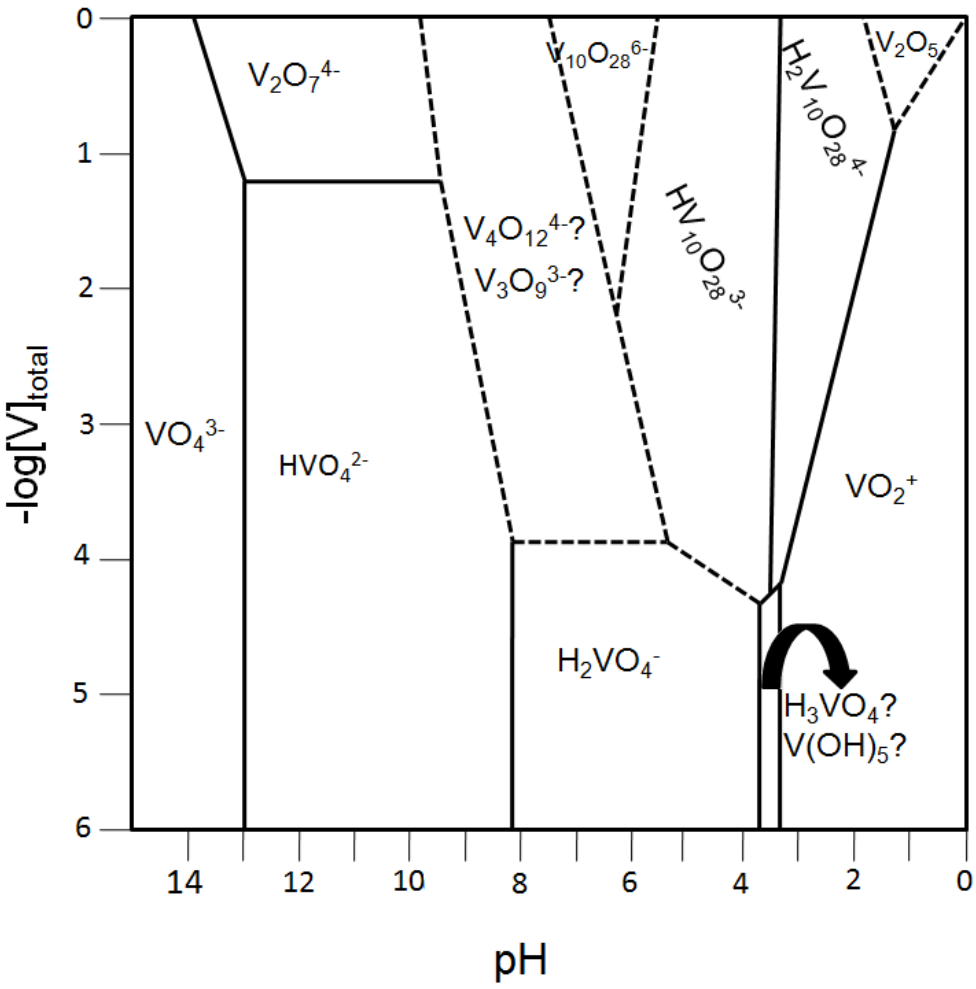

Figure 1.18: The approximate condition of pH and total vanadium concentration under which species would be dominant at the different pH and concentrations at 25°C. Illustration inspired by Comprehensive inorganic chemistry [1]

$$2VO_{2\,(aq)}^{+} + 4H_{(aq)}^{+} + Zn_{(s)} \rightarrow 2VO^{2+} + 2H_2O + Zn_{(aq)}^{2+} \tag{1.9}$$

$$2VO^{2+} + 4H_{(aq)}^{+} + Zn_{(s)} \rightarrow 2V^{3+} + 2H_2O_{(l)} + Zn_{(aq)}^{2+} \tag{1.10}$$

$$2V_{(aq)}^{3+} + Zn_{(s)} \rightarrow 2V^{2+} + Zn_{(aq)}^{2+} \tag{1.11}$$

Equation 1.9 show the reduction of yellow pentavalent solution to tetravalent blue solution. In equation 1.10 the tetravalent vanadium is further reduced to trivalent vanadium which is generally not observed since the next step shown in equation 1.11 happens too quickly.[30] The different oxidation states which appears during the reduction of pentavalent vanadium with zinc is shown i figure 1.19.

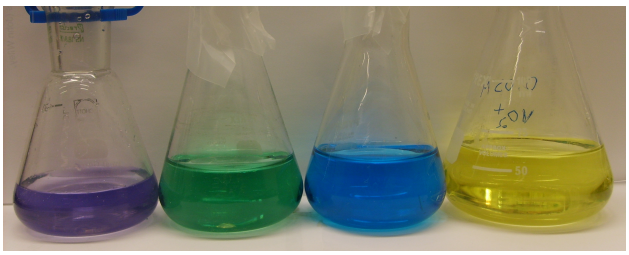

Figure 1.19: The different oxidation states of vanadium in solution. The purple solution is divalent vanadium, the green solution is a mixture of pentavalent an tetravalent solution, the blue solution is tetravalent, the yellow solution is pentavalent.

The divalent vanadium has a perfect octahedral symmetry and the ion in solution is preferably denoted $[V(H_2O)_6]^{2+}$.[30,31] The transition is spin allowed for divalent vanadium, hence the purple color is quite strong. The structure of $[V(H_2O)_6]^{2+}$ is shown in figure 1.20.

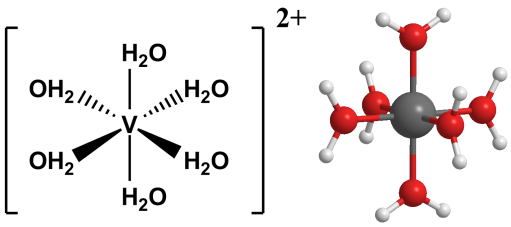

Figure 1.20: The structure of the divalent $[V(H_2O)_6]^{2+}$ ion, and the corresponding 3D structure.

Vanadium monoxide (VO) has a sodium chloride structure and consist of regular octahedral VO_6 units. Hence the symmetry of VO is a perfect octahedra as shown in figure 1.21.[32] The monoxide is formed as a grey, metallic powder by reduction of higher oxides with a number of different reducing agents, most usually with hydrogen.[1]

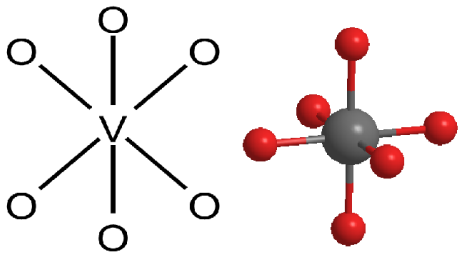

Figure 1.21: The structure and geometry of vanadium monoxide. The figure on the left shows the structure as octahedral in 3D.

1.6.1 Vanadium species in VAPO-5

The structure of the vanadium species have been suggested in several articles. Yu *et al*[4] suggested that vanadium was not incorporated in VAPO-5, but was rather as polymerised vanadate in VAPO-5. As for VAPSO-5 Yu *et al* suggested that vanadium was incorporated into the structure, and that it was bonded tetrahedrally to oxygen. The two models that were suggested in the article are shown in figure 1.22

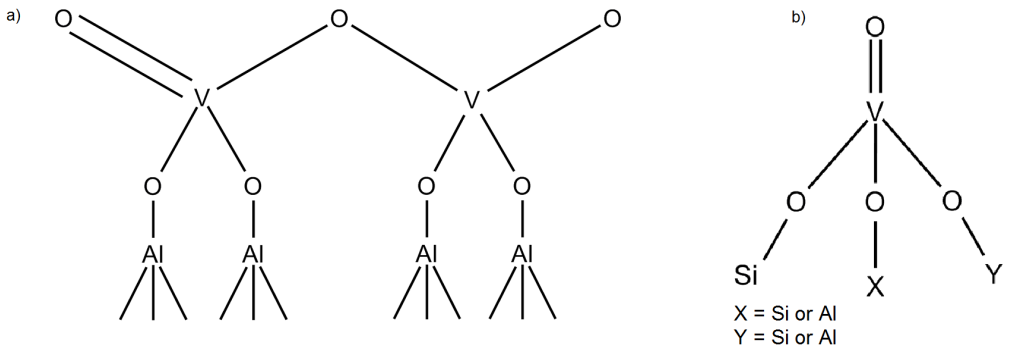

Figure 1.22: An illustration of the vanadium species in VAPO-5 and VAPSO-5, a) is polymerised vanadate in VAPO-5, b) is tetrahedrally coordinated framework vanadium species in VAPSO-5

There are other contradicting models that also suggests where the vanadium is bonded within the framework. Rigutto *et al*[25] suggested that V(IV) substitutes Al(III) which is illustrated in figure 3.24. The basis of their theory is that the composition of VAPO-5 is consistent with vanadium substitution

of aluminum rather than phosphorous.[33]

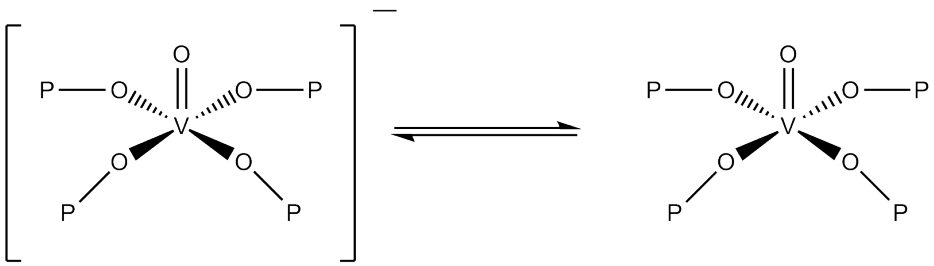

Figure 1.23: This model suggests that V(IV) subsittutes Al(III)

Montes *et al*[34] suggested the opposite that V(V) and or V(IV) substitutes phosphorous P(V) based on EPR and PNMR experimental results, and is shown in figure 1.24

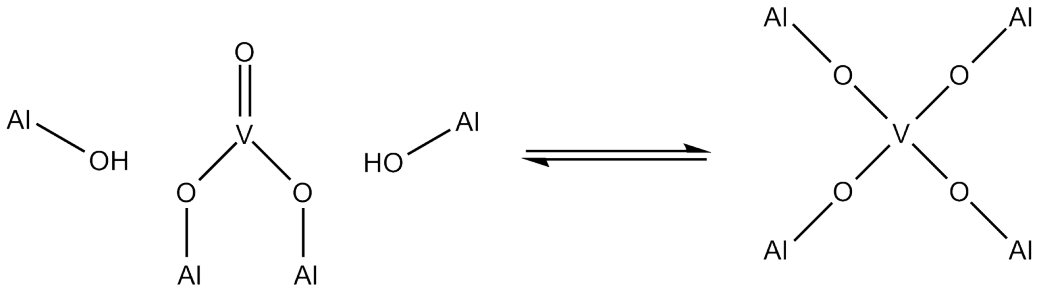

Figure 1.24: Montes et al suggested that V(V) and or V(IV) substitutes P(V)

Chen *et al* states that substitution of either phosphorous or aluminium is possible. Although $(V{=}O)^{2+}$ seems to be bonded to two P sites and two adsorbed template or water molecules. At low vanadium content vanadium is usually incorporated as monomeric vanadyl $(V{=}O)^{2+}$ species of a square pyramidal or distorted octahedra in VAPO-5. The V(IV) could be oxidised to V(V) and then partially reduced back to V(IV). They confirmed this with XANES and EXAFS data.[33] The structure and the oxidation and reduction is shown in figure 1.25

It is still controversial of which model is the accurat one, and this problem will be adressed later in section 3.3.2. The structure of the vanadium species

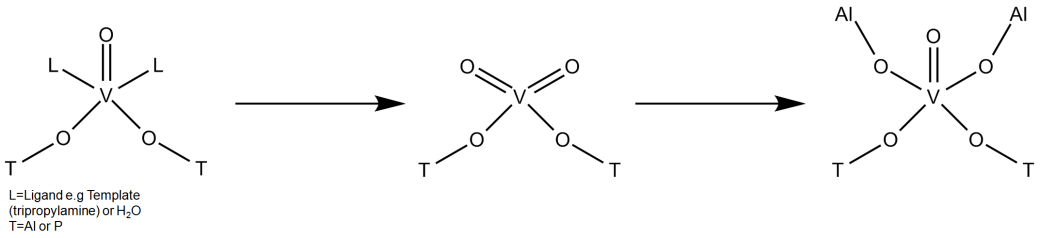

Figure 1.25: The proposed model by Wei *et al* of as synthesised, oxidised and reduced vanadium species in VAPO-5

in VAPO-5 and VAPSO-5 were studied with XAS. Unfortunately it is hard to distinguish aluminium and phosphorous with XAS which will be shown later 3.3.2.

1.7 X-ray diffraction (XRD)[35]

X-ray diffraction is a method that can be used to characterise crystalline inorganic compounds.

X-rays interact with electrons in matter and a beam of X-rays hitting an inorganic material will be scattered in various directions by atomic electrons. If the scattering centers are separated by distances comparable to the wavelength of the X-rays, the interference between the X-rays scattered from particual electron centres can occur.

Distances between atoms or ions in solids are typically a few Ångstroms, which is comparable to the X-ray wavelengts produced by bombardment of metals by electrons.

In this thesis, powder diffraction is used.

1.7.1 Generation of X-rays[35,36]

A beam of electrons striking a metal plate will, provide the electrons that are sufficiently energetic, eject an electron from the metal atom core orbitals. Filling of this hole by electron decay from a higher energy orbital occurs with emission of radiation.

In order to carry out a diffraction experiment a single X-ray wavelength is desired. This may be achieved using a crystal monochromator in which the X-ray beam emerging from the X-ray tube hits on a single crystal at a chosen, fixed orientation. For a particular angle θ and employing Braggs law (seen in equation 1.13), only one wavelength can be diffracted from the crystal. By adjusting θ it is possible to select one wavelength from the X-ray beam, normally the most intense $K_{\alpha 1}$. A second way of removing unwanted wavelengths from the X-ray beam is to use filter. This normally consists of a foil of metal with an atomic number one or two below the targeted metal that of metal used to generate the X-ray spectrum. In the metal of the filter,

transitions between energy levels will require slightly less energy than the corresponding transitions in the metal target due to reduced nuclear charge and this leads to a high adsorption coefficient for these X-rays.

1.7.2 Scattering of X-rays by crystalline solids

A X-ray beam impings a crystal in the powder. The scattering of the impinging X-ray beam from the points A and D in neighbouring planes will produce in phase diffracted X-ray beams (constructive interference) if the additional distance travelled by the X-ray photon scattered from D is an integral number of wavelengths. This path difference BD+DC will depend on the lattice spacing or d_{hkl}, where hkl are the Miller indices for the planes under consideration, and will also be related to the angle of indicence of the X-ray beam,θ. For an integral wavelength pathlength difference, the following relationship can be obtained, which is illustrated in figure 1.26

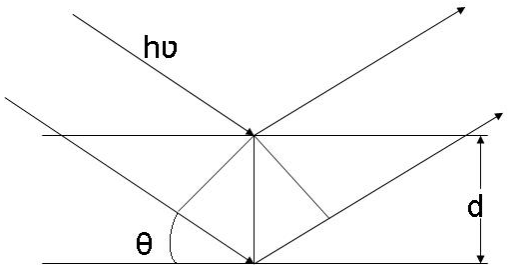

Figure 1.26: When a X-ray beam is diffracted the crystal plane, the relationship between the distance of the crystal planes and the angle of the diffracted beam can be derived.

$$\text{Path difference} = BD + DC = 2d_{hkl}sin\theta = n\lambda \tag{1.12}$$

Where n is an integer and λ is the X-ray wavelength. The Bragg equation is known as:

$$2dsin\theta = n\lambda \tag{1.13}$$

A X-ray beam that is incident on a crystal plane will be diffracted according

to Braggs law. In this thesis powder diffraction is used for phase determination.

1.8 X-ray absorption spectroscopy (XAS)[36,37]

X-ray absorption spectroscopy is a local proping technique, which give information about the local geometry, the valence state and the neighbours of the metal in interest. The spectrum is divided into two parts, the extended X-ray absorption fine structure (EXAFS) and the X-ray absorption near-edge structure (XANES). The absorption edge arises when a X-ray beam sweeps over the sample with increasing energy. When the photon energy is sufficient enough, it will excite the inner electrons which result in what is known as the absorption edge. This absorption edge is different for every element and can be seen as the fingerprint of each element. The K-edge as studied in this thesis is the ionisation of 1s to continuum. To collect absorption data a synchortron source has to be used. Third generation synchrotron sources as the European Synchrotron Radiation Facility (ESRF) and MaxLAb used in this work, provides a higher photon flux than conventional X-ray sources. A high photon flux is makes it possible to obtain a high signal to noise spectrum. Synchrotron radiation is generated when charged particles such as electrons are accelerated with increasing speed in a magnetic field. Figure 1.27 show an illustration of the EXAFS and XANES spectra:

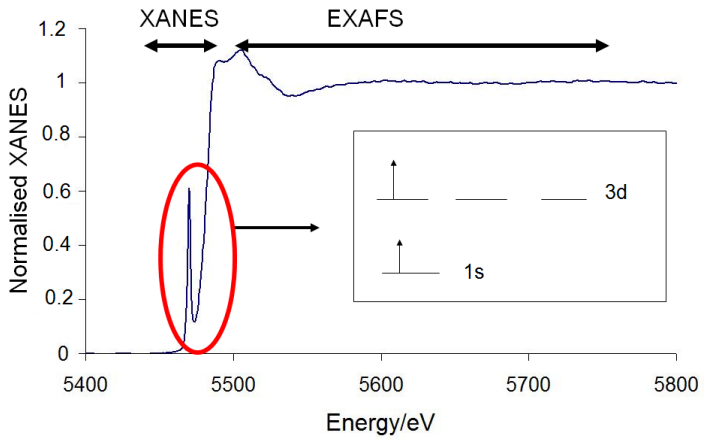

Figure 1.27: The normalised X-ray absorption spectrum. The pre-edge is considered in the XANES, and is due to transitions from the 1s→3d, which will be explained in more detail later.

1.9 X-ray absorption near-edge structure (XANES)

The XANES spectrum includes the edge and the pre-edge, from which it is possible to determine the oxidation state and local geometry of the element. Increasing the oxidation state results in the edge shifting to higher energies. As the effective nuclear charge increases, more energy are required in order to excite a core electron.

1.9.1 The pre-edge feature[38,39,27]

The pre-edge feature is smaller absorption peaks which arises before the actual K-edge. The pre-edge feature is a consequence of the exitation of core electrons to a higher orbital which is empty or half full. For the first row of transition metals the 1s→3d transition has previously been regarded as the possible transition for all the complexes regardless of their symmetry. However Yamamoto describes the pre-edge feature as a transition from 1s→4p due to 3d-4p mixing in tetrahderal complexes. This will be explained more thoroughly in this section. The different factors that contributes to the preege feature are discussed below:

1. The pre-edge feature depends on the geometry of the complex. The geometry of molecules are affected by the type of metal and the type of ligand. Lone pairs also contributes to the final geometry. The geometry of the complex determines the symmetry and the point group which gives irreversible symboles for the orbitals to the metal, which then contributes to the bond. These are labels such as a, a_{1g}, e, e_g and so on, which are used to label molecular orbitals in nonlinear molecules. They are based on the behaviour of the orbitals under all the symmtry operations of the relevant molecular group. The label is assigned by referring to the character table of the group.[13] By studying the character table for octahedral complexes the 1s orbital has a A_{1g} symmetry and the 3d orbitals have symmetry labels of E_g and T_{2g} (referring to

subsection 1.5). The subscript g means gerade (even) and u means ungerade (uneven). Generally the laporte selection rules states that a centrosymmetric molecule has only one allowed transition, when there is a change in parity; i.e g≠g is a forbidden transition, and g≡u is an allowed transition. The s, p and d-orbitals are even, uneven, and even functions respectively. Hence the 1s→3d transition is forbidden and s→p transitions are allowed, according to laporte.[39] However there are exeptions to the rule. If the inversion centre is broken and the geometry is no longer a perfect octahedra, the transition becomes allowed.[32]

The 1s→ 3*d* is not an electric dipole transition, but a quadrupole transition. This is because electric dipole transitions are only possible in p orbitals as it has a dipole, the d-orbitals on the other hand has a quadrupole. The electric dipole transition is a more probable and a stronger transition than a quadrupole transition. The electric dipole transition is evident in tetrahedral complexes due to 3d-4p mixing, which is described below more thoroughly.[39]

In figure 1.28 where V_2O_5 and divalent vanadium is present, the pre-edge feature of V_2O_5 is evident. As mentioned in subsection 1.6, the geometry of V_2O_5 is square planar and there is no centre of inversion, this again mean that the laporte selection rule does not apply. $[V(H_2O)_6]^{2+}$ is as shown in subsection 1.6 a perfect ochtahedra and the transition is not allowed, which is shown in the figure since it does not have a pre-edge.

2. A stronger pre-edge is visible to tetrahedral complexes, and is a result of 3d-4p mixing in 3d transition metals. By group theory 3d-4p mixing can only occur in non-centrosymmetric complexes. Thus are the pre-edge feature in octahedral complexes very weak. When the symmetry is a distortion from the octahedra, 3d-4p mixing is allowed and the dipole transition is allowed, thus leads to a pre-edge with a higher intensity.[40, 41]

   The pre-edge feature in tetrahderal complexes is not due to the 1s→3d transition as mentioned above, but transition to the p component in

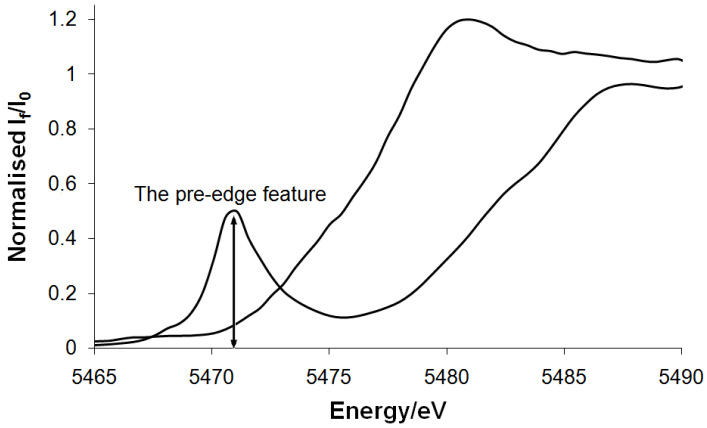

Figure 1.28: The pre-edge feature of V_2O_5 and the $[V(H_2O)_6]^{2+}$ ion which is laporte forbidden, thus there are noe pre-edge.

d-p hybridised orbital. The 3d-4p mixing depends on coordination symmetry. If a p component was mixed in a d-orbital through hybridisation, transition of a 1s electron to the hybridised p-orbital would be observed. By studying character tables it is possible to predict if there are hybridisation of d and p-orbitals. In table 1.1 of the tetrahedral point group the $p_{x,y,z}$ and $d_{xy,xz,yz}$ orbitals belong to the irreducible representation, T_2, hence p-d hybridisation can occur. Then the electric dipole transition of a 1s electron occurs to the hybridised p-orbital following with an electric quadrapole transition to d-orbitals. However in the O_h point group there are no irreducible representations where both d and p-orbitals belong. Thus only electric quadrupole transitions can occur for O_h. With D_{4h} point group the irreducible character e_g could form a p-d hybridisation, however the pre-edge feature is not enhanced as the p and d-orbitals are orthogonalised. As shown, the use of character tables of group theory could predict the pre-edge intensity qualitatively without theoretical calulations, if the structure and the point group is known.[39]

Table 1.1: The character tables of tetrahedral complexes (T_d), octahedral complexes (O_h) and those with a D_{4h} symmetry

T_d		
	p	d
A_1		$x^2+y^2+z^2$
A_2		
E		$(2z^2\text{-}x^2\text{-}y^2, x^2\text{-}y^2)$
T_1	(R_x, R_y, R_z)	
T_2	(x,y,z)	(xz,yz,xy)

O_h		
	p	d
A_{1g}		$x^2+y^2+z^2$
A_2g		
E_g		$(2z^2\text{-}x^2\text{-}y^2, x^2\text{-}y^2)$
T_{1g}	(R_x, R_y, R_z)	
T_{2g}		(xz,yz,xy)
A_{1u}		
A_{2u}		
E_u		
T_{1u}	(x,y,z)	
T_{2u}		

D_{4h}		
	p	d
A_{1g}		x^2+y^2, z^2
A_{2g}	R_z	
B_{1g}		$x^2\text{-}y^2$
B_{2g}		xy
E_g	(R_x, R_y)	(xz,yz)
A_{1u}		
A_{2u}	z	
B_{1u}		
B_{2u}		
E_u	(x,y)	

3. Dependence on coordination number. Farges *et al* studied the dependence on the pre-edge peak height and the energy on the cooridnation number for Ti, Fe and Ni species. The pre-edge intensity decreases with increasing coordination number. The peak energy shifts with the coodination number of Ti and Ni species, but were independent in the case of Fe. A decrease in the pre-edge intensity as a result of higher coordination is also seen for vanadium, when the coordination is changed from fourefold to sixfold.[39]

4. The increase in vacancies in the 3d orbital, increases the intensity of the pre-edge, as the case with increasing oxidation state. There should also be a shift in the pre-edge position towards higher energies with increasing oxidation state.[32] This is because of the increase in the effective nuclear charge, in which higher energies are needed to eject the electron from the core shell.

5. The intensity of the pre-edge feature is also effected by the molecular cage effect. The molecular cage effect proposed by Kutzler *et al*[42] is defined by the first ligand which is coordinated to the absorbing metal. This effect brings with it some contributions: A cage which breaks the inversion center, can enable 1s→3d transitions. If the neighbouring ligand is close to the metal the pre-edge intensity increases. In other words means that the smaller the molecular cage, the larger intensity has the pre-edge.[42]

Figure 1.28 show the pre-edge for V_2O_5. There have been some study on what causes the intense pre-edge in V_2O_5. Previously the intensity has been assigned to the electric dipole transition to the hybridised 3d orbital on vanadium and the 2p orbital on oxygen. However the bond lengths in V_2O_5 are not equal as described in subsection 1.6. It was found by Mossanek *et al* that the intense peak was an electric dipole transition to the vanadyl group (V=O). The contribution of the electric quadrupole transition was minimal. This characteristic feature can also be assigned to other vanadium compounds

with a vanadyl group such as $VOSO_4$, where the intense pre-edge is an electric dipole transition from 1s to p in the 3d V -2p O hybridised orbital.[39, 32]

The pre-edge feature contains information about electronic configuration and local symmetry.The area of this peak can give information concerning the share of metal cation in octahedral and tetrahedral sites.

1.10 Extended x-ray absorption fine structure(EXAFS)[36,37,38,43]

EXAFS generally refers to the region 40-1000eV above the absorption edge. The extended X-ray absorption fine structure can give us information about the valence shells of the central atom, and the neighbouring atoms.

EXAFS spectroscopy refers to the measurement of the X-ray absorption coefficient μ as a function of photon energy E above the threshold of an absorption edge. When a collimated beam of monochromatic X-rays travel through matter, it inevitably loses intensity via interaction with the material. The loss in intensity I is proportional to the original intensity and the thickness x:

$$dI = \mu I dx \tag{1.14}$$

μ is the linear absorption coefficient. If the expression is integrated the following expression is obtained:

$$\frac{I}{I_0} = e^{-}\mu X \tag{1.15}$$

Where I is the intensity of the transmitted beam, and I_0 is the intensity of the incident beam. μ depends strongly on X-ray energy E and atomic number Z, and the density ρ and the atomic mass A:

$$\mu \approx \frac{\rho Z^4}{AE^3} \tag{1.16}$$

This is escpecially important for vanadium which is the element of interest in this thesis. The energy of vanadium is operated at low energies, and therefore the importance of sample thickness and the absorption coefficient becomes vital. This will be assessed in more detail later in section 1.11

In a transimission experiment the μ or μx is calculated by

$$\mu x = ln\frac{I}{I_0} \tag{1.17}$$

In fluorescence mode the experiment is calculated by:

$$\mu x = \frac{I_f}{I_0} \tag{1.18}$$

For a monoatomic gas with no neighbouring atoms a photoelectron ejected by absorption of a X-ray photon will travel as a spherical wave with wavelength equal to:

$$\lambda = \frac{2\pi}{k} \tag{1.19}$$

In the presence of neighbouring atoms, the outgoing photoelectrons can be backscattered from the neighbouring atoms thereby producing an incoming wave which can interfere either constructively or destructively with the outgoing wave near the origin, resulting in the oscillatory behaviour of the absorption. This is the riples as seen in the EXAFS spectra. In figure 1.29 the interferens with the neighbouring atoms are illustrated.

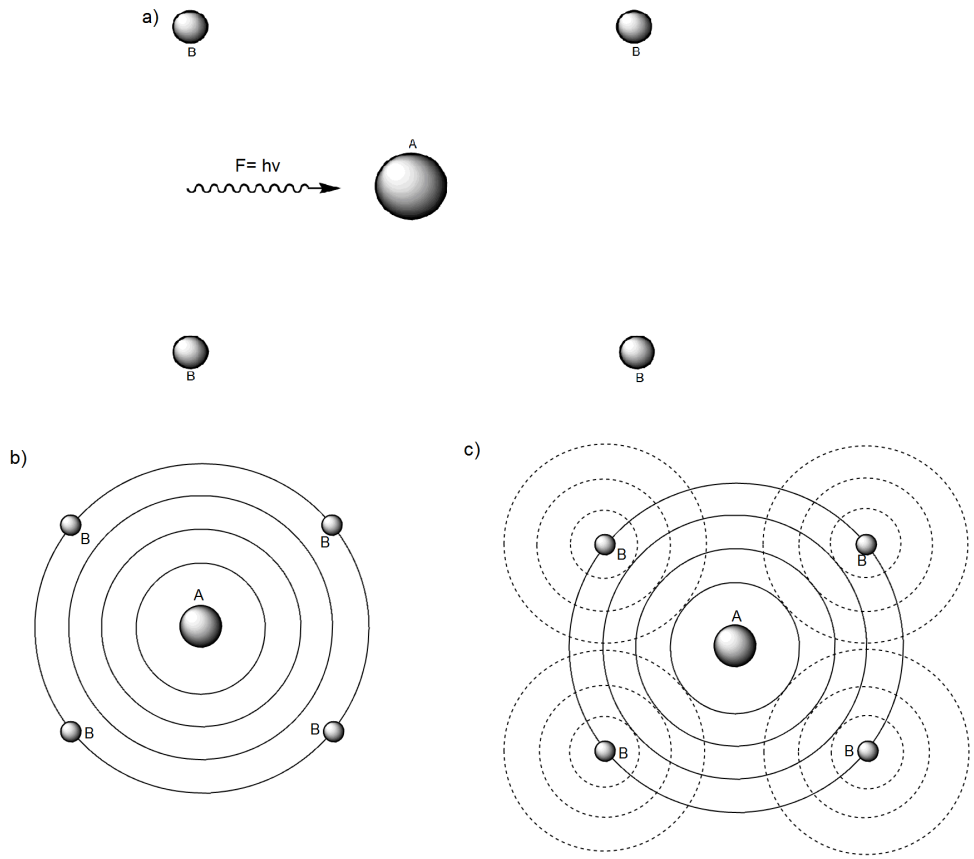

Figure 1.29: An illustration of the backscattering which shows as oscillations in the EXAFS; a) a X-ray beam with energy E=hv higher than the threshold energy ejects as photoelectron, b) A spherical wave of the incident photoelectron is emitted from the absorber, c) the outgoing photoelectron wave is backscattered by the surrounding neighbours. The waves from the backscatterer and the absorber interfers constructively or destructively

The EXAFS spectrum considers only the backscattering resulting in oscillations. The normalised absorption spectrum is defined as:

$$\chi(E) = \frac{[\mu(E) - \mu_0(E)]}{\Delta\mu_0(E)} \tag{1.20}$$

The oscillations in the EXAFS is due to the backscattering and is termed χ(E) and μ(E) is the measured absorption at a given X-ray wavelength. The μ_0(E) is the absorption that would be observed if there were a monoatomic gas, in which there are no neighbours (the background). Except as mentioned in a monoatomic gas, the wavelength of the material without neighbours cannot be measured and therefore it is calculated. It is convenient to convert χ(E) from the energy scale (eV) to the photoelectron scale (Å^{-1}):

$$k = \sqrt{\frac{2m}{\hbar^2}(E - E_0)} \tag{1.21}$$

- E is the incident photon energy
- E_0 is the threshold energy of that particular absorption edge
- k is the photo-electron wavenumber.
- m is the rest mass of the electron
- $\hbar$ is the reduced Plancks constant: $\frac{h}{2\pi}$

The EXAFS equation is a theoretical expression that describes χ(k) in terms of structural paramters and thereby allows structural information to be derived from the experimental χ(k). Equation 1.23 is known as the EXAFS equation. The EXAFS equation is based on the single scattering plane-wave approximation. In this approximation the electron wave is viewed as a plane wave to simplify the deviation. The plane-wave approximation assumes that the atomic radii is much smaller than the inter-atomic distances, and is valid only for higher k-values (k>3Å). In single-scattering the electron is assumed

to only be scattered once before returning to the absorbing atom. Equation 1.22 show that the EXAFS equation does mainly consist of two parts, the amplitude A_j(k) and a sine function which describes the inter-atomic distance between absorber and scatterer atoms ($2kr_j$) and a phase factor (ϕ_{ij}(k)).

$$\chi(k) = \sum_j A_j(k) sin(2kr_j + \phi_{ij}(k)) \tag{1.22}$$

$$\chi(k) = \sum_j N_j S_j(k) F_j(k) e^{-2\sigma_j^2 k^2} e^{-2r_j/\lambda_j(k)} \frac{sin(2kr_j + \phi_{ij}(k))}{kr_j^2} \tag{1.23}$$

- F_j(k) is the backscattering amplitude
- N_j is the number of neighbouring atoms of type j
- σ_j is the Debye-Waller factor (thermal vibrations)
- r_j nearest neighbour distance between the central atom and backscatterers in the j^{th} shell.
- ϕ_{ij}(k) is the total phase shift experienced by the photoelectron.
- $e^{-2rj/\lambda j}$ is due to inelastic losses in the scattering process.
- λ_j is the electron mean free path.
- the sin function, sin($2kr_j$ + ϕ_{ij}(k)) accounts for the oscillations seen in the EXAFS.
- S_i(k) is the amplitude reduction factor

Phase

The frequency of each EXAFS wave depends on the distance between the absorbing atom and the neighbouring atom since the photoelectron wave

must travel from the absorber to the scatterer and back. During this trip the photoelectron experiences a phase shift (Coulombic interaction) of the absorber twice. The first part arises as a result of the photoelectron wave travelling a distance $2r_j$ from the absorber to the backscatter and then back to the absorber again.

The second contribution to the total phase, $\phi_{ij}(k)$, alters the velocity of the first contribution. It increases the velocity of the photelectron as it approaches the neighbouring atom and then slows it down as it returns. The experimental or theoretical $\phi_{ij}(k)$ is subtracted from the total phase.

Amplitude

The backscattering amplitude function $F_j(k)$ is only a function of the scatterer atom, and not the absorber atom. The backscattering amplitude is element specific. As each atom has a unique electron configuration the backscattering pattern will also be unique for each element.

A way to reduce the EXAFS amplitude is caused by multiple excitations at the central atom, whereas the second is associated with excitation at the neigbouring environment. The loss in amplitude due to multiple excitations are approximated by the amplitude reduction factor $S_i(k)\approx 1$. The loss in amplitude due to excitation of the neighbouring environment is approximated by $e^{-2r/\lambda(k)}$.

Debye-Waller factor

The Debye-Waller factor σ plays an important role in EXAFS spectroscopy. It contains important structural information and chemical information which is otherwise difficult to obtain. The Debye-Waller factor has two components σ_{stat} which point to static disorder, and σ_{vib} which is thermal vibrations. The Debye-Waller factor is the sum of the two components in square form.

1.10.1 Experimental setup

1.10.2 Data analysis and reduction[38,43,44]

Extraction of structural information from EXAFS is a multistep procedure that involves considerable data reduction. In this thesis Athena is used for background subtraction, deglitching, truncation and peak fitting. EXCURVE98 is used to refine the EXAFS data to find the multiplicty, the neighbours, the distance and the Debye-Waller factor.

The first step in the data analysis is extraction of the EXAFS fraction of the X-ray absorption spectrum, which is termed χ(E) from μ(E). By fitting a curve in the pre-edge region and extrapolating it to the end of the spectrum. This extrapolated curve is then subtracted from the whole spectrum. By studying equation 1.20 it is understood that determination of χ(E) requires that the background,μ_0(E), is removed from μ(E). As mentioned previously it is impossible to measure μ_0(E) experimentally (if the atom is not monoatomic), therefore the μ_0(E) must be approximated numerically. Athena is the progam that is used for background subtraction in this thesis. The program calculates the μ_0(E) by a spline equation. The edge step normalisation is done in Athena to set the spectrum equal to zero. It is done with taking the difference of μ(E) and μ_0(E) and divide it on an estimation of $\Delta\mu_0$(E). This edge step is determined by taking the regression line to the data in some region below the edge and subtract it from the data. Then a quadratic polynomial is regressed to the data in some region below the edge and extrapolated back to E_0. The extrapolated value of the post-edge polynomial E_0 is used as the normalisation constant. This procedure is shown in figure 1.30

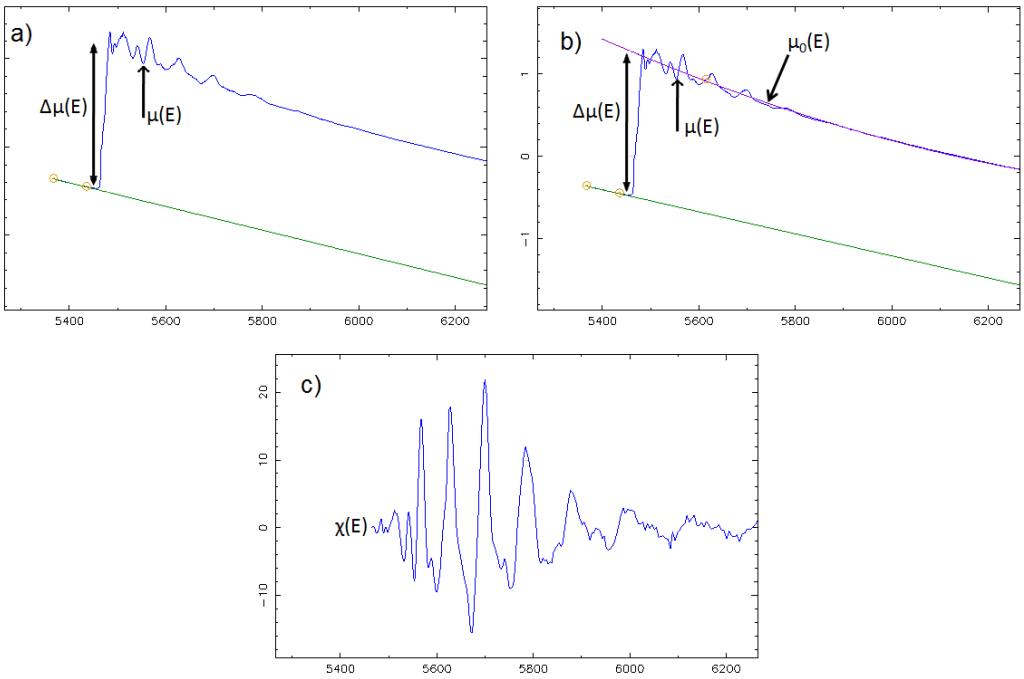

Figure 1.30: A systematic illustration of the steps in the background subtraction done in Athena; a) The pre-edge line is extrapolated to the end of the spectrum, b) μ_0(E) is calculated as a smooth line in Athena and is subtracted from μ(E) and dividing by the μ step which is denoted as $\Delta\mu$(E), c) the χ(E) after the smooth background line is subtracted from the original EXAFS spectra and divided by the $\Delta\mu$(E).

The next step is the conversion of χ(E) to k$^n\chi$(k). By using equation 1.21 the χ(E) is converted to k-space when the threshold energy (E$_0$) is known. The χ(k) is shown in figure 1.31 down below

Step 4 is the Fourier transformation of the χ(k) into a radial distribution function known as the Fourier transform (Å). The Fourier transformation is defined by:

$$FT(R) = \frac{1}{\sqrt{2\pi}} \int_{k_{min}}^{k_{max}} k^n \chi(k) e^{i2kR} dk \tag{1.24}$$

The Fourier transformation can be taken with different k weightings. This can be used to distinguish between high and low Z scatterers around the

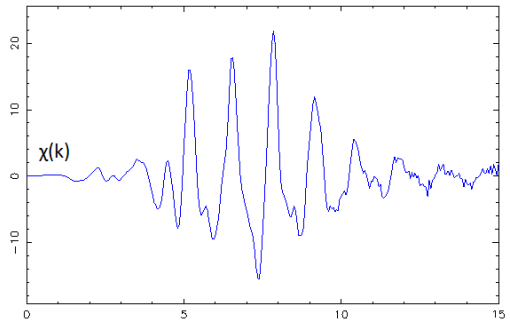

Figure 1.31: The k-space ($Å^{-1}$) in χ(k) in which can be k^n weighted with n being 0,1,2 or 3.

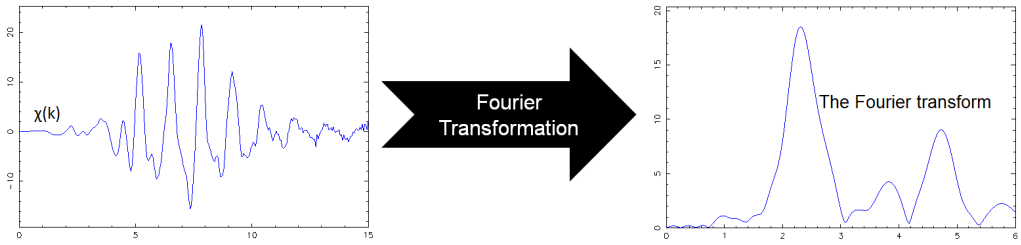

Figure 1.32: The Fourier transformation from k-space to R-space.

absorber atom. An element with low mass (like oxygen) will scatter mainly at low k-values, while platinum will scatter at higher k-values. It is the χ(k) that is the backscattering curve which is refined in EXCURVE98. The Fourier transform is a more visual way to study the bond lengths and the multiplicity surrounding the central atom. The Fourier transformation is shown in figure 1.32.

Fourier filtering is a useful tool in EXCURVE98 as it allows to extract one peak, refine and find the different paramters such as the multiplicy (N_i), Debye-Waller factor (A_i) and the distance (R_i). The principle of Fourier filtering is shown in figure 1.33

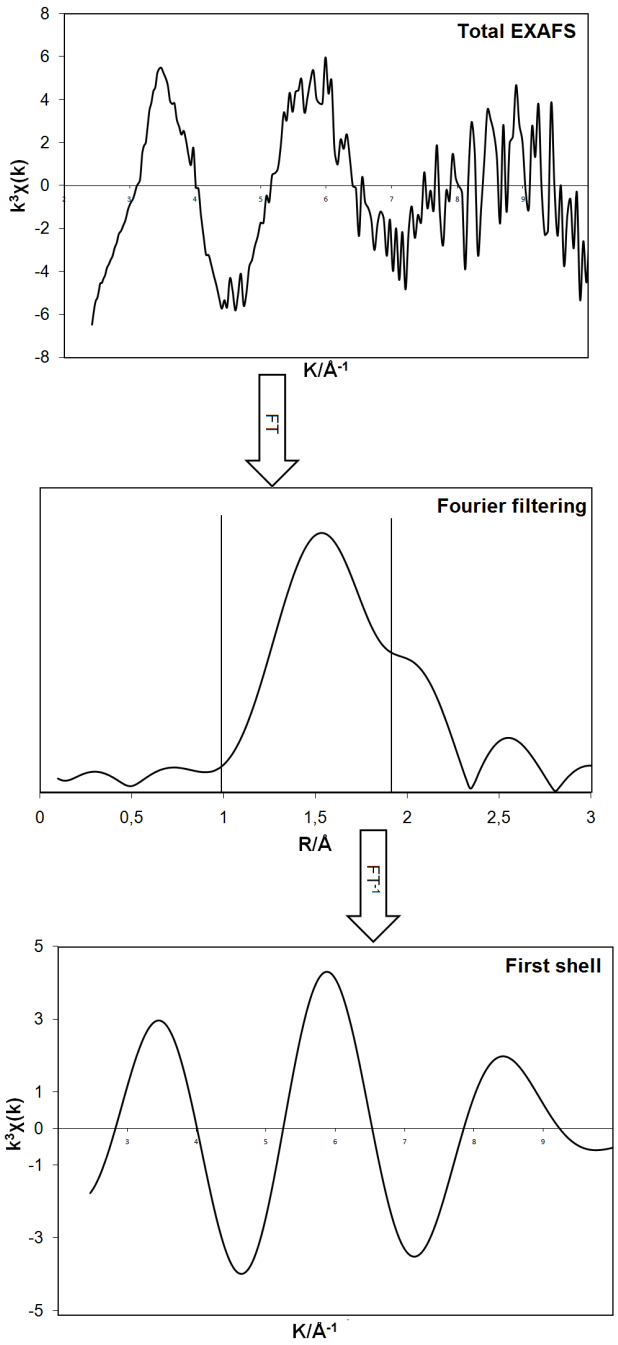

Figure 1.33: The Fourier filtering done in EXCURVE98

Before extracting the data from Athena to EXCURRVE98, the data need to be deglitched, as it can give some trouble with the data refining in EXCURVE98. The glitches arise when the monochromator is out of the energy range, in which spikes in the spectrum appears. If the background does not look like a smooth line or if the χ(k) does look fishy, it might help to truncate the data. This feature in Athena allows you to define an energy and to chose wether the data points before or after that energy are removed from the data. By deglitching one point is removed, when the truncation feature is used, several points can be removed at once. This is very important to apply on the vanadium data as it has several glitches and usually the χ(k) has to be truncated as it does not contain a lot of information above 10Å^{-1}, only a low signal to noise ratio.

Merging data feature in Athena is very useful for vanadium data. As the vanadium data can be very noisy, it is helpful to do several scans of the same sample, and Athena can sum them by using the merge function. Another very important feature in Athena concerning vanadium, is the peak fitting analysis. As previously mentioned in section 1.9.1 vanadium can expereience intense pre-edges. The peak fitting technique makes if possible to calculate the area and position of the pre-edge. The peak functions that are available are Lorentzian and Gaussian. These are unit normalised, so the fitted amplitudes are also the areas measured in eV. The fitting range can be defined and is represented by two vertical lines in the plot, as seen in figure 1.34. After each fit, a complete summary of the fitting result is written into the space viewed by clicking on the tab labeled results. The R-factor of the fitted paramters is:

$$\frac{sum((data - fit)^2)}{sum(data^2)} \tag{1.25}$$

Figure 1.34 show the peak fit procedure of V_2O_5.

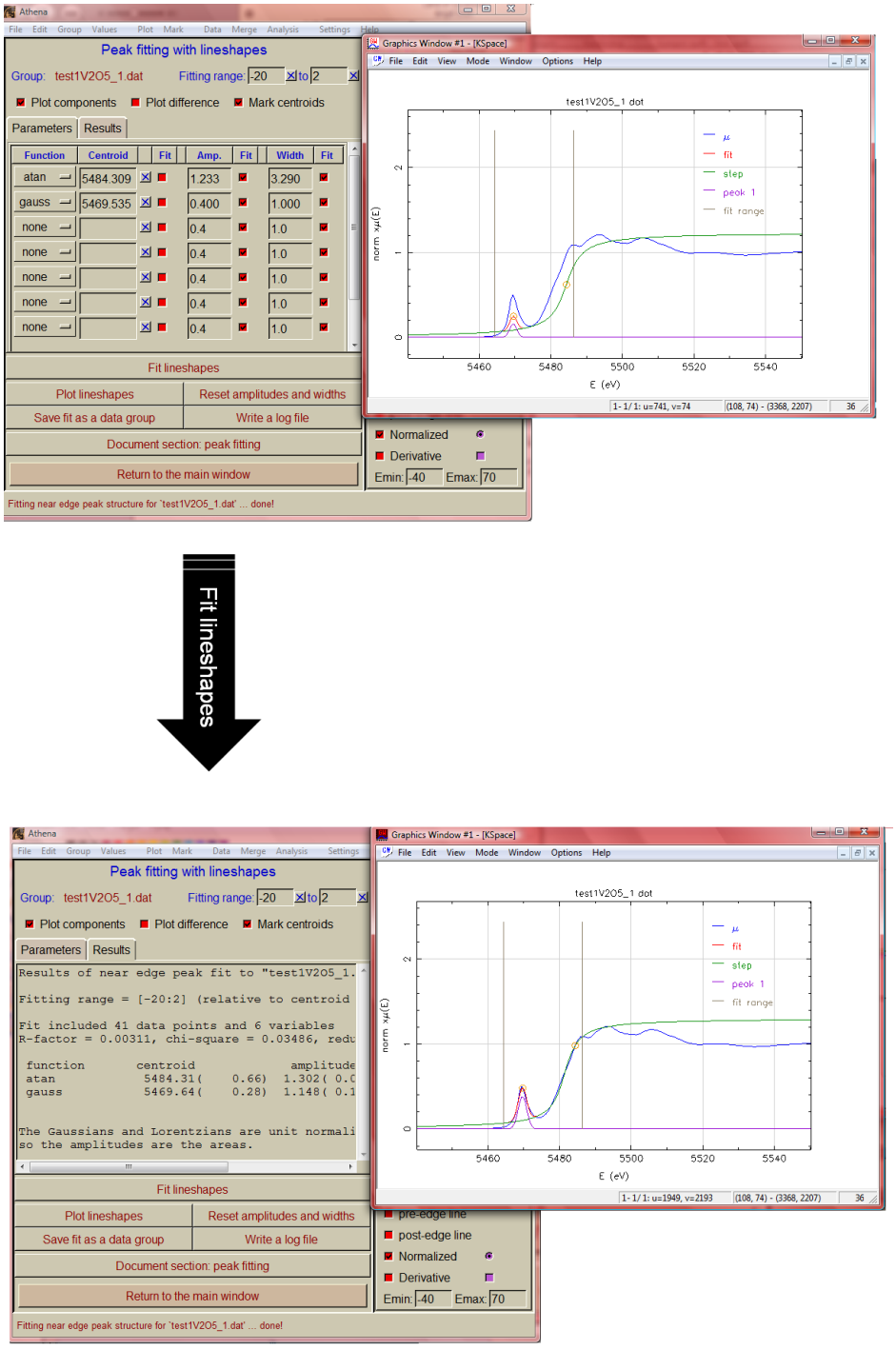

Figure 1.34: The peak fit procedure of V_2O_5. First the peak is chosen to be either Lorentzian or a Gaussian peak, and then the peak is refined.

1.11 XAS of vanadium

As previously mentioned it is challenging to achieve acceptable EXAFS data on vanadium. In this section it will be focused on the troubles and what should be focused on concerning the analysis of vanadium.

In equation 1.16 it is shown that the absorption coefficient is dependent upon the atomic number (Z), the atomic mass (A), the X-ray energy (E) and the density (ρ). Therefore a higher absorption coefficient the more is being absorbed by mediums such as air. As seen in equation 1.17 the transmission is dependent on the absorption coefficient and the sample thickness. Therefore with a high absorption coefficient and a thick sample, the intensity is to low to get reasonable data from I. The K-edge for vanadium is very low (5465eV), compared to other elements. Energies under 6000eV absorbs a lot of the X-ray photons, thereby it is difficult to achieve good resolution on vanadium. A lot of the photons are absorbed before the sample or by the kaptan-tape covering the sample. By reducing the sample thickness, e.g. pressing the vanadium sample into pellets, it is possible to do transmission data collection. Then the sample thickness is reduced, which was a factor affecting the intensity that is transmitted through the sample as shown in figure 1.35.

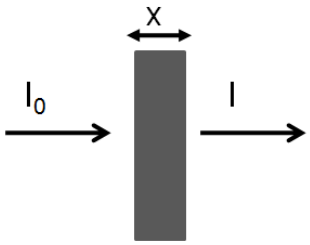

Figure 1.35: An illustration to show how the sample thickness affects the transmission data.

There is also possible to use fluorescence data collection. Fluorescence radiation occurs when an outer shell electron fills the vacancy from the electron that was excited. When that electron is relaxed from the outer shell it ejects

fluorescence radiation. This phenomena is very useful when the absorption of elements with low absorption coefficient such as vanadium, is studied. Fluorescence detectors only detects the fluorescence signal from the surface of the sample, and thereby the problem with the sample thickness and how the sample is prepared with respect to the kaptan tape can be neglected. The illustration of fluorescene radiation is shown in figure 1.36. However the energy of vanadium is still in the low energy range, and although the data collection is possible, the signal to noise ratio is still very small.

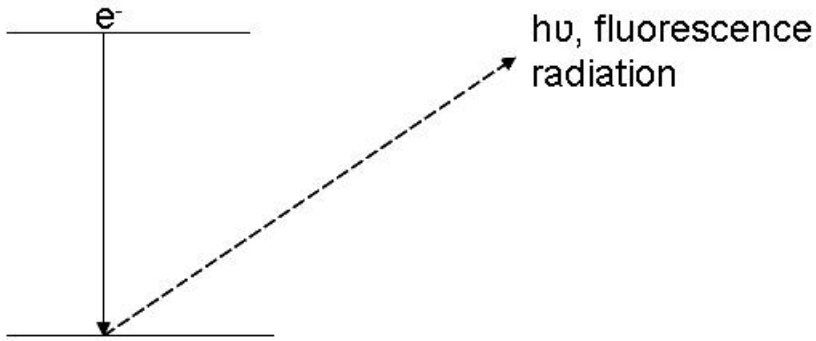

Figure 1.36: Fluorescence radiation

1.12 Other characterisation techniques

Surface measurements[45]

Specific surface area is defined as the surface area per unit mass, and is typically expressed in square centimeter per gram (cm^2/g). Specific surface area depends on the particle shape, particle size, and any imperfections or flaws present at the surface.

The best known method of determination of the surface area is the so called BET method from Brunauer, Emmett and Teller. Which is used in this thesis. The BET method is based on the relationship between the pressure of a gas that is in equilibrium with a solid surface and the colume of the gas adsorbed at the particular pressure at the surface. The assumptions in the BET method is:

1. It is constant throughout the formation of the first layer of adsorbed gas. (Assumes monolayer adsorption)
2. In the second and higher layers it is equal to the heat of liquefaction.

A plot of the amount of gas adsorbed at a certain temperature against the relative pressure is called a sorption isotherm. It is usually presented at the volume of adsorbed gas vs the relative pressure, p/p_o. From such a plot the amount of gas needed to form a monolayer can be determined, and, assuming the cross-sectional area of the sorbate molecule, the surface area of the measured solid can be calculated. The BET equation can be given as:

$$v/v_m = ckx/(1-kx)[1+(c-1)kx] \tag{1.26}$$

- x is the relative pressure p/p_o
- k is a number smaller than 1
- c is the BET constant

- v_m is the volume of the sorbate at monolayer coverage
- v is the volume of the adsorbed sorbate

Scanning electron microscopy (SEM)[?]

When a beam of primary electrons strikes a bulk solid, the electrons are either reflected (scattered) or absorbed producing various signals. Besides secondary electrons, backscattered electrons (BSE), X-rays, Auger electrons, and other responses, are also produced. SEM captures the secondary and backscattered electrons. Figure 3.2 show the principle of SEM. The electron beam is formed by the electron gun which successively condensed by the projecting lense and the objective (magnetic) lens to spot about 5-100nm in diameter at the speciemen plane. The entire system is tightly sealed so that when in an operational state the microscope column can be evacuated to about 10^6 torr. A scan generator simultaneously drives the X and Y-scan coils in the microscope column and the cathode ray tube (CRT). Among the different types of responses produced, the secondary electrons (SE) and X-ray are collected by the photomultiplier to form an image and provide chemical compositional data.[?]

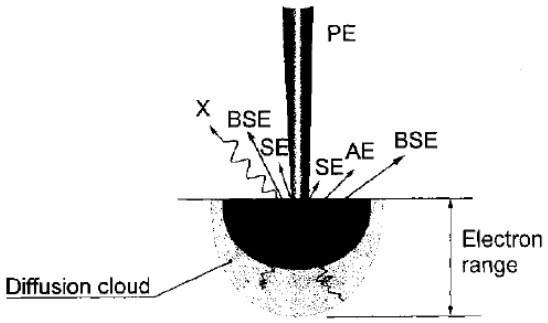

Figure 1.37: The different interaction wich arises the an electron beam is interacted with the material. The electron beam is PE, BSE= backscattered electron, SE=secondary electron, X=X-ray, AE, Auger electron[?]

ICP-MS[46]

Inductively coupled plasma mass spectrometry (ICP-MS) have been used in this thesis for elemental analysis. Ions formed in the plasma are introduced into the mass analyser, where they are sorted according to mass-to-charge ratio and detected. Solid samples are either dissolved in solution or introduced directly through laser ablation methods. A beam is introduced to the mass spectrometer and has about the same ionic composition as the plasma region from which the ions are extracted. Background ions include Ar^+, ArO^+, ArH^+, H_2O^+, $O^+{}_2$ and $Ar_2{}^+$. Such background ions can interfere with the determination of analyst.

Thermogravimetric analysis[47]

In thermogravimetric analysis (TGA) the weight changes are determined as the sample is heated at a uniform rate. In this thesis it is mainly used to detect where water is lost, and where the template might be removed in the presence of air. To study the reducbility of the vanadium samples in a reducing atmosphere, TGA was done with hydrogen coupled to a mass septrometer. By the coupling of a mass spectrometer it is possible to detect which masses that are absorbed by the sample or which masses are lost.

Raman spectroscopy[13,48]

In Raman spectroscopy the sample is exposed to intense laser radiation in the visible region of the spectrum. Most of the photons are scattered elastically (with no change in the frequency), but some are scattered inelastically, having given up some of their energy to excite vibrations. These photons have frequencies different from the incident radiation (v_{in}) by amounts equivalent to vibrational frequencies (v_i) of the molecule. When radiation of frequency ν interacts with a molecular vibration of frequency ν, one quantum of the incident radiation may disappear, with a creation of a quantum frequency

($\nu \pm \nu$). It can be considered as the photon causing a transition to a virtual excited state whose lifetime is so short that there is immidiate re-emission of a photon whose energy might be different by a quantum of vibrational energy. Conservation of energy requires a corresponding change in the vibrational energy of the molecule. The resulting spectrum is called the Raman spectrum. The Raman spectrum contain lines whose frequencies differ from that of the incident radiation by the frequencies of molecular vibrations. The lines to low frequency of the incident radiation are called Stokes lines, and those at higher frequency are called anti-Stokes lines. The anti-Stokes arise from the vibrationally-excited states. Scattered radiation of lower frequency is in general more important. A conventional Raman spectrum therefore consists of a series of Stokes emissions separated in frequency from the exciting radiation by the various vibrational frequencies of the sample.

The Raman scattering process is not a resonant interaction, and it results in comparatively weak spectra. The interaction come through the polarisation of the electron cloud of the molecule by the oscillating electric vector of the incident energy. A vibration will therefore give rise to a Raman line, if there is a change in the polarisability of the molecule. Figure 1.38 show the Raman scattering process.

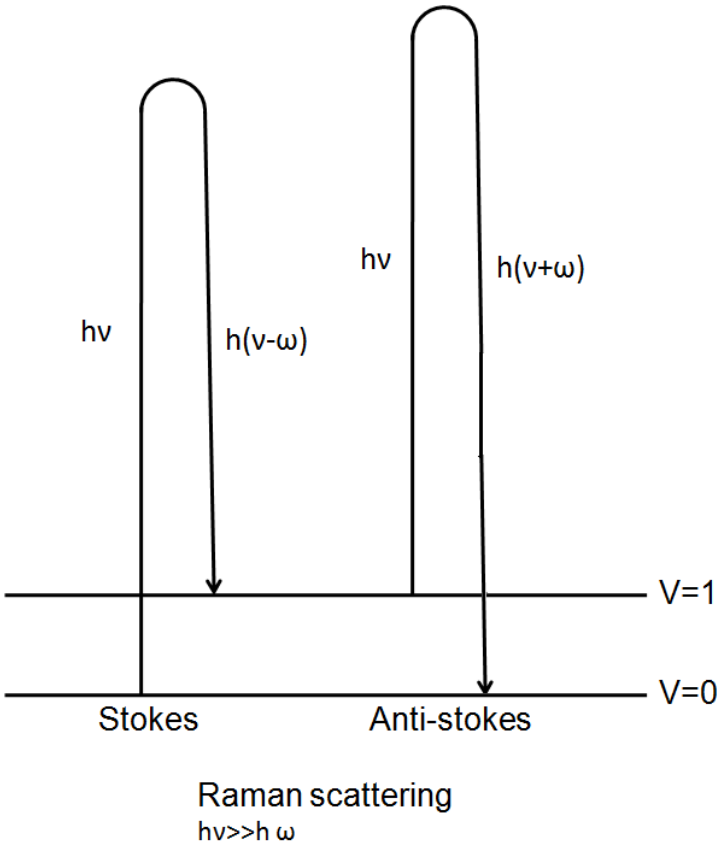

Figure 1.38: Energy levels involved in Raman scattering. Illustration inspired by Structural Methods in Inorganic Chemistry[48]

Mass spectrometer[49]

In this thesis mass spectrometers are used to detect mass loss and mass gain during *in situ* studies, and during TGA measurements. The concept of mass spectrometry is relatively simple. A compound is ionised, the ions are separated on the basis of their mass/charge ratio and the number of ions representing each mass/charge unit is recorded as a spectrum.[50] The sequence in a mass spectrometer is first ionisation. The atom is ionised by knocking one or more electrons off to give a positive ion. Mass spectrometers always work with positive ions, the most frequently positive ion is + 1, as it is more difficult to remove further electrons from an already positive ion.The second step is acceleration. The ions are accelerated so that they all have the same kinetic energy. Then the ions are deflected by a magnetic field according to their masses. The lighter they are, the more they are deflected. The amount of deflection also depends on the number of positive charges on the ion. The more charge cation, the more it is deflected. Finally the ions are detected. The beam of ions passes through a machine, and is detected electrically.

Chapter 2

Experimental: The synthesis of VAPO-5 and VAPSO-5

2.1 Synthesis of VAPO-5 and VAPSO-5

The VAPO-5 samples and VAPSO-5 samples were synthesised by modifying the procedure reported by Yu *et al*[4]. The mole ratio was as follows:
Al:P:xV:0.675TEA:20H_2O for VAPO-5 and
Al:P:xV:ySi:0.675TEA:20H_2O for VAPSO-5

In table 2.1 the different synthesis conditions are shown. In a typical synthesis of VAPO-5 orthophosphoric acid (H_3PO_4, 85%, Merck,7.064g) and distilled water was mixed for 5 minutes before adding the vanadium source,vanadium pentoxide(V_2O_5, Merck,0.9g).The mixture was stirred for 1h and 30min or until the vanadium salt was fully dissolved with the mixture reaching a pH between 0 and 1. Then pseudoboehmite(AlOOH, Si/Al ratio, Sasol, 7.09g) was added and the resulting gel left to stir for 1h and 20min until it appeared homogeneous. The pH of the mixture was now raised to 4. Finally triethylamine (TEA, Aldrich,6.89g) was added and after stirring the whole mixture for a total of 2h and 50min the gel was put in an autoclave and crystallised in the oven at 180°C for 24h.

The crystallised product was filtered, and excess template was washed off. The sample dried at 100°C for 24h. To remove the template, the VAPO-5 sample was calcined at 500°C for 17h using a ramp rate of 1°C/min. The sample was characterised by X-ray powder diffraction, as shown in section 3.

The synthesis of VAPSO-5 followed the procedure as described above, but the vanadium source in this instance was $VOSO_4$ (Alfa Aesar,1.63g), and the silicon source was As40 (SiO_2, DuPont,6.009g). In the synthesis the silica was added after the template.

Table 2.1: The different synthesis parameters which has been changed in the synthesis. The crystallisation temperature was always at 180°C

Sample	V Source	Gel composition				Template	Time
		x[a]	z[b]	y[c]	r[d]		
VAPO-5\1(V)	V_2O_5	0,1	1	0	0,675	Et_3N	24h
VAPO-5\2(IV)	$VOSO_4$	0,1	1	0	0,675	Et_3N	24h
VAPO-5\3(IV)	$VOSO_4$	0,01	1	0	0,675	Et_3N	24h
VAPO-5\4(IV)	$VOSO_4$	0,05	1	0	0,675	Et_3N	24h
VAPO-5\5(IV)	$VOSO_4$	0,1	1	0	0,675	DCHA	24h
VAPO-5\6(IV)	$VOSO_4$	0,05	1	0	0,675	DCHA	24h
VAPO-5\7(IV)	$VOSO_4$	0,1	1	0,6	0,675	Et_3N	48h, 6d
VAPO-5\8(IV)	$VOSO_4$	0,1	1	0	0,675	Et_3N	4h,9h,24h,49h
VAPO-5\9(V)	V_2O_5	0,18	0,475	0	1	Pr_3N	24h
VAPO-5\10(IV)	$VOSO_4$	0,18	0,475	0	1	Pr_3N	24h
VAPSO-5\1(IV)	$VOSO_4$	0,1	1	0,6	0,675	Et_3N	24h
VAPSO-5\2(IV)	$VOSO_4$	0,1	1	0,4	0,675	Et_3N	24h
VAPSO-5\3(IV)	$VOSO_4$	0,1	1	0,3	0,675	Et_3N	24h
VAPSO-5\4(IV)	$VOSO_4$	0,05	1	0,6	0,675	Et_3N	24h
VAPSO-5\5(IV)	$VOSO_4$	0,01	1	0,6	0,675	Et_3N	24h
VAPSO-5\6(IV)	$VOSO_4$	0,15	1	0	0,675	Et_3N	24h

[a] The vanadium ratio according to the article Comparative study of the Vanadium Species in VAPO-5 and VAPSO-5 Molecular Sieves with the relationship:Al:P:xV:0.675TEA:20H_2O for VAPO-5 and Al:P:xV:ySi:0.675TEA:20H_2O for VAPSO-5.

[b] Usually the modified procedure from Yu *et al* was used. For two synthesis the modified procedure of Venkatathri *et al* was used.[51]

[c] The silicon ratio in the synthesis.

[d] The template ratio. TEA is Et_3N and Tripropylamine is Pr_3N.

2.2 Ion exchange of H-ZSM-5

A 0.05M solution of V_2O_5 (30ml) was added to H-ZSM-5 (Zeolyst International,Si/Al=80,1g), and the mixture stirred for 24h. The excess vanadium solution was washed off and the powder dried at 100°C for 24h. The ion exchange was also done with the tetravalent solution of 0.1M $VOSO_4$ and H-ZSM-5 (Zeolyst International,Si/Al=80, 1g), with the mixture stirred for 24h, and the procedure followed as described above. The 0.1M solution of $VOSO_4$ was also ion exchanged in an autoclave as it is acknowledged that the metal content of the zeolite is increased when it is hydrothermally treated.[52] The ion exchange was done to compare the behaviour of the VAPO-5/VAPSO-5 and V:ZSM-5 during the *in situ* studies.

2.3 Reduction of vanadium(V) with Jones reductor

Jones reductor sonsist of a sylinder filled with zinc, and is activated by slowly adding H_2SO_4 (50ml, 1M). A solution of VO_2^+ (0.05M) was added to the reductor, and went slowly through the zinc. All renmants of the solution was washed by H_2SO_4 (0.5M). The outlet of the reductor had to be covered in aluminium foil as the reduced vanadium entered the erlenmeyer flask, to limit the air supply. Since vanadium(II) is very easily oxidised to vanadium(IV). The chemical equations are described in section 1.6. Figure 2.1 show the Jones reductor.

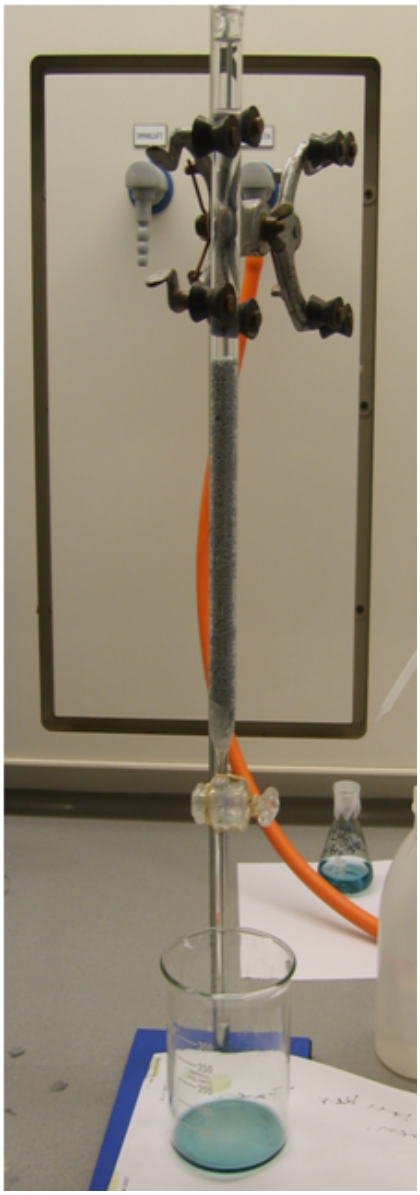

Figure 2.1: The Jones reductor used for the reduction of vanadium.

2.4 Characterisation techniques

2.4.1 X-ray diffraction,XRD

XRD was done at the institute of Material Technology at NTNU in Trondheim. There were two different diffractometers used: A Siemens D-5005 diffractometer operated at 50kv and 40mA and using Ni-filtered Cu K_α radiation. The diffractograms were collected using a constant slit opening and a step size of 0.03° covering a range of 5-50° 2Θ with a counting time of 6 seconds per step. An a Bruker D8 focus diffractometer. The diffractometer uses a Cu_α X-ray tube. The diffactometer uses a LynxEye detector and the angular range covered was 5-50° 2θ, step size 0.02°, 40kV and 40mA.

2.4.2 BET

Surface measurements was performed on a Micromeritics Tristar3000 surface area and porosimetry analyser at liquid nitrogen temperature. The samples were degassed with Vac-Prep091 at 250°C at 0.12mbar for 24h prior to the measurements.

2.4.3 ICP-MS

The elemental analysis was performed on a high resolution Inducive Coupled Plasma ElementII . Pretreatment of the samples containing silicon was dissolved in HNO_3 and HF. The the samples were autoclaved under high pressure with Milestone UltraClave. For the regular VAPO-5 samples, agua regia (HNO_3 + HCl) was used to dissolve the samples. After the autoclavation the solutions were diluted with distilled water. Then they were further analysed.

2.4.4 X-ray absorption spectroscopy, XAS

X-ray absorption data were collected in the fluorescence and transmission mode at the vanadium K-edge at the Swiss Norwegian Beamlines (SNBL, BM01b) using a 13 element Ge multi channel detector.The beamline is equipped with a Si-111 double crystal monochromator and chromium mirrors to reflect high intensity glitches. Data were collected in the multibunch filling mode providing a maximum current of 200 mA. The vanadium samples was filled in a sample holder with kapton windows. The EXAFS spectra were measured with 5 eV steps below the edge, 0.2 eV steps in the edge region, and steps equivalent to 0.03 $Å^{-}1$ increments above the edge (region borders were 5400, 5450, and 5500 eV). The scan ended at 6000eV. For EXAFS Several XAS scans were collected and summed. The XANES scan ended at 5500eV. All XANES spectra were energy corrected against a vanadium-foil calibration (5465 eV). In ion chamber I_0 it was 20%N_2 and 80%He in ion chamber I_1 and I_2 it was 90%He and 10%Ar.

The X-ray data were collected in fluorescence mode at the vanadium K-edge at MaxLab (I811) using a multi power wiggler. The beamline is equipped with a Si-111 double crystal monochormator. The EXAFS spectra were measured with 10eV eV steps below the edge, 0.5eV eV steps in the edge region, and steps equivalent to 0.05 $Å^{-1}$ increments above the edge (region borders were 5363.75, 5443.76, and 5493.76 eV). The scan ended at 6158.75eV. For EXAFS Several EXAFS scans were collected and summed. The XANES scan ended at 5532.77eV. All XANES spectra were energy corrected against a vanadium-foil calibration (5465 eV).

X-ray data was collected in fluorescence mode at hte vanadium K-edge at Dubble. The beamline is equipped with a Si-111 double crystal monochromator, and uses bending magnets. All XANES spectra were energy corrected against a vanadium-foil calibration (5465 eV).

In situ measurements

XAS is a viable technique for studying catalytic systems in which the catalyst is a metal on a carrier system. XAS is a local probe technique where the metal i studied.

The samples were placed in an *in situ* cell which is shown in figure 2.3, which allow gases to flow through the sample in a closed system. For the *in situ* measurements the setup was the same for MaxLab as for SNBL. For the *in situ* measurements the progress was as follows. Firstly the sample were heated up to 150°C in helium to burn off water and other contaminations. The cell was heated up by electricity, the voltage was increased at the end of each XANES measurement. After the sample was heated in helium, it was further heated to 450°C in propene and oxygen (prop/O_2), at a total flow of 15ml/min. This is to reduce the vanadium species incorporated into the lattice of AlPO-5. When the cell reached the temperature of 500°C, the gases were switched to NO, and the sample cooled in the presence of NO.

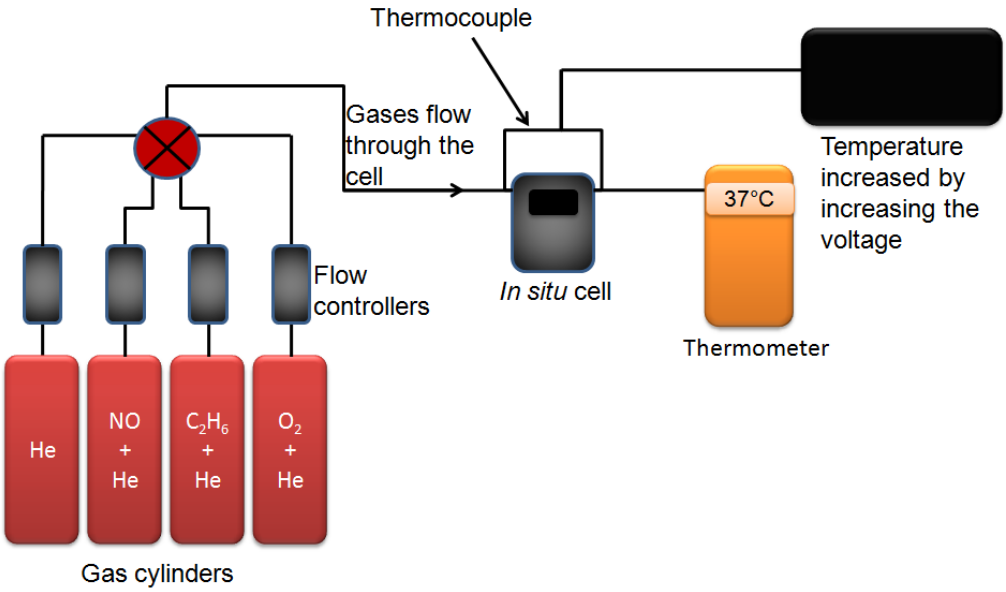

Figure 2.2: The experimental setup for the *in situ* XANES measurements

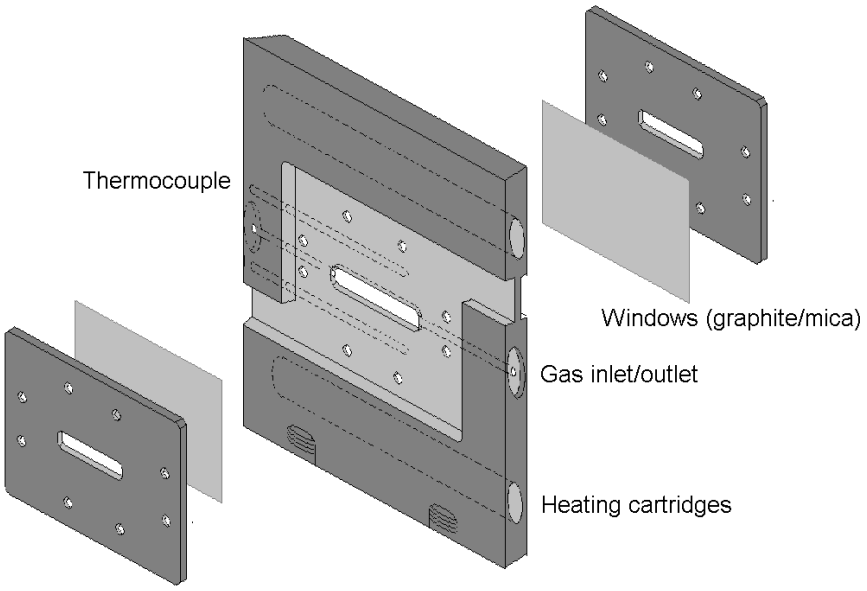

Figure 2.3: The *in situ* cell that was used for the XANES measurements. The cell allows gases to flow through the sample in a cloesd system.(illustration by Karina Mathisen)

Data Reduction

The data from European Synchrotron Radiation Facility, ESRF, and MaxLab were analysed by Athena [44] and Excurve. Athena is a plotting programme, in which the background is subtracted and it is possible to do peak fitting and linear combination analysis. Peak fitting is a way to estimate the area and position of the pre-edges, thereby comparing them to the models.

Data Analysis

The data analysis of the EXAFS measurments was done by using EXCURVE98. EXCURVE98 uses the EXAFS equation shown in Equation 1.23 to refined the parameters. Therefore it is important to be critical, and determine what fit EXCURVE98 suggests is chemically correct. The EXAFS refinements done in EXCURVE98 give information about mulitplicity (N), bonding ditance (R) and thermal vibration (Debye-Waller factor $2\sigma^2$). E_f is the refined

correction of Fermi energy in vacuum compared to E_0 found in Athena. The standard deviation in the last digit of the refinements calculated by EXCURVE98 is given in parentheses in the tables. The deviation of $2\sigma^2$ is $\pm 20\%$. The statistical R-factor is defined as shown in Equation 2.1, and gives an indication of the quality of fit in k-space. Before the EXAFS refinements can be done, the phase shift and backscattering amplitude needs to the calculated , this is done in EXCURVE98 by defining the different atoms present in the sample. When this is done, these parameters can be excluded from the EXAFs equation. EXCURVE98 considers the parameter $S_i(k)$ to be independent through the reduction factor AFAC. The AFAC is a constant which should be close to 1. Since $S_i(k)$ is difficult to determine, the AFAC is calculated for model compounds that are expected to have the same oxidation state as the samples, and transferred to the samples.

$$R = \sum_{i}^{N} [1/\sigma_i(|\chi^{exp}(k) - \chi_i^{th}(k)|] \times 100\% \tag{2.1}$$

Before the samples can be extracted to EXCURVE98, the background needs to be subtracted. This is done in Athena through a spline function. The background should be a smooth line, and follow the EXAFS, and it is important to make sure the background subtraction is done properly. As this can be troublesome with noisy data, when the data are truncated. With XANES scan the data were normalised from 15-150, and EXAFS data were normalised from 150-the end of the spectrum. E_0 can be qualitatively determined in Athena, by going halfway up at the K-edge. Usually the E_0 can be determined from the first peak in the first derivative, however the first peak in the first derivative of vanadium is the pre-edge. The noise after the first peak, makes it hard to determine E_0. As mentioned in section 1.10.2 the pre-edge feature can be refined in order to find the pre-edge position and area.

EXAFS refinements for vanadium is a complicated procedure as the noise is very dominant. It is important to take into account the different k-weightings. For some samples the k^2 weighting gives the most reasonable result, as for

other samples the k^2 weighting gives a higher multiplicty and the uncertainty is higher than for k^3, although the R-factor is smaller. The k-space is usually at 10 $Å^{-1}$ although sometimes it has to be shorter because of the noise. It is very important to subtract the background, deglitch and truncate the data in Athena, before the data are opened in EXCURVE98. Most of the data for vanadium is increasingly noisy with increasing k-space, and there are also several glitches for vanadium. The Debye-Waller factor becomes negative upon refining, which then had to be set at a fixed value.[53] Since the Debye-Waller factor is nearly set at zero, the thermal vibration can almost be disregarded. Thus EXAFS analysis of vanadium is difficult and the R-factor is approximately 50% with noisy data. To achieve better EXAFS with decreasing noise, is to run several EXAFS scan and then sum them up in Athena. This should always be done at least two times, when doing EXAFS of vanadium.

The data from MaxLab is a bit troublesome as the monochromator caused an energy shift several times during the period. Although this is not that influenced when analysing the *in situ* results, as all of the data scans have the same energy correction. A XANES scan at room temperature was done before starting the *in situ* measurement.

2.4.5 TGA

The TGA analysis were carried out using a Perkin-Elmer Thermogravimetric Analyzer (TGA7). Also a Jupiter STA 449C connected to a QMS 403C Aëolos Mass Spectrometer from Netsch has been used to detect the mass loss. A sample is placed into a sample holder, which is set on a balance inside the furnace. The balance is zeroed before the experiment starts. The balance sends the weight signal to the computer for storage along with the sample temperature and elapsed time. In oxidising atmosphere the total flow was 100ml/min with 20ml/min protective gas that was argon, and 80ml/min of air. In reducing atmosphere the total gas flow was 31ml/min, with 11ml/min hydrogen (7%) and 20ml/min argon (93%).

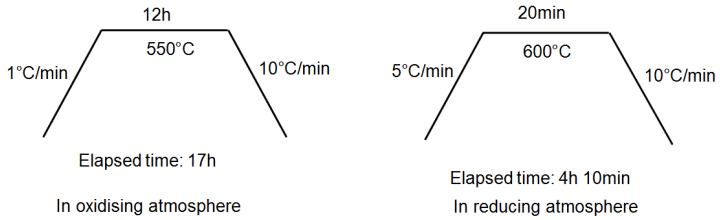

Figure 2.4: Temperature profiles in oxidising and reducing atmosphere.

2.5 Catalytic measurements

The catalytic measurement was done at the University of Newcastle. The experimental rig done for this experiment consist of a catalyst bed connected to four flow meters for appropriate mixing of the gases. Figure 2.6 show the experimental setup of the activity measurements. The output gas from the reactor was detected by a NOx box, which measured the concentration of NOx and NO in gas phase. A bypassline was a reference as the experiment progressed. Prior to the catalytic testing the catalysts were mortared, pressed to pellets and meshed through a sieve, until the catalyst had a pore size between 425-250μm. The gas concentrations and gas flow is shown in table 2.2. The flow was adjusted using a bubble meter. The catalysts were pre-treated by heating in helium as shown in figure 2.5, in order to remove impurities. After the catalyst had cooled to 250°C, the NOx conversion was measured at the temperature range 250°C-500°C. The temperature was increased 50°C, and held for 30min until steady state was reached at each temperature. The conversion of NOx is calculated from the NOx-box which gives both pure NO concentrations and NOx=NO-NO_2 concentration. The conversion of NOx was calculated by Equation 2.2.

$$NOx_{conversion} = \frac{[NOx]_{bypass} - [NOx]_{reactor}}{[NOx]_{bypass}} \times 100\% \qquad (2.2)$$

Table 2.2: An overview of the gas concentration and gas flow used in the activity measurements.

Gas cylinder	Concentration	Gas flow
2.9% NO/He	2000ppm	20.68ml/min
20% O_2/He	20000ppm	30.3m/min
100% He		214.28
C_3H_6 1%	1200ppm	36.14

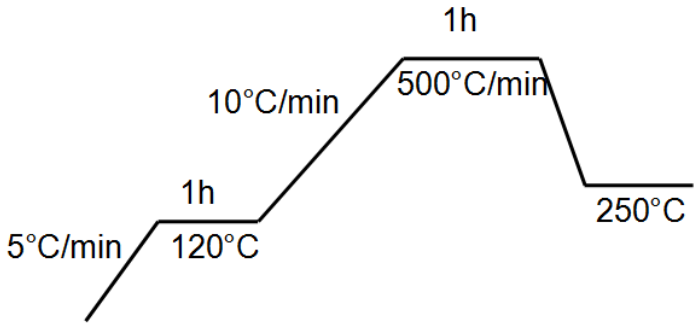

Figure 2.5: A figure of the temperature profile for the pre treatment of the catalyst in order to remove impurities.

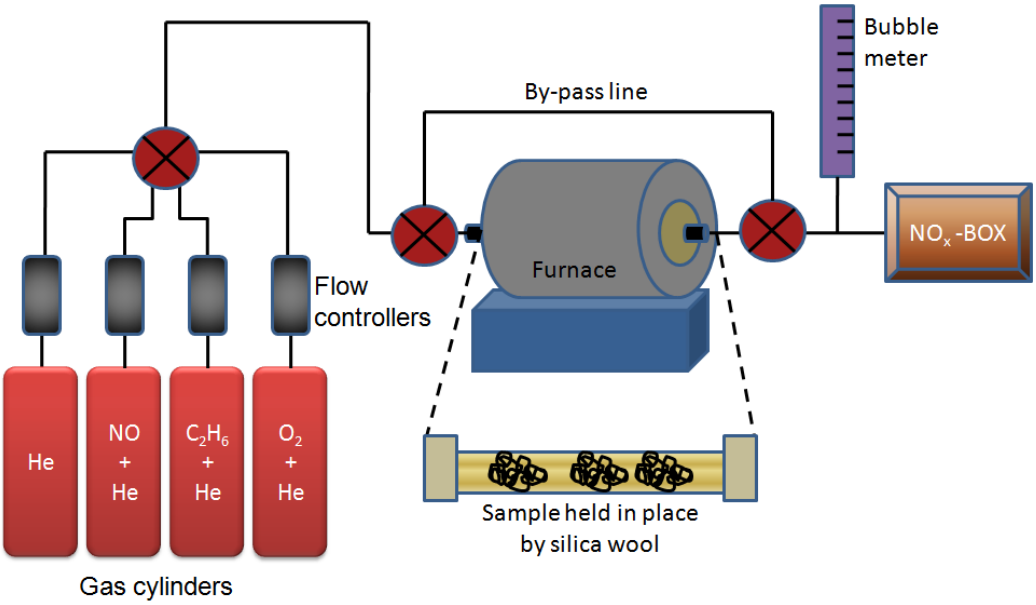

Figure 2.6: The microreactor used for the catalytic measurements

Chapter 3

Results and discussion: The synthesis and characterisation of VAPO-5 and VAPSO-5

3.1 Observation and investigation of the synthesis paramters in VAPO-5 and VAPSO-5

Calcination

For the synthesis of VAPO-5\1(V), vanadium pentoxide was used. At the beginning of the synthesis the color was yellow, and it stayed yellow when it was taken out of the autoclave. After the sample had been calcined it was still yellow.

When $VOSO_4$ was used as the vanadium source the samples were blue at the beginning of the synthesis. After the sample had been taken out of the autoclave it had turned green. When the sample had been calcined it had turned yellow. The oxidation states for vanadium with their respective colors have been explained previously in section 1.6. There it is stated that when vanadium is in oxidation state IV it is blue, and when it is a mixture of IV and V it is green, when the color is yellow it is V. This shows that the vanadium had oxidised from IV to V during calcination, and that it was

partially oxidised during the synthesis as the color had become green. It is stated in several articles that VAPO-5 is oxidised during calcination.[4,53,27] Figure 3.1 show a VAPO-5\X(IV) sample prior and after it had been calcined. VAPO-5\1(V) did not show any color change as it is already in its highest oxidation state.

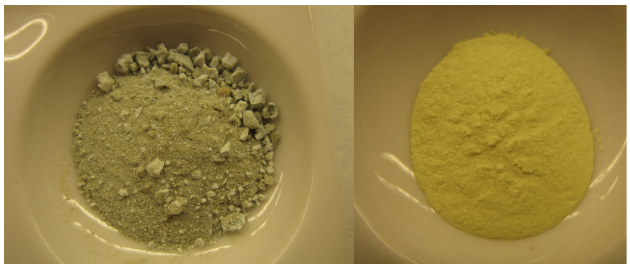

Figure 3.1: The as synthesised to the left and calcined VAPO-5\X(IV)

This effect was also observed with the synthesis of VAPSO-5. However Yu *et al* observed that after the VAPSO-5 was calcined, it had become white.[4] In the article Comparative Study of the Vanadium Species in VAPO-5 and VAPSO-5 Molecular Sieves, it is explained by VAPO-5 and VAPSO-5 are in different coordination states and that the vanadium species in VAPO-5 and VAPSO-5 are different from each other. The vanadium species are further investigated by EXAFS in section 3.3.2.

Figure 3.2 show SEM pictures of calcined VAPO-5\8(IV) The righthand picture is an overview of the particles in VAPO-5\8(IV). As seen in the figure, the particle sizes are not uniform ,but agglomerates with different size and shapes.

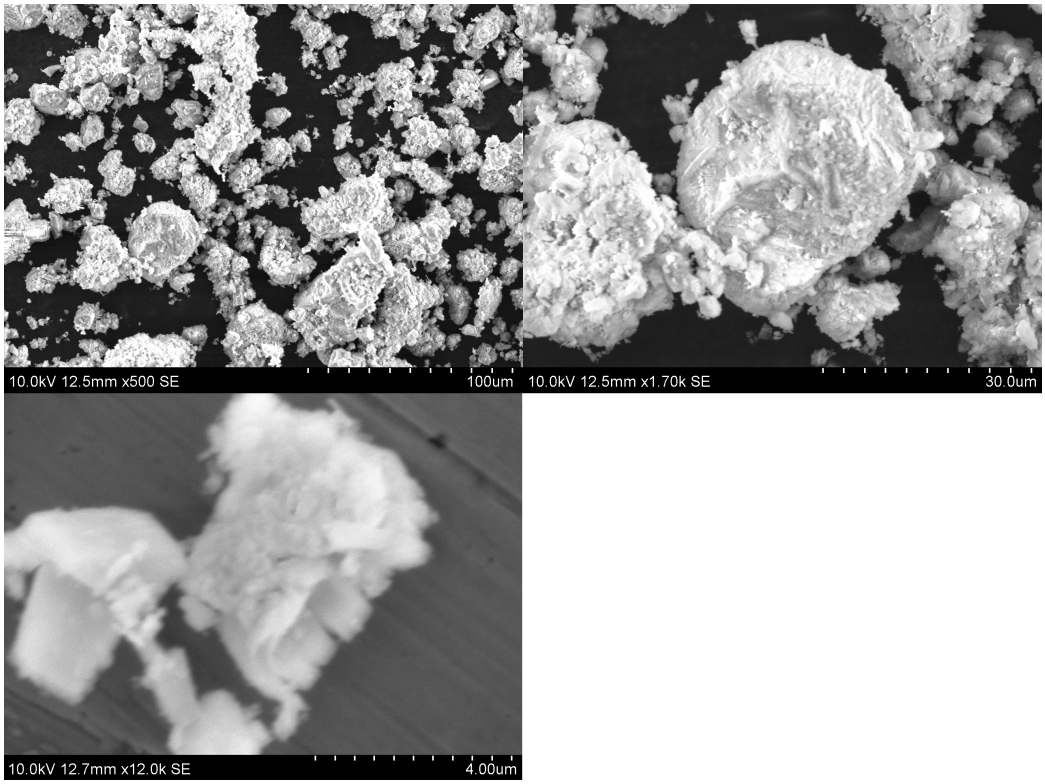

Figure 3.2: SEM pictures of the calcined VAPO-5\8(IV)

Effect of template on VAPO-5

The effect of the template has been studied by using various templates that are known to create AlPO-5. The different templates are shown in table 2.1 under section 2.1. The X-ray diffractogram of VAPO-5\8(IV) with the different crystallisation times is shown in figure 3.3. As the figure show the VAPO-5 was not in phase until 49h. This synthesis was done by using TEA as template. The X-ray diffractogram of VAPO-5\9(V) and VAPO-5\10(IV) is shown in figure 3.4, where tripropylamine was used as a template. Figure 3.4 shows that the VAPO-5 is in phase after 24h, with both V_2O_5 and $VOSO_4$ as the vanadium source.

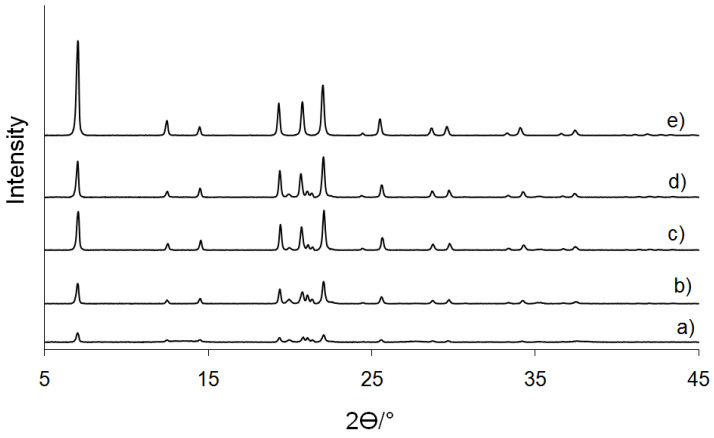

Figure 3.3: The different crystallisation times for VAPO-5\8(IV) as synthesised; a) 4h, b) 6h, c) 9h, d) 24h, e) 49h

Figure 3.5 shows the X-ray diffractograms for the VAPO-5 using DCHA as template. As figure 3.5 show when x=0.05, the AFI structure is intact and increasing the vanadium content to 0.1 the calcined sample of VAPO-5\5(IV) has collapsed.

Figure 3.6 show the XRD diffractogram of as synthesised/calcined VAPO-5\1(V) and as synthesised/calcined VAPO-5\2(IV) as a comparison of the two vanadium sources. As seen in the figure, VAPO-5\1(V) show a perfect crystalline structure, however VAPO-5\2(IV) show some extra peaks as marked in the figure. Which means that the vanadium source contributes to

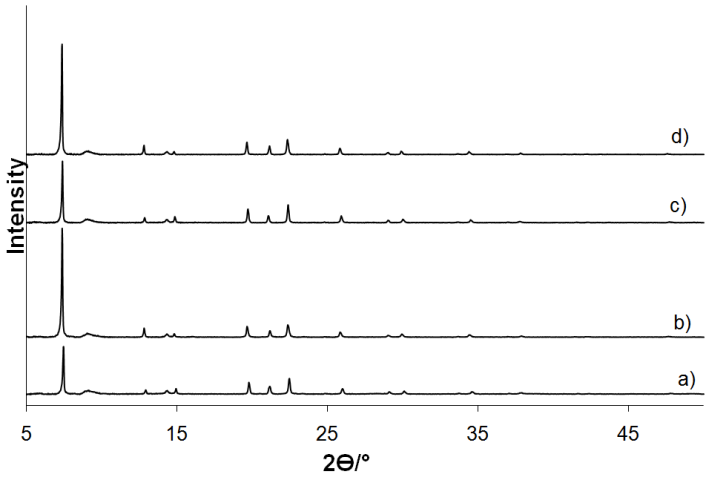

Figure 3.4: The X-ray diffractogram of a) as synthesised VAPO-5\9(V),b) calcined VAPO-\10(IV), c) as synthesised VAPO-5\10(IV) and d) calcined VAPO-5\10(IV).

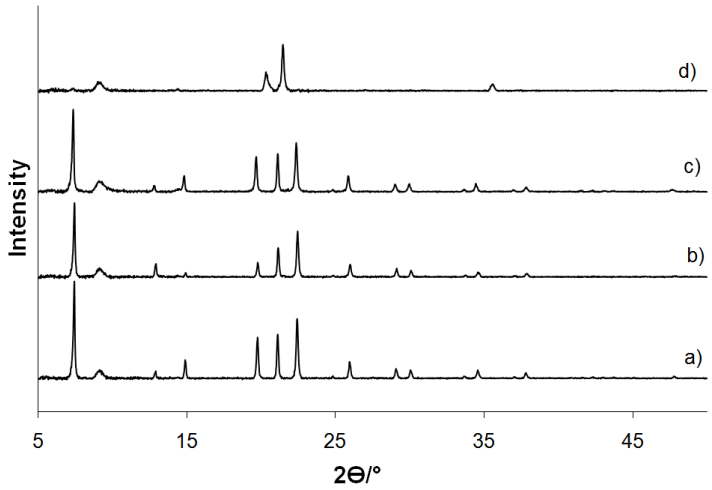

Figure 3.5: VAPO-5 synthesised with DCHA as template; a) is with vanadium content 0.05 as synthesised VAPO-5\6(IV), b) calcined VAPO-5\6(IV), c) is VAPO-5\5(IV) with x=0.1 as synthesised, d) is VAPO-5\5(IV) calcined

the crystallinity. A test in order to see wether the vanadium is incorporated into the structure was done as seen in the figure. The VAPO-5\1(V) was heated to 800°C, since AlPO-5 collapses at 1100°C, introducing vanadium into the framework leads to defects in the strucure. Hence if it was incorporated it would collapse at 800°C as seen for copper if it is incorporated into

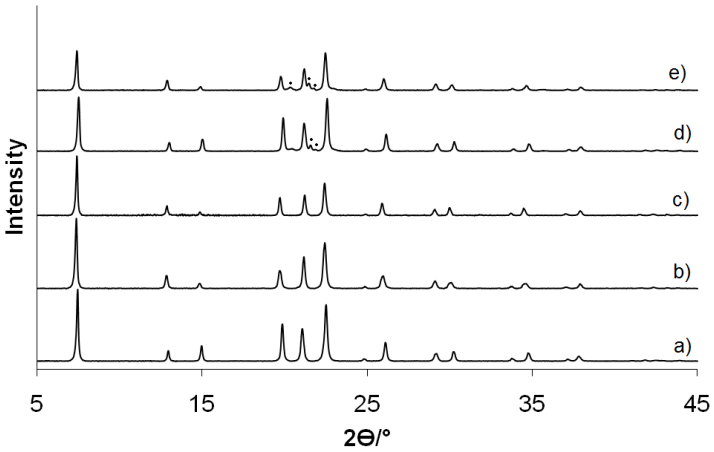

Figure 3.6: a) as synthesised VAPO-5\1(V), b) calcined VAPO-5\1(V), c) calcined at 800°C VAPO-5\1(V), d) as synthesised VAPO-5\2(IV), e) calcined VAPO-5\2(IV)

the framework.[54] As seen in the figure, the structure keeps its crystallinity.

To study the effect of the template during calcination, TGA was done on VAPO-5\8(IV) and VAPO-5\10(IV). Figure 3.7 show that under the heating of VAPO-5\8(IV), the mass loss is divided into two main components. There is a major mass loss from 27°C to 77.7°C were the mass goes from 100% to 96.7%. After this mass loss, the TG curve flattens out until the temperature reaches 228°C. At 228°C and to 423°C mass loss goes from 96% to 92% and then the curve once again flattens out. The total mass loss is 10%. The VAPO-5\10(IV) is also divided into 2 components as shown in figure 3.7. Firstly the mass loss from 27°C to 54°C with a mass loss on 100% to 97%. Then the curve flattens out between the temperature range from 103°C to 238°C, until it loses a lot of mass with the temperature 238°C to 446°C with a mass loss of 95% to 86%, until it again flattens out. The total mass loss of VAPO-5\10(IV) was 15%.

The template is the structure directing agent in the formation of VAPO-5. In order to see if the template contributes to any changes in the surface area of the VAPO-5, BET surface area was measured. Table 3.1 show the measured BET surface area and the vanadium content for the samples. In the table it

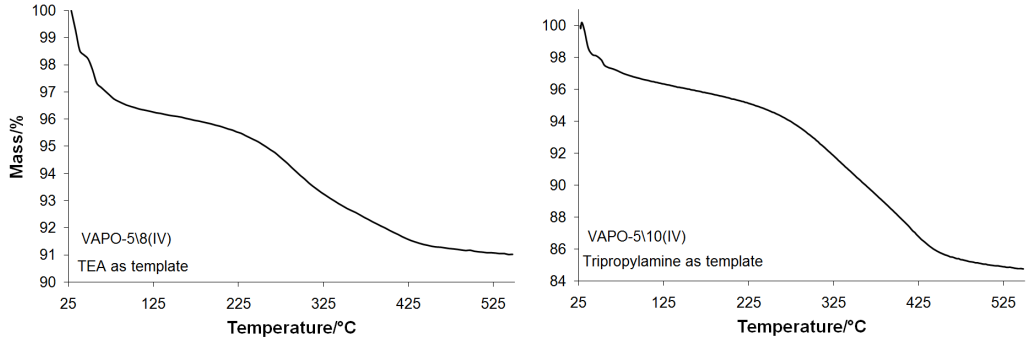

Figure 3.7: The TG curve of the VAPO-5\8(IV) and VAPO-5\10(IV).

is shown that the VAPO-5\1(V) sample has the greatest surface area with a vanadium content of 0.31wt%. VAPO-5\10(IV) has the lowest surface with a vanadium content of 1.14wt%.

Table 3.1: Results from the elemental analysis and the BET measurements

Sample	BET surface area\m^2 g^{-1}	Elemental analysis	V w%	RSD%
VAPO-5\10(IV)	246.9		1.14	0.9
VAPO-5\1(V)	285.1		0.31	2.4
VAPO-5\2(IV)	278.02		0.9	2.3
VAPO-5\5(IV)			1.99	

Montes *et al* stated that VAPO-5 was crystallised after only 4h, and that it stays pure after that time. Montes *et al* used tripropylamine as template for the synthesis of VAPO-5. When TEA was used a the template the sample had to crystallise for over 24h, and it is pure after 49h, as shown in figure 3.3. As for the samples when tripropylamin was used as a template, the sample was in phase after 24h. The VAPO-5\5(IV) with the same initial vanadium content as the other samples (x=0.1), show a loss in the characteristic peaks which is distinct for the AFI structure. This is an indication of berlinite, which is the collapsed form of AlPO-5. Hence the DCHA template should either been heated for a longer time such as VAPO-5\8(IV) or it is because it is not stabile enough for the high thermal treatment when the sample is calcined.

Figure 3.7 show the TG curve as descibed above. The TG curve for VAPO-5\10(IV) show a greater total mass loss than VAPO-5\8(IV) and the mass loss is greatest at the end of the measuremnt. As for VAPO-5\8(IV) the total mass loss is 10% and is greatest at the beginning of the experiment. This could be the effect of template, although is should also be pointed out that VAPO-5\10(IV) has a greater vanadium content, as shown in table 3.7, which makes these two samples not completetely comparable.

Table 3.1 show an increased surface area when TEA is used as the template, however it results in a lower vanadium content. VAPO-5\5(IV) has the highest vanadium content in which the DCHA template is used. This suggests that the template affect the vanadium content in VAPO-5. Hence it can bli concluded that the choice of template is crucial for the outcome of the synthesis. The properties of these materials with the different templates should be investigated, as there are different applications for VAPO-5.

As seen in figure 3.6 VAPO-5\1(V) is not collapsed when it is heated to 800°C. This could be because vanadium is incorporated into the framework, and the framework is stabilised.

Vanadia loading

The vanadia loading in VAPO-5 and VAPSO-5 have been investigated as shown in table 2.1. Table 3.2 show the VAPO-5 samples with different vanadia loading and the elemental analysis of the samples.

VAPO-5\5(IV) has the highest vanadium content of 1.99wt% as seen above. The lowest vanadium content in which the initial mole composition of vanadium was 0.1 is 0.31 in VAPO-5\1(V). The table show, as mentioned above, that the choice of template is a factor concerning the uptake of vanadium in VAPO-5. The VAPO-5\5(IV) has the highest vanadium content according what has been added to the synthesis. However as figure 3.5 shows, the calcined sample seems to have the collapsed form of berlinite. This indicates that higher vanadia loading results in instability of the structure after the

Table 3.2: Final and initial vanadium content in VAPO-5

Sample	Initial composition	Final composition		RSD %
	V	Final Product	V wt%	
VAPO-5\1(V)	0.1	$V_{0.01}AlP_{0.98}O_4$	0.31	2.4
VAPO-5\2(IV)	0.1	$V_{0.02}AlP_{0.91}O_4$	0.9	2.3
VAPO-5\3(IV)	0.01	$V_{0.003}AlP_{1.1}O_4$	0.0188	3.6
VAPO-5\5(IV)	0.1	$V_{0.06}AlP_{0.97}O_4$	1.99	1.7
VAPO-5\6(IV)	0.05	$V_{0.02}AlP_{0.85}O_4$	0.77	1.2
VAPO-5\9(V)	0.18	$V_{0.04}AlP_{0.53}O_4$	1.51	0.9
VAPO-5\10/IV)	0.18	$V_{0.03}AlP_{0.5}O_4$	1.14	0.9
VAPSO-5\4(IV)	0.05		0.97	2.3

[a] It was not possible to calculate the ratio of VAPSO-5, because it was dissolved in HF during the elemental analysis. AlF is precipitated, and therefore the Al ratio is not correct.

tempalt has been removed. This has also been reported in other articles.[55] However if the sample had been allowed to crystallise longer as for VAPO-5\8(IV) 49h, it might have been stable. Wechuysen *et al* observed that with increasing vanadium content, the formation of VAPO-5 from pseudoboehmite required a longer synthesis time. They found out that the optimal synthesis time was between 48h and 120h. This can be correlated to the surface area from the BET measurements.

Table 3.1 suggests that with increasing vanadium loading, the surface decreases. This could be explained by the fact that the incorporation of vanadium introduces defects into the framework, and then decreases the surface. Wechuysen *et al* also claimed that the AFI phase could not be obtained with a vanadium mole ratio above 0.08. As been shown above, most of the VAPO-5 are in phase after 24h, with a mole ratio higher than 0.08.

The elemental analysis for VAPSO-5\4(IV) is 0.97wt%, which is higher than some of the VAPO-5 samples considering the amount of vanadium added. Unfortunately there was no time to take elemental analysis on the other VAPSO-5 samples. However several of the VAPSO-5 samples show a less crystalline structure as shown in figure 3.8 where the XRD diffractograms for some VAPSO-5 samples with different silicon and vanadium content is presented.

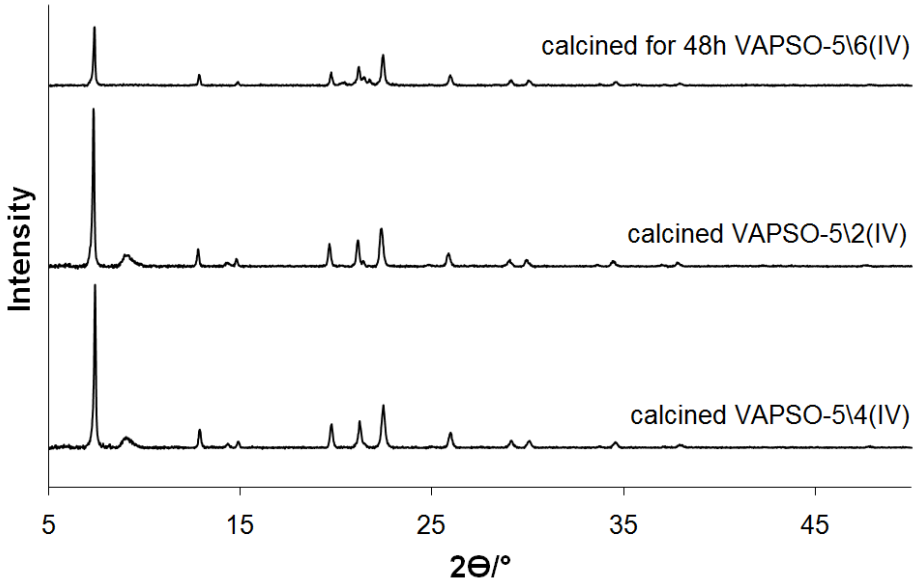

Figure 3.8: The XRD diffractogram of calcined VAPSO-5\4(IV), calcined VAPSO-5\2(IV) and calcined for 48h VAPSO-5\6(IV).

Figure 3.8 show that with either increasing vanadium content or silicon content the VAPSO-5 sample become less crystalline. To investigate the effect of crystallisation time for VAPSO-5\6(IV), the sample was crystallised for 48h and for 6 days. The one that was crystallised for 6 days was suspected to be more crystalline. However the calcined sample of VAPSO-5\6(IV) which crystallised for 6 days collapsed when the template was removed. This can be assigned to as longer the synthesis was crystallised, more vanadium was incorporated, which led to instability in the structure. Where upon calcination the structure collapsed, since the as synthesised sample showed a crystalline structure of SAPO-5.[4] Yu *et al* discovered that in VAPSO-5 it is possible to

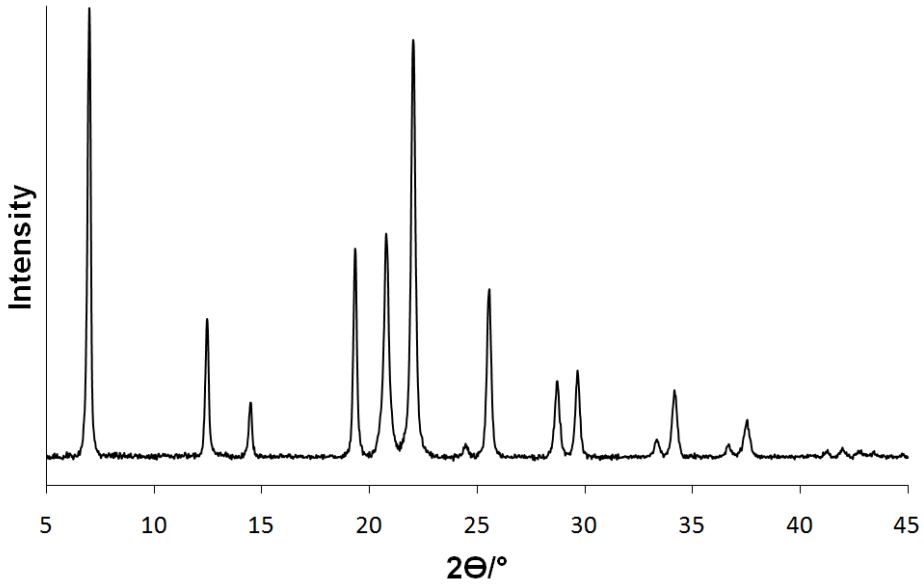

Figure 3.9: The calcined VAPSO-5\5(IV)

add more vanadium as silicon stabilised the structure. This have not been observed in this thesis. Although this difference could be explained by the synthesis procedure as the silicon source was added in the end in this thesis. Yu *et al* added the silicon at the same time as vanadium was added.

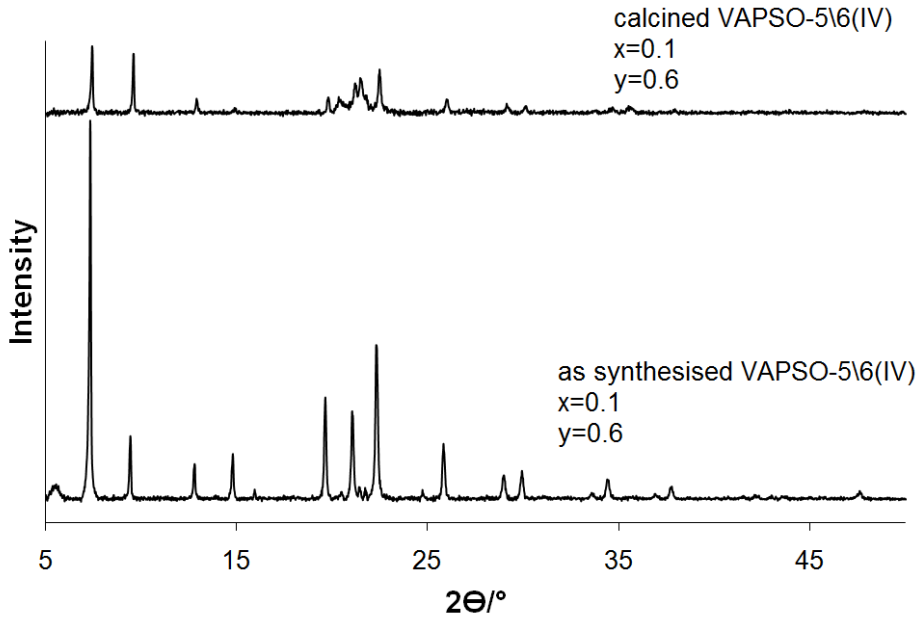

Figure 3.10: The as synthesised and calcined VAPSO-5\6(IV) which was crystallised for 6 days; x= vanadium ratio inserted in the synthesis, y= silicon ratio inserted in the synthesis.

It is concluded in this thesis that it is not possible to have a complete ratio of vanadium and silicon at the same time, because the structure becomes too unstable. However this could be due to the synthesis procedure. The vanadium content in VAPSO-5 seems to be higher than the VAPO-5 samples considering the amount of vanadium added to the synthesis. Before final conclusions can be made on this subject, the vanadium content in the other VAPSO-5 samples need to be investigated.

3.2 X-ray absorbtion near edge spectroscopy

3.2.1 Oxidation states of vanadium models and VAPO-5 and VAPSO-5

XANES is a very useful part of the XAS spetrum to distinguish between different oxidation states of the metal of interest. Here different XANES for the vanadium samples were investigated. To be able to decide which oxidation state the samples are in, it is important to use reference models. As mentioned in section 3, it was observed a color change before and after calcination when $VOSO_4$ was used as the vanadium source. It was suggested that the VAPO-5 samples oxidised from tetravalent vanadium to pentavalent vanadium. To verify this observation a XANES study of the samples and the reference models have been done. The reference models were V_2O_5 which is as mentioned pentavalent and therefore is a reference for vandium in oxidation state V, and $VOSO_4$ which is a reference for oxidation state IV. Figure 3.11 show a comparison of the XANES for the reference models and for VAPO-5\8(IV) calcined and as synthesised. The figure show that the XANES for the calcined VAPO-5\8(IV), is shifted towards higher energies than the others. The pre-edge of the calcined VAPO-5\8(IV) is also the most intense. The XANES of the bulk $VOSO_4$ is shifted to lower energies than the others, and the pre-edge intensity is higher than for the as synthesised sample. Ideally the calcined VAPO-5\8(IV) and the bulk V_2O_5 should overlap as they are both in oxidation state V. The pre-edge intensity for the bulk $VOSO_4$ should be lower than that for as synthesised VAPO-5\8(IV) as it is between oxidation state IV and V. This can be explained by the effect of different chemical environment, which leads to shifts in XANES. Therefore are these reference samples not applicable to the VAPO-5 samples. Hence it was therefore important to find better reference models,which was further investigated in section 3.2.2.

Figure 3.12 show different VAPO-5 samples. The pre-edge of the as synthesised VAPO-5\8(IV) is shifted to lower energies than that for the calcined

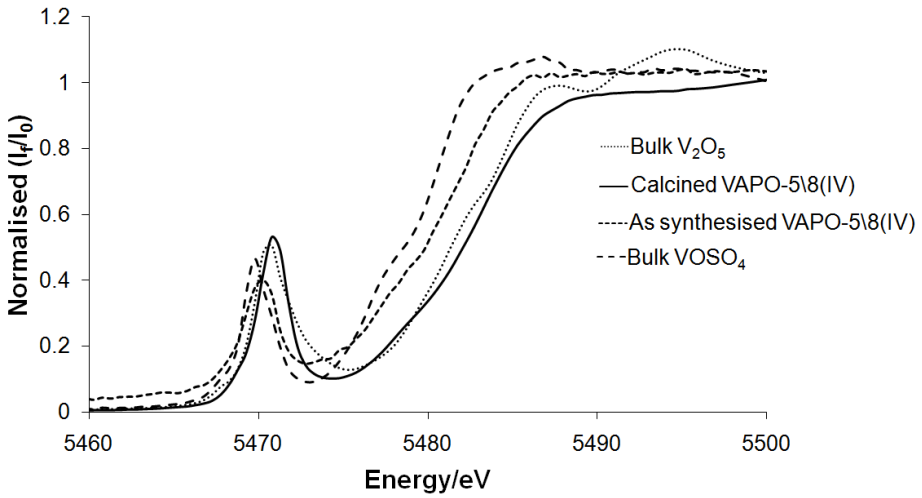

Figure 3.11: XANES for the reference models and calcined and as synthesised VAPO-5\8(IV).

sample. The pre-edge of the as synthesised VAPO-5\10(IV) is at the same position as the calcined pre-edge. The pre-edge position of the as synthesised VAPO-5\1(V) sample is the same as for the calcined VAPO-5\1(V). The position of the K-edge for all the calcined VAPO-5 samples are shifted to higher energies. By studying the XANES of the VAPO-5 samples it is possible to qualitatively determine the oxidation state. As mentioned under section 1.9.1 the pre-edge feature is dependent upon several factors:

- the local geometry
- hybridisation of 3d- and 4p-orbitals
- the valence state
- the effect of the ligand (the molecular cage effect)
- coordination number

The effect of the oxidation state is observed in the comparison of the as synthesised and calcined VAPO-5 samples. The calcined and as synthesised VAPO-5\1(V) does not show a a pronounced alteration in XANES, as it is

already in oxidation state V. The change that is observed can be assigned to water loss, and then vanadium might rearrange its bonding arrangement during calcination. The pre-edge feature of the as synthesised VAPO-5\10(IV) sample, has a weaker pre-edge intensity than the calcined sample. This feature is because of difference in the oxidation state of the as synthesised and calcined sample. Hence it is a confirmation that the vanadium is oxidised upon calcination. Unfortunately a qualitative study like this cannot say anything about the degree of pentavalent and tetravlent vanadium in the VAPO-5 samples. However the pre-edge position for the as synthesised sample of VAPO-5\8(IV) is shifted to lower energies than the calcined sample. This is not observed for the other VAPO-5 samples in the figure. Referring to the theory in section 1.9.1, this indicates that the as synthesised VAPO-5\8(IV) has a higher degree of tetravalent vanadium than the other as synthesised VAPO-5 samples.

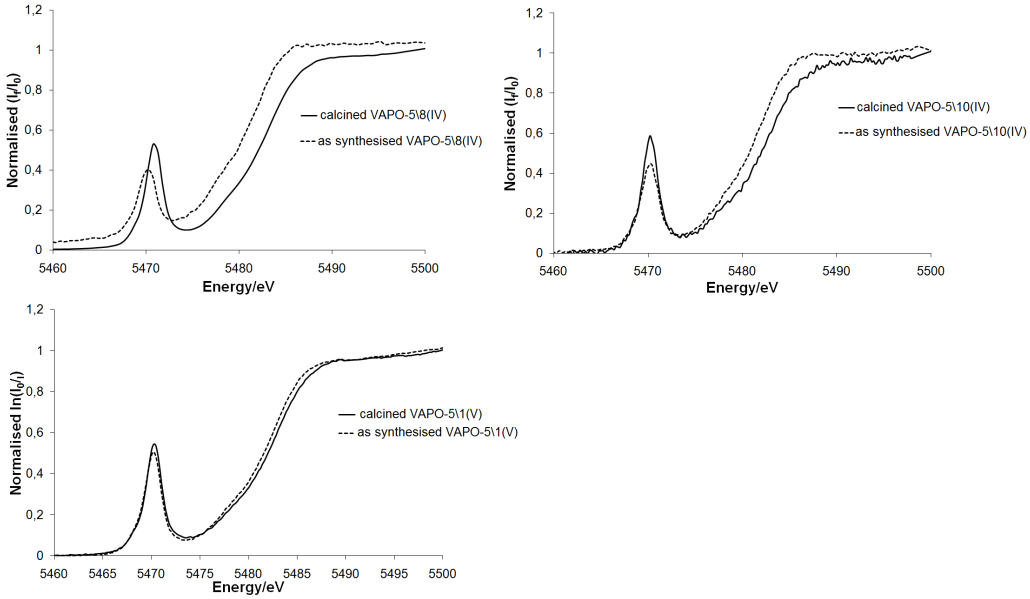

Figure 3.12: The XANES of different VAPO-5 samples. By studyng the XANES it is possible to qualitatively determine the oxidation state.

3.2.2 XANES analysis of vanadium in solution

Comparison of XANES of aqueous solution of vanadium in various oxidation states are ideal as the chemical shift can be ignored. The data for the vanadium solutions were collected at Dubble at ESRF. The K-edge of vanadium was studied for the different solutions.

As mentioned in subsection 1.9.1, the geometry and symmetry of the molecules represent a big impact on the pre-edge feature. This will be shown in the results from the XANES region of the vanadium solutions.

The pentavalent and tetravalent vanadium solutions were mixed together with different ratios. This yielded vanadium with various degree of oxidation state IV and V. The idea was to employ the vanadium solutions as references to the as synthesised samples. This is applicable as the samples are all mixtures of valence state IV and V.

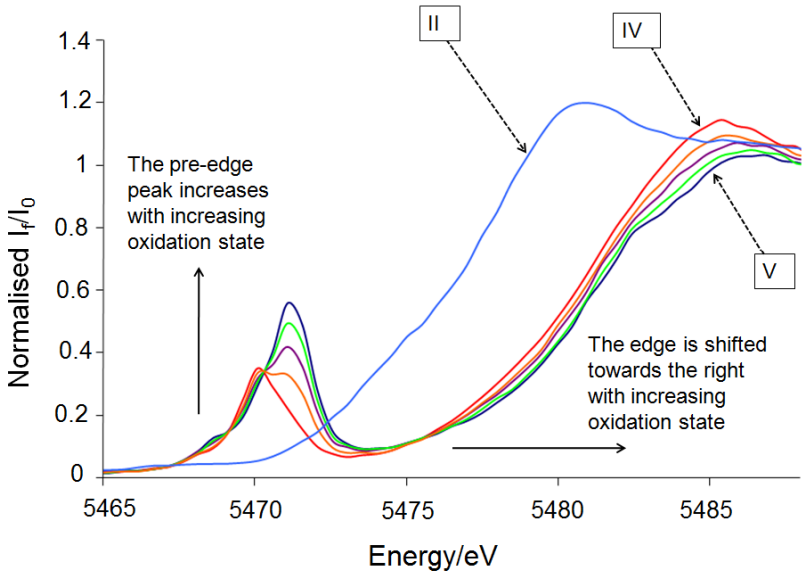

Figure 3.13: The XANES for the vanadium solutions. As shown in the figure the pre-edge area increases with increasing oxidation state.

Figure 3.13 show that the divalent vanadium solution has no pre-edge. This is consistent with what have been described under subsection 1.6. That divalent

vanadium in solution has a octahedral symmetry and the 1s→3d transition is laporte forbidden. The pre-edge features of the other solutions are visible since they have a distorted octahedral symmetry where the centre of inversion is broken, in which the 1s→3d transition becomes allowed. The pre-edge of the tetravalent vanadium is shifted to lower energies when compared to figure 3.13. This is most likely the cause of the valence state. For valence state IV less energy is required to excite from 1s→3d, the pre-edge feature is vicible at lower energies. This is also evident in the vanadium solution with 3:1 relationship between IV and V respectively, which seems to have two pre-edges. This could be that the two oxidation states are both detected in the solution. In the solutions where there are a higher degree of pentavalent vanadium, that becomes dominant, and the pre-edges are located at higher energies. The pre-edge area is lower with a decreasing degree of V. The pre-edge areas are refined and shown in table 3.3.

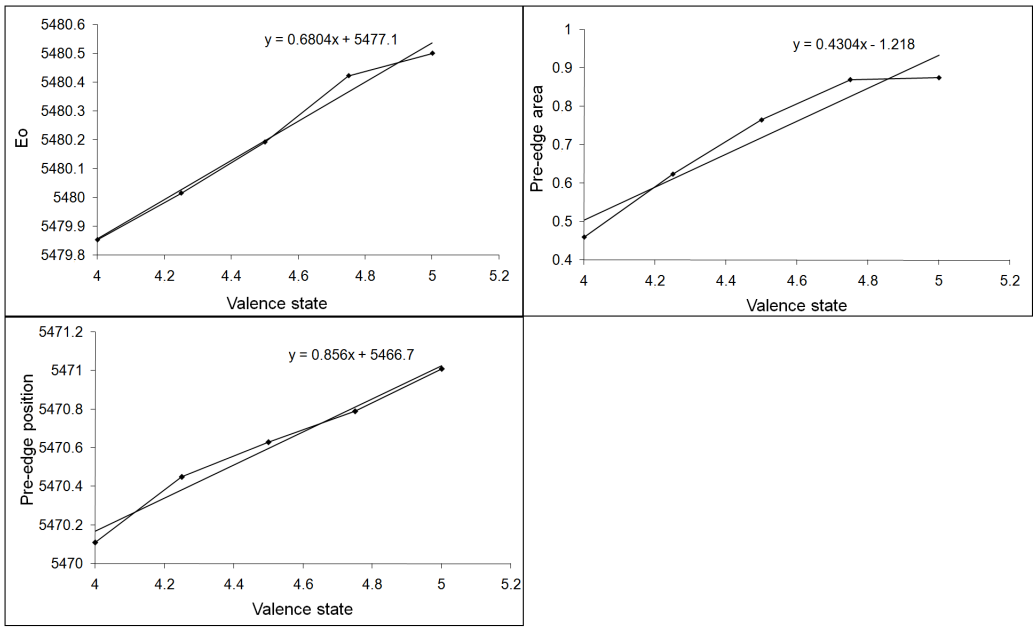

Figure 3.14: The correlation of the threshold energy (E_0) , the pre-edge area, the pre-edge position and the valence state

Figure 3.13 shows a clear correlation between oxidation states and energy treshold (E_0) as expected, but also both position and area of the pre-edge correlates with the oxidation states. This is consistent with the theory related

to the pre-edge feature explained in subsection 1.9.1. As shown in figure 3.14 the relation between the oxidation states and the other factors were calculated by linear regression, which in theory could be employed on the VAPO-5 and VAPSO-5 samples. Although this is not applicable, as vanadium solutions and the samples have different geometry and environment. As already mentioned the pre-edge feature is sensitive to the local geometry, and this is why these vanadium solutions cannot be used to calculate the degree of IV and V in the VAPO-5 and VAPSO-5 samples. As shown in figure 3.15 where V_2O_5 does not overlap with the XANES of VO_2^+ because of their different chemical environment and geometry as shown in subsection 1.6.

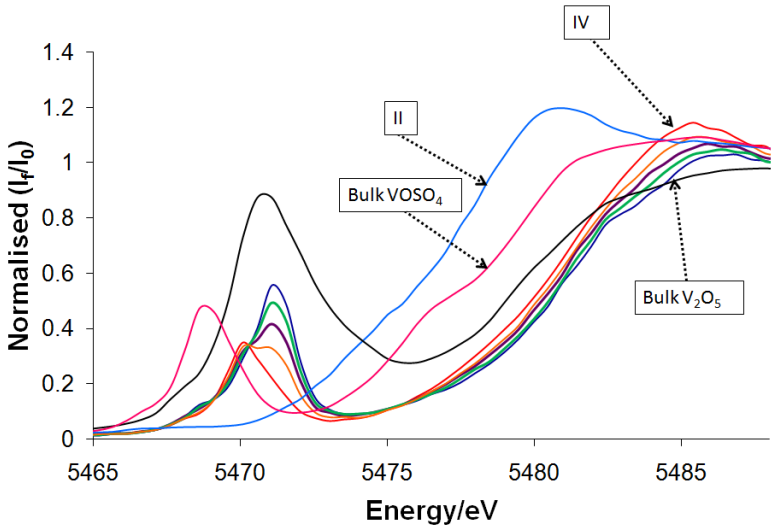

Figure 3.15: The vanadium solutions with the solid models of V_2O_5 and $VOSO_4$.

The geometry of the complex $[VO_2(H_2O)_4]^+$ is distorted octahedra with a C_4v symmetry, which according to the character table will have 3d-4p mixing. The geometry of V_2O_5 is square pyramidal with a C_s symmetry and has also a 3d-4p mixing according to the character table. Hence it is the effect of chemical shift on the K-edge position, the local geometry effect on the pre-edge and the molecular cage effect. The molecular cage effect depends on what type of ligand, and how much these overlap. The $VOSO_4$ has also a difference in the chemical shift on the K-edge for the V(IV) in solution, but there is also a difference in the pre-edge intensity and position. This is an

Table 3.3: A table over the area and position of th pre-edges for hte vanadium models in solutions. The result is obtained by peak-fit Athena

Sample		Centroid/eV[a]	Area	R-factor
Ratio VO^{2+}	Ratio $VO_2{}^+$			
1	0	5470.1(5)	0.46(7)	0.00328
0	1	5471.0(2)	0.88(6)	0.00252
1	1	5470.6(2)	0.77(7)	0.00266
3	1	5470.5(4)	0.62(7)	0.00233
1	3	5470.8(3)	0.87(7)	0.00331

Sample	Centroid	Area	R-factor
V_2O_5	5472.5(3)	2.7(3)	0.00301
$VOSO_4$	5470.1(5)	0.8(1)	0.00616

[a] The position of the pre-edge is difficult to calculate with the peak-fit function in Athena. Therefore the pre-edge position was qualitatively found in Athena when the pre-edge position and valence state was plotted against eachother in figure 3.14

interesting feature as the solid $VOSO_4$ has the same symmetry and geometry as the V(IV) solution. Therefore this could be the molecular cage effect, as they have different types of ligands. Table 3.3 show the refined pre-edge area and position. As figure 3.15 show, the position of the bulk $VOSO_4$ is shifted to a lower energy than the VO^{2+} solution. Although this is not observed in the table, this is mostly because the peak-fit function in Athena has a hard time to give correct values of the pre-edge position.

Figure 3.16 show the correlation between the pre-edge area and position. As the figure show the pre-edge position is shifted to higher energies as the pre-edge area increases. This show that there is a correlation between the pre-edge position and the area. This is expected since there is a correlation with the pre-edge position and the oxidation state, and the area and oxidation state. The bulk V_2O_5 has a more intense pre-edge and is shifted towards higher energies than the $VO_2{}^+$.

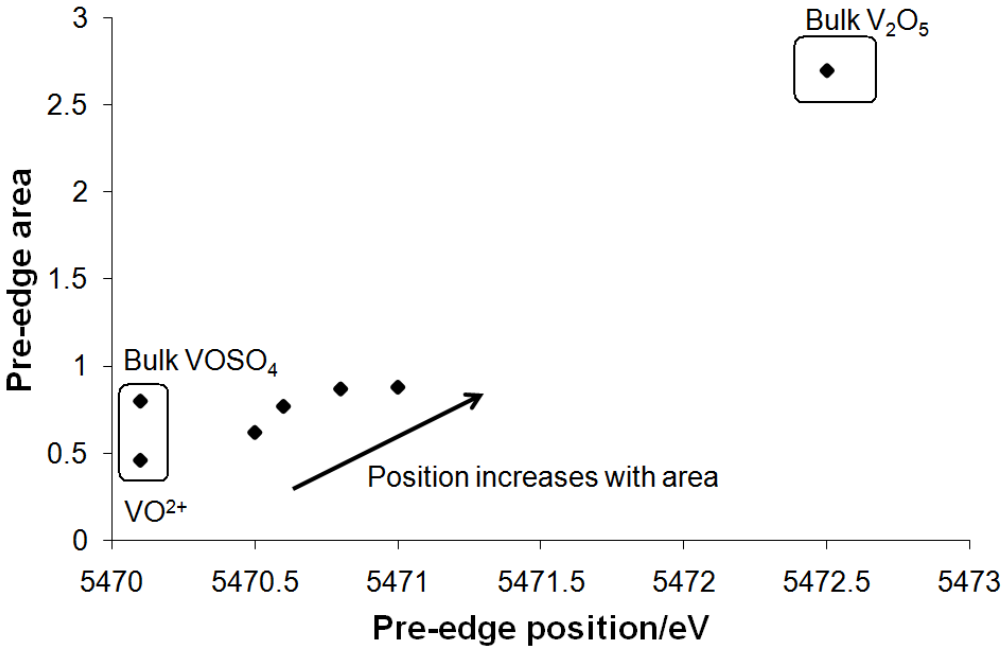

Figure 3.16: A plot of the pre-edge area vs the pre-edge position. The dots that are not marked are the ones that are shown in table 3.3

3.3 Extendend X-ray Absorption Fine Structure, EXAFS

3.3.1 Reference models

Reference models are used to be able to distinguish bond distances that are distinct for some vanadium bonds, such as the vanadyl group (V=O). Vanadium pentoxide is used as a pentavalent model, and vanadyl sulfate is used as the tetravalent model. AFAC correlates with the type of element and with oxidation state. Therefore the AFAC for the reference models are done first, and then they are transferred to the VAPO-5 and VAPSO-5 samples that have the same oxidation state. The parameters for the vanadium foil is refined, in order to see if there are any vanadium-vanadium distances in the VAPO-5 and VAPSO-5 samples.

The vanadium foil

The refined data for the vanadium foil are shown in table 3.4.

Table 3.4: The refined EXAFS parameters for the vanadium foil. The AFAC was determined to be 0.77.

Sample	Shell	N	R/Å	R/Å[a]	2σ/Å^2	Ef	R/%
Vanadium foil	V-V	8	2.623(7)	2.625	0.015(1)	-15.7(8)	52.31
	V..V	6	3.02(1)	3.027	0.017(3)		

[a] The radial distance found in literature.[56]

The EXAFS and its Fourier Transform are shown in figure 3.17.

V_2O_5-model

The results from the EXAFS refinements are shown in table 3.5 and the EXAFS and its Fourier transform are shown in figure 3.17

Table 3.5: The EXAFS refinements for bulk V_2O_5

Sample	Shell	N[a]	R/Å	R/Å[b]	$2\sigma/Å^2$	Ef	R/%
bulk V2O5	V-O	1	1.58(1)	1.576	0.006(3)	-1.002(5)	45.48
		3	1.87(1)	1.828[b]	0.011(8)		
		1	2.18(2)	2.017	0.010(7)		
		1	2.70(3)	2.793	0.005(8)		
		2	3.10(1)	3.082	0.011(3)		
		3	3.5(2)	3.496[b]	0.08(7)		

[a] The fixed mulitplicities and the radial distances are taken from the references.[56]
[b] Two shells were added together and the mean value was used.

Vanadyl sulfate

The refined parameters are represented in table 3.6. Figure 3.17 show both the experimental and theoretical curve for the refined data.

Table 3.6: The EXAFS refinements of $VOSO_4$. The AFAC was determined to be 0.62

Sample	Shell	N[a]	R/Å	R,XRD/Å[a]	$2/Å^2$	Ef	R/%
VOSO4	V-O	1	1.61(1)	1.63	0.004(4)	-1.47(7)	35.10
	V-O	4	2.039(6)	2.04	0.011(2)		
	V-O	1	2.38(39	2.47	0.009(9)		

[a] The fixed multiplicities and crystallographic distances were taken from references.[57]

The refined data for the reference models correlates well with what is found in litereature. Thereby it is possible to transfer the AFAC from the reference models to the samples.

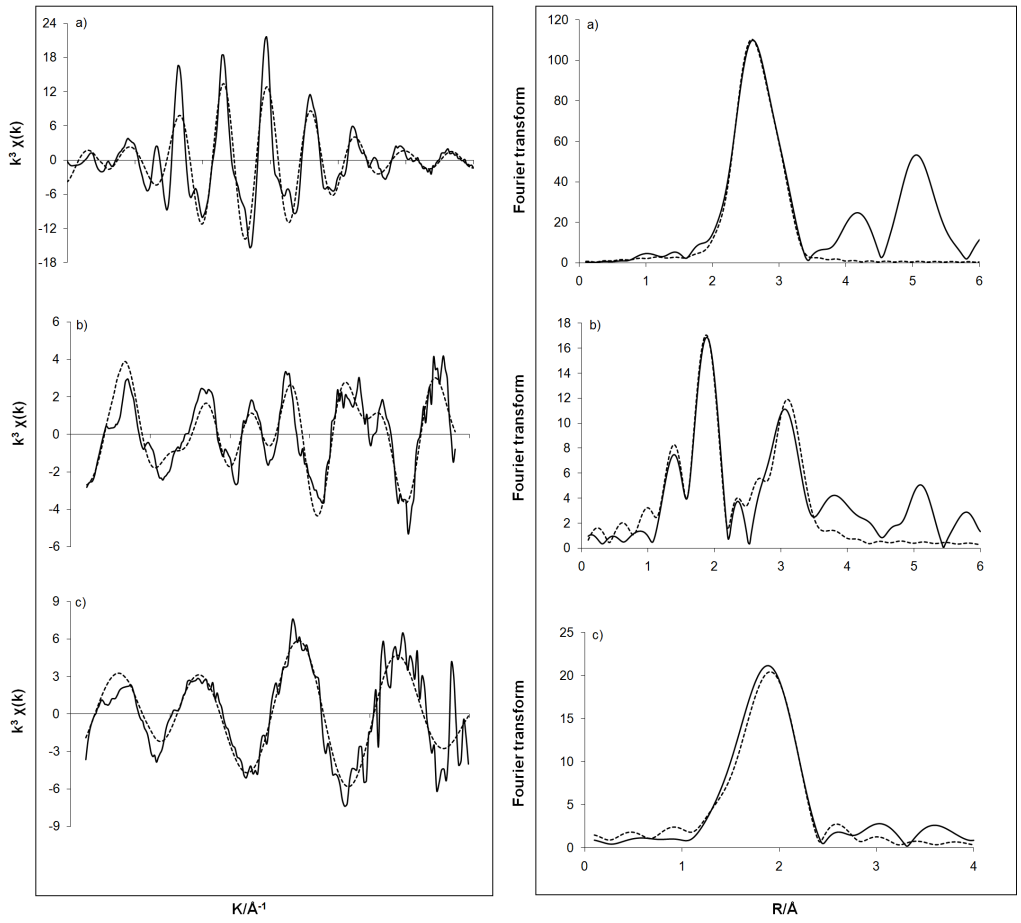

Figure 3.17: Experimental (-) and theoretical ($\cdots$) k^3-weighted EXAFS and its Fourier Transform for: a) Vanadium foil k=2-14Å^{-1}, b) bulk V_2O_5 k=2-12Å^{-1}, c) bulk $VOSO_4$ k=2-10Å^{-1}.

3.3.2 EXAFS refinements of VAPO-5 and VAPSO-5

As mentioned in Section 1.11 EXAFS on vanadium is troublesome because of the low signal to noise ratio. Different weighting schemes have been used in order to see what gave the best fit. When the Debye-Waller factor was refined, they always became negative. Therefore they were fixed at a certain value, 0.0003Å^2 in accordance with literature.[53] The AFAC was transferred from the vanadium models and to the samples. This gave a multiplicity that is not chemical correct according to the bonding distances and the coordination number. Although the same refining procedure was done for alle of the vanadium samples, therefore they are comparable with eachother. It is also been reported negative Debye-Waller factors in literature, and the multiplicity had to be set in order to obtain reasonable data.[29] In this thesis it was chosen to set the Debye-Waller constant, and refine the other values.

As synthesised and calcined VAPO-5\8(IV)

The as synthesised and calcined sample of VAPO-5\8(IV). The parameters from the least squares EXAFS refinements are shown in table 3.7.

As seen in figure 3.18, the k-space is from 2-8Å^{-1}. It had to be cut because the data had only noise at higher k. This refining was first done by k^3 weighting, but the R-factor was better with k^2 weighting. If k^3 weighting was used the multiplicity became larger. This could be explained by the theory of Teo and Lee[36]. They suggested than one should use k^1 weighting when $Z>57$, k^2 if $32<Z<57$, and k^3 $Z>36$. With higher weighting the signal is amplified, and therefore with noisy data, the noise would also be amplified. Hence it would be favourable to use lower weighting than k^3, which is the most widely used weighting. The advantage of the k^3 weighting is that it has the ability to weight the EXAFS signals more uniformly over the data range of k= 3-16Å^{-1}. The k^3 weighting also assures that chemical effects on the EXAFS information are minimized. The weighting scheme may have significant effects on the peak heights and peak positions in the Fourier Transform.

Table 3.7: EXAFS refinements of as synthesised VAPO-5\8(IV). AFAC was 0.62 and was taken from the $VOSO_4$ model. For the calcined sample of VAPO-5\8(IV) the AFAC was 0.55 and taken from the model compund V_2O_5

Sample	Shell	N	R/Å	2σ/Å^{2a}	Ef	R/%
as synth VAPO-5\8(IV)	V-O	0.6(3)	1.74(3)	0.0003	-8(1)	45.41
	V-O	2.7(4)	2.1(2)	0.0003		
	V$\cdots$O	1.6(4)	2.54(4)	0.0003		
	V$\cdots$Al	0.6(6)	3.3(1)	0.0003		
calcined VAPO-5\8(IV)	V-O	1.7(2)	1.644(1)	0.0003	4(2)	47.94
	V$\cdots$O	1.0(3)	1.87(2)	0.0003		
	V$\cdots$O	1.3(5)	2.45(2)	0.0003		

[a] The Debye-Waller was set at 0.0003Å^2 because the value always became negative.The value was taken from references.[53]

It is not wrong to use the k^2 weighting, but it is less common than the k^3 weighting. According to what weighting scheme is used, it is reflected in the multiplicity. With some data the k^2-weighting gives a negative multiplicity, therefore when the data was refined, both of the weighting schemes were used, to see what gave the most reliable result.

The calcined sample of VAPO-5\ 8 (IV) gave a better fit with k^3 weighting. When k^2 weighting was used the mulitplicities became negative. Figure 3.18 show the EXAFS and its Fourier transform for the VAPO-5 and VAPSO-5 samples discussed in this thesis. As seen in table 3.7 vanadium loses the last shell upon calcination. This is a further indication of vanadium rearranges upon calcination as proposed in Section 3.2.1. In the last shell of aluminium the multiplicity is shown to be quite low this could be the effect of aluminium having slightly different bond distances, and thereby giving a lower multiplicity. The last shell observed in the as synthesised sample was not present in the calcined sample. A possible explanation of this is the environment is

altered as vanadium enters the framework sites of different symmetries. The resulting V$\cdots$Al distances are thereby so close and within a low intensity, which is then referred to as noise when the vanadium data are refined. This is supported by references.[54]

As synthesised and calcined VAPO-5\10(IV)

This sample was synthesised by using $VOSO_4$ as the vanadium source and tripropylamine was used as the structure directing agent. Results from the EXAFS refinements are shown in table 3.8.

Table 3.8: The refined EXAFS paramters. The refined AFAC value was 0.68 and was taken from the V_2O_5 model.

Sample	Shell	N	R/Å	2σ/Å^{2a}	Ef	R/%
as synth. VAPO-5\ 10(IV)	V-O	2(2)	1.66(2)	0.0003	-0(2)	46.90
	VO	2.5(4)	2.01(2)	0.0003		
	V$\cdots$T[b]	0.54(5)	2.70(8)	0.0003		
calcined VAPO-5\ 10(IV)	V-O	3.2(4)	1.644(1)	0.0003	3(2)	54.16
	V$\cdots$O	2.1(6)	1.87(2)	0.0003		
	V$\cdots$T[b]	0.8(7)	2.45(2)	0.0003		

[a] The Debye-Waller was not refined as with the other VAPO-5 samples.
[b] T is either phosphorous or aluminium. EXAFS cannot easily distinguish between the two atoms

The k^3-weighted and least squares fitted EXAFS spectra of VAPO-5\10(IV) are shown in figure 3.18. It is hard to distinguish aluminium and phosphorous with EXAFS. Therefore with this sample, the results became the same wether the third shell was aluminium or phosphorous. The as synthesised sample resembles the calcined sample . The loss of a shell upon calcination are not observed here as it is with VAPO-5\8(IV). As table 3.8 show, the

mulitplicities are different after calcination. To see the effect of the AFAC of the multiplicity, the AFAC was set as 1, and refining the parameters except for the Debye-Waller. The results showed that the mulitplicity became 1.3(2) in the first shell. All of the mulitplicities in the subsequent shells were also smaller. Hence it is most likely the AFAC that have errors, even though the AFAC is taken from models with the same oxidation state. To investigate the value of the AFAC, the mulitplicity for the first shell of the as synthesised sample, was set to 1, and the AFAC and Debye-Waller factor were refined. The refined results showed a AFAC at 1.66(3), and the Debye-Waller factors had good values, and were not negative. These results show that the AFAC transferred from the reference models should not be employed to the vanadium samples, as they give errors to the multiplicity and Debye-Waller.

Calcined VAPSO-5\4(IV)

Table 3.9 show the parameters of the least square EXAFS analysis og VAPSO-5\4(IV).

Table 3.9: The refined EXAFS parameters of VAPSO-5\4(IV). The AFAC 0.62 was used after the model compound V_2O_5.

Sample	Shell	N	R/Å	$24\sigma/Å^2$	Ef	R/%
VAPSO-5\4(IV)	V-O	0.34(4)	1.644(1)	0.0003	-1(2)	44.94
	V-O	0.45(8)	1.87(2)	0.0003		

The EXAFS refinements show that vanadium has two oxygen shells with very small multiplicity. This can be seen in context by the fact that the Debye-Waller is set at 0.0003Å^2, which is taken up by the multiplicity. This is the only vanadium sample that contain only two shells. This could be a consequence of the Debye-Waller factor, or the noise. However it could also be a factor that the silicon make the vanadium bond differently to the framework.

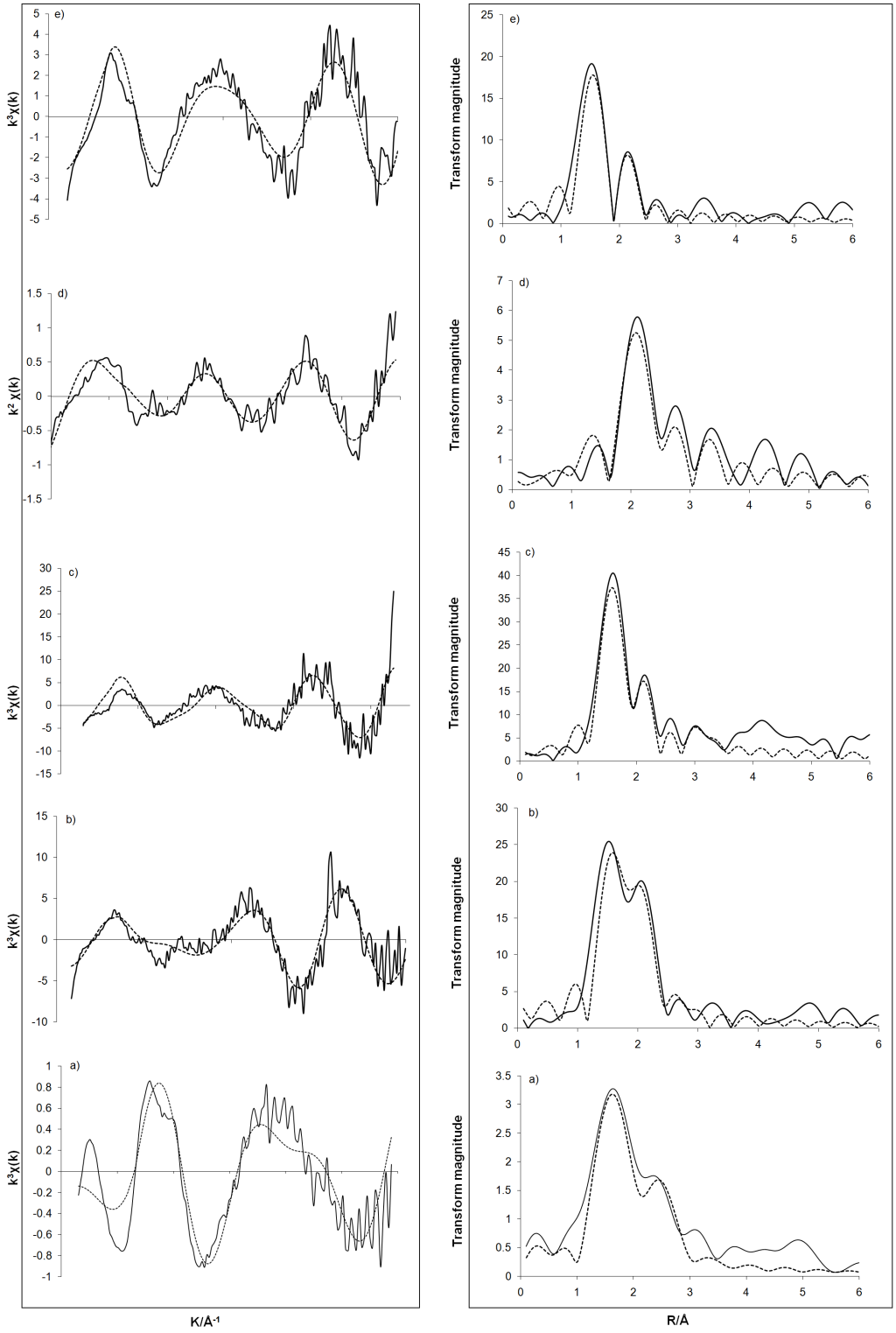

Figure 3.18: Experimental (-) and theoretical (⋯) k^2 and k^3-weighted EXAFS and its Fourier Transform for the different VAPO-5 and VAPSO-5 samples; a)calcined VAPSO-5\4(IV) k=2-8, b) as synthesised VAPO-5\10(IV) k=2-10, c) calcined VAPO-5\10(IV) k= 2-10, d) as synthesised VAPO-5\8(IV) k=2-8, e) calcined VAPO-5\8(IV)k=2-10.

3.3.3 How the synthesis conditions affect the bonding arrangement in VAPO-5

Figure 3.19 show that the VAPO-5 samples are quite different from the pentavalent V_2O_5 model. This shows that vanadium is not present as an oxide on the surface, but incorporated into the lattice. There is also a difference in the Fourier transform of the calcined VAPO-5\8(IV) and the as synthesised, which is a further indication that the bonding arrangement changes upon calcination. Another interesting factor is that the Fourier transform of VAPO-5\8(IV) and VAPO-5\10(IV) is a bit different. This can be explained by the use of different templates. As mentioned in section 1.6.1 there are different models suggested for how the vanadium species are bonded in the framework of AlPO-5, these differences could be as shown here, a consequence of different synthesis conditions.

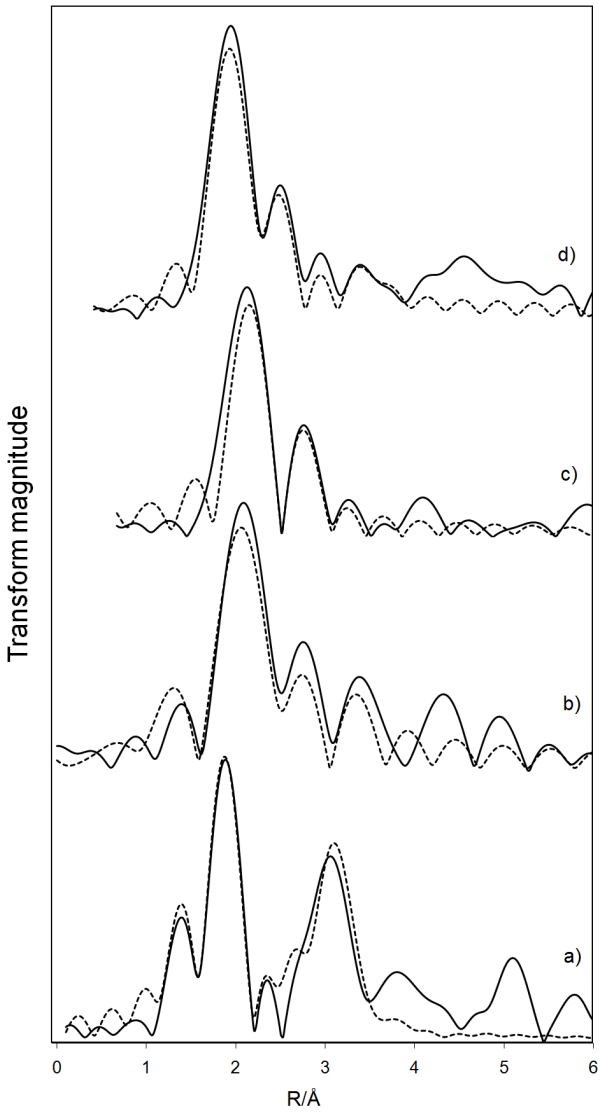

Figure 3.19: The Fourier transform of; a) bulk V_2O_5, b) as synthesised VAPO-5\8(IV), c) calcined VAPO-5\8(IV), d) calcined VAPO-5\10(IV)

The vanadium species in VAPO-5

There is a disagreement with several articles about which atom vanadium is bonded to when incorporated into the AFI structure. Montes *et al* and Jhung *et al* claimed that vanadium substitutes phosphorous, P(V), and Rigutto *et al* and Bekkum *et al* proposed that Al(III) is substituted for V(IV)[55]. Yu *et al* proposed a different theory as described in Section 1.6.1 that VAPO-5 existed as polymerised vandate, and was not incorporated into the framework of AlPO-5. EXAFS have been used to give an account for which proposed model would be the most probable.

By Fourier filtering the Fourier transform of the EXAFS in EXCURVE, it is possible to analyse selected peaks. As the first peak in the Fourier transform is the vanadium oxygen bond,it is interesting to look at the third shell to see if this is vanadium, phosphorous or aluminium. A way to selectively analyse the backscattering is to compare the experimental χ-curve and the theoretical curves for the various atoms. Fourier filtering has the ability to give a quick indication which atom is suitable for different shells. Unfortunately the parameters aquired from Fourier filtering are seldom applicable for the whole file.

Figure 3.20 shows the refined theoretical χ-curves and the experimental curve of calcined VAPO-5\10(IV).

Table 3.10: A table over the refined parameters for the theoretical atoms in figure 3.20 of the third peak in VAPO-5\10(IV) calcined

Atom	N	R/Å	2σ/Å^2	Ef	R/%
V$\cdots$P	1.41(8)	2.797(4)	0.012(1)	13.1(6)	12.06
V$\cdots$Al	1.4(1)	2.829(5)	0.008(2)	17.1(7)	17.48
V$\cdots$O	2.4(2)	2.908(7)	0.005(2)	26.2(8)	20.83
V$\cdots$V	1(1)	2.689(9)	0.016(2)		21.35

As both figure 3.20 and table 3.10, the neighbours that are mostly similar to the experimantal VAPO-5\10(IV) χ-plot is either phosphorous or aluminium. It is difficult do dinstinguish the two χ-curves of aluminium and phosphorous,

which is also shown in the table as their mulitplicity is similar. Although the R-factor of phosphorous is pronounced lower than the one for aluminum. Thus is can be concluded that in the third shell phosphorous is present.

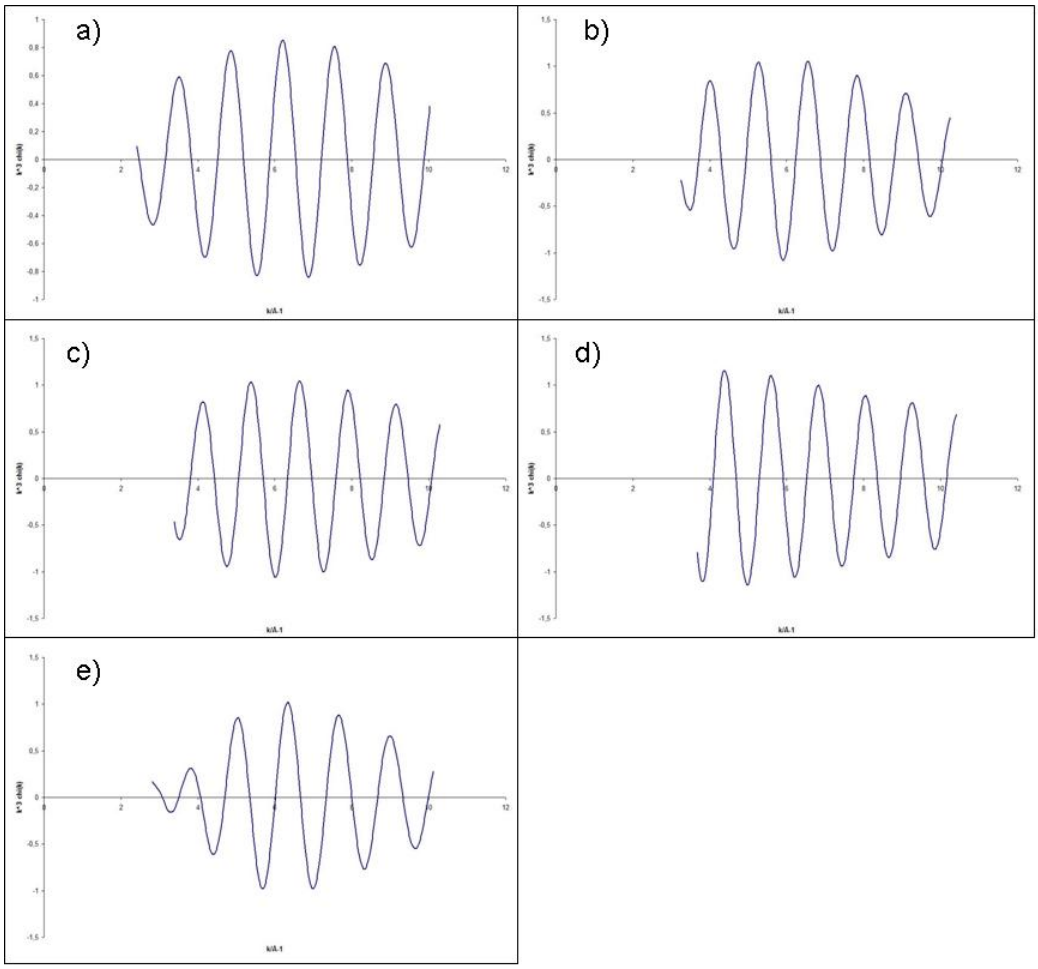

Figure 3.20: The figure shows the refined data for the Fourier filtered third peak of the calcined VAPO-5\10(IV). ΔR is 2.1-2.6. The refined parameters are shown in table 3.10 below. a) is the experimental curve of VAPO-5, b) is phosphorous, c) is aluminium, d) is oxygen, and e) is vanadium

The as synthesised VAPO-5\10(IV) was also investigated with Fourier filtering of the third peak. The Fourier filtering is shown in figure 3.21. Table 3.11 show the refined parameters of the Fourier filtering.

Table 3.11: A table of the refined parameters for the third peak in the as synthesised VAPO-5\10(IV). The Debye-Waller factor was not refined for oxygen, phosphorous and aluminium as it always became negative.

Atom	N	R/Å	2σ/Å^2	Ef	R/%
V$\cdots$P	0.33(4)	2.710(9)	0.002	-17.9(2)	49.58
V$\cdots$Al	0.49(4)	2.704(6)	0.002	-7.4(9)	33.5
V$\cdots$O	0.40(3)	2.482(8)	0.002	-20.9(4)	41.84
V$\cdots$V	0.36(2)	2.505(4)	0.013(2)	-10.6(8)	49.37

For Fourier filtering the R-factors are quite high, this could be assigned to the noisy data of the as synthesised sample. From the table it seems as the aluminium is in the third shell of the as synthesised VAPO-5\10(IV) however this might not be applicable due to the high R-factors.

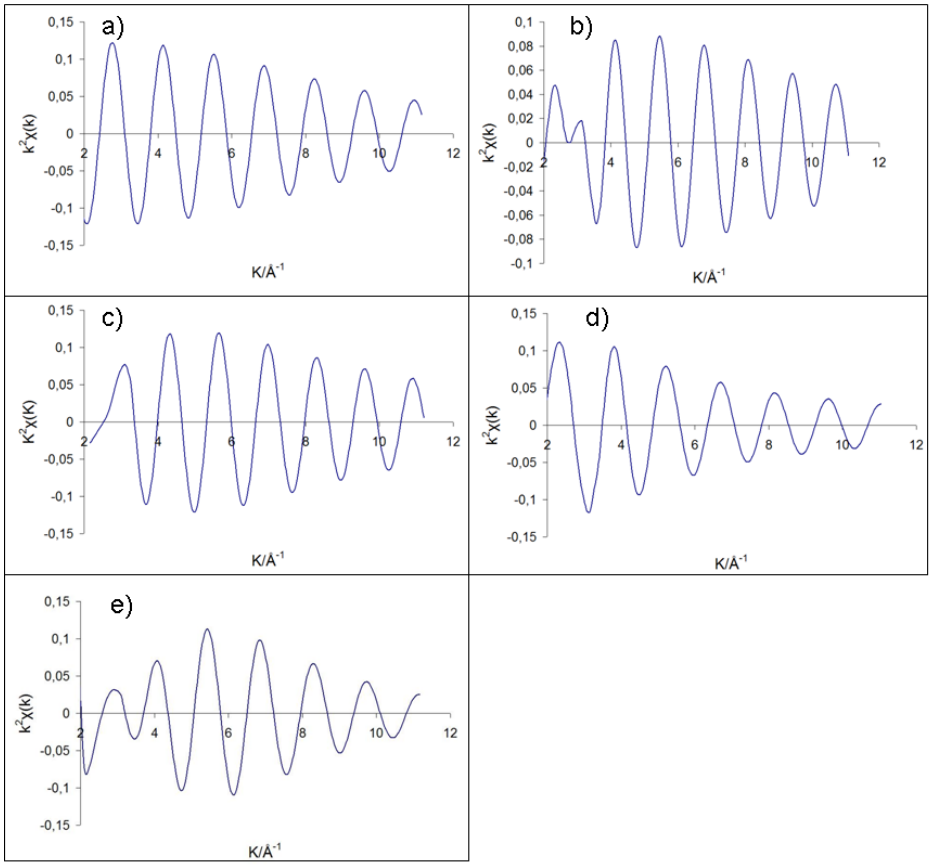

Figure 3.21: The figure shows the refined data for the Fourier filtrated third peak of the as synthesised VAPO-5\10(IV),ΔR is 2.1-2.6 .The refined paramters are shown in table 3.11 . a) is the experimental curve of VAPO-5 as synthesised, b) is phosphorous, c) is aluminium, d) is oxygen and e) is vanadium

The fourth peak of the as synthesised VAPO-5\8(IV) was Fourier filtered to distinguish which atom that are present i the fourth shell. Results from the Fourier filtered peak are shown in figure 3.22.

Table 3.12: The refined paramters for the Fourier filtered fourth peak.

Atom	N	R/Å	2σ/Å^2	Ef	R/%
V$\cdots$P	1.1(6)	3.283(8)	0.0003	-19.3(5)	32.88
V$\cdots$Al	1.28(6)	3.341(7)	0.0003	-17.9(4)	26.62
V$\cdots$O	1.4(2)	3.42(2)	0.0003	-9.3(7)	58.66
V$\cdots$V	0.64(3)	3.09(1)	0.0003	-18.9(5)	52.23

Fourier Filtering show that aluminium give the lowest R-factor, which suggests that aluminium is in the fourth shell. As the data are quite noisy it is difficult to distinguish peaks from noise. This is seen as the experimental curve does not resemble the refined curve of aluminium.

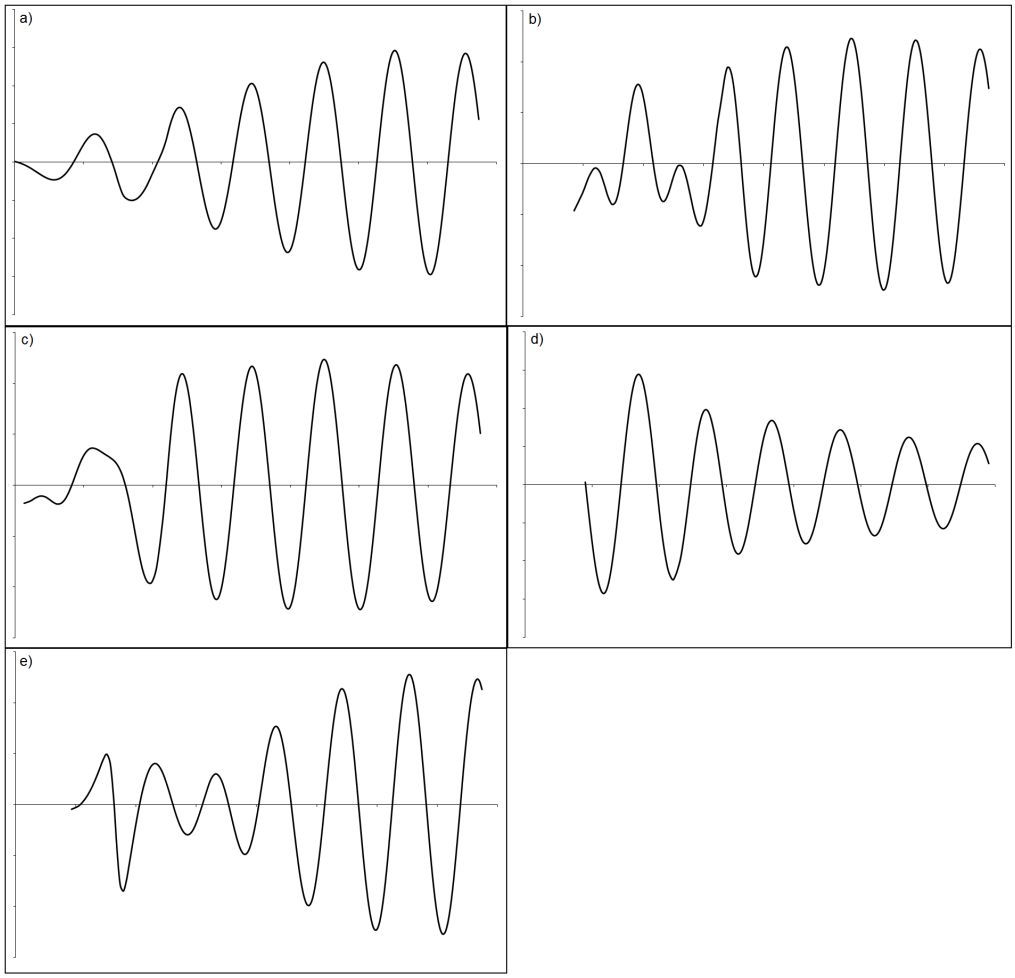

Figure 3.22: The figure shows the refined data for the Fourier filtered fourth peak with ΔR 2.8-3.6, of the as synthesised VAPO-5\8(IV). The refined parameters are shown in table 3.12; a) is the experimental curve, b) is phosphorous, c) is aluminium, d) is oxygen and e) is vanadium.

Figure 3.23 show the Fourier filtered third peak in the calcined VAPO-5\8(IV). Table 3.13 show the refined EXAFS for the Fourier filtered peak.

Table 3.13: The refined paramters for the Fourier filtered third peak of the calcined VAPO-5\8(IV)

Atom	N	R/Å	2σ/Å^2	Ef	R/%
V..P	0.33(2)	3.05(1)	0.0003	5(1)	31.18
V..Al	0.23(1)	2.79(4)	0.0003	-17.5(6)	27.30
V..O	0.45(2)	2.875(6)	0.0003	-5.4(5)	21.06
V..V	0.19(2)	2.91(2)	0.0003	-0(2)	48.18

In the Fourier Filtered third peak it is oxygen which resembles the experimental curve, which is also evident in table 3.7. In the table the R-factor of the oxygen shell is lowest,hence it is oxygen in the third shell. These results show that upon calcination the aluminium in VAPO-5\8(IV), have slighty different distances, hence lower intensity as mentioned above. Which mean, as already shown in the XANES for VAPO-5\1(V) (referring to section 3.2.1), that vandium is rearranged upon calcination.

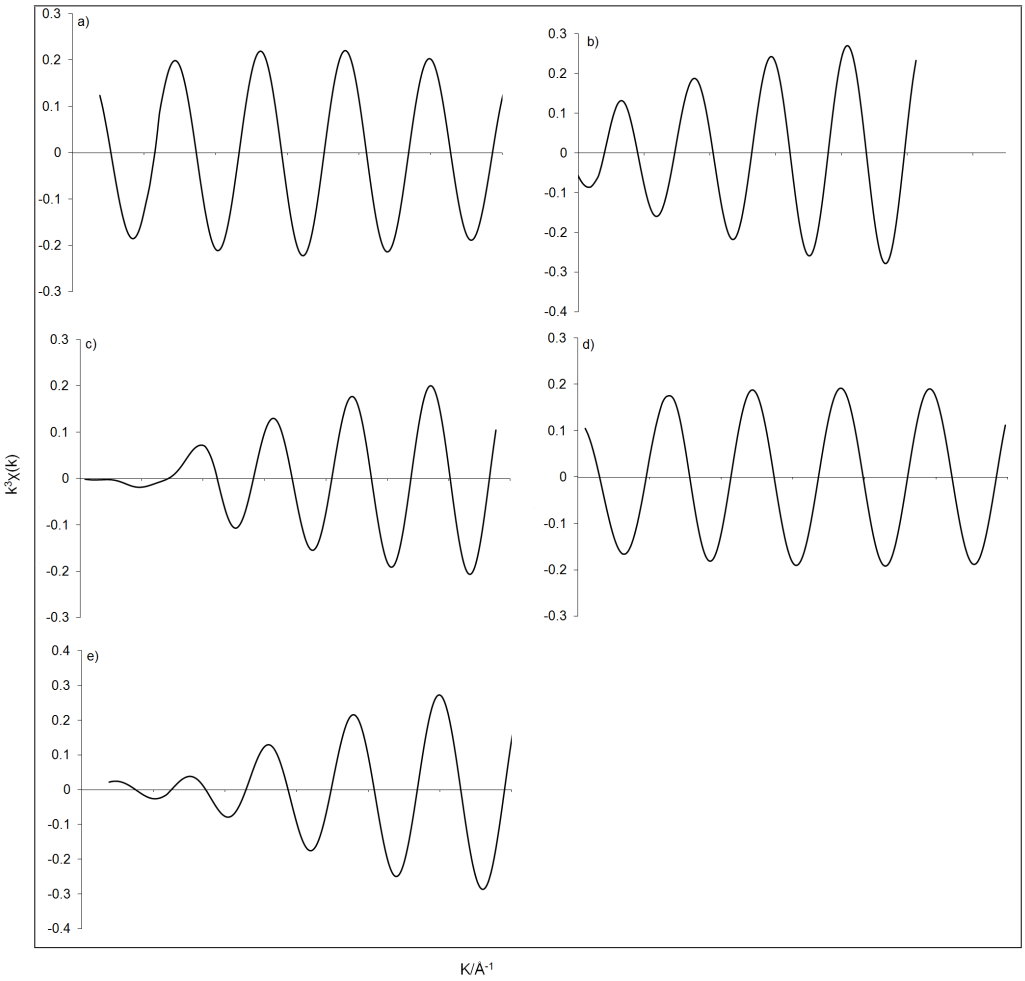

Figure 3.23: The figure shows the refined data for the Fourier filtered third peak (2.4-2.9) of the calcined VAPO-5\8(IV) whereas the refined paramters are in table 3.13; a) is the experimental curve, b) phosphorous, c) aluminium, d) oxygen and e) vanadium.

As a summary it is observed that VAPO-5\10(IV) has phosphorous in the third shell, even though table 3.11 show otherwise. These values are most likely influences by noise in the EXAFS since the R-factors in the Fourier filtering should not be that high. It is thereby concluded substitutes aluminium. The model suggested by Rigutto *et al* is thereby the correct model for VAPO-5\10(IV). In figure 3.24 the propesed model is shown where vanadium substitutes aluminium. Thereby the vanadium specie have a square planar structure, and is five coordinated. The model proposed by Wei et al is also probable.

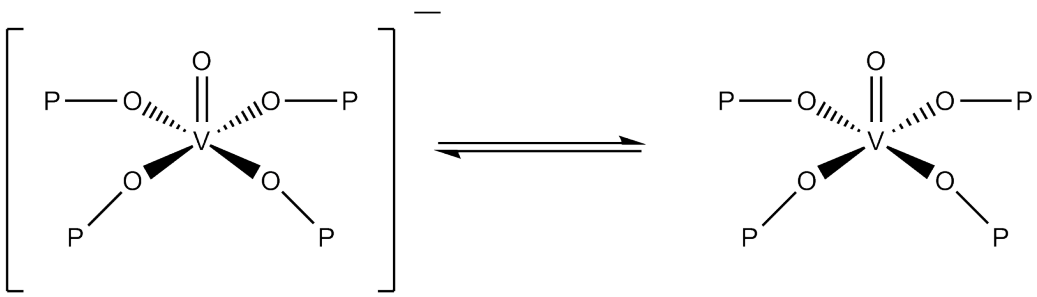

Figure 3.24: The model proposed by Rigutto *et al* could be employed on the VAPO-5\10(IV) sample as it substitutes phosphorous.

The as synthesised sample of VAPO-5\8(IV) show from the EXAFS refinements aluminium in the fourth shell. However the model suggested by Montes *et al*, cannot be correct. As already shown from the EXAFS refinements, the bond distance of the first shell is so short and is most likely the vanadyl group. According to the model, the vanadyl group is broken upon calcination, and the bond distance have not been longer after the calcination. XANES analysis also shows that the model of Montes *et al* cannot be right. As mentioned in Section 1.9.1 the pre-edge of V_2O_5 is due to the vanadyl group. It is observed in the XANES of VAPO-5\8(IV) that the pre-edge intensity increases upon calcination. If the model of Montes *et al* was correct, the pre-edge intensity should decrease. Hence the model of Montes *et al* and Yu *et al* is ruled out. The model proposed by Wei *et al* correlates well with what is shown in the EXAFS refinements according to the multiplicty and bond distances. It is shown in table 3.7 vanadium is four coordinated after it is calcined, which is correlated with the calcined sample of figure 3.25. As the table shows the multiplicity is increased in the first shell upon calcination, thereby it is logical that vanadium might posess two double bonds. Prior to the calcination the Wei *et al* suggests that vanadium is five coordinated. The as synthesised VAPO-5\8(IV) also show a five coordination. This is also observed in the XANES of the as synthesised and calcined VAPO-5\8(IV). As the pre-edge is dependent upon the coordination number, when the coordination number is lowered the pre-edge intensity increases. Which is evident in the XANES for VAPO-5\8(IV). Hence it follows the illustration suggested by Wei *et al*. Thereby it is concluded that vanadium in the VAPO-5 samples are either square planar as in figure 3.24 or dirstorted tetrahedra as in figure 3.25.

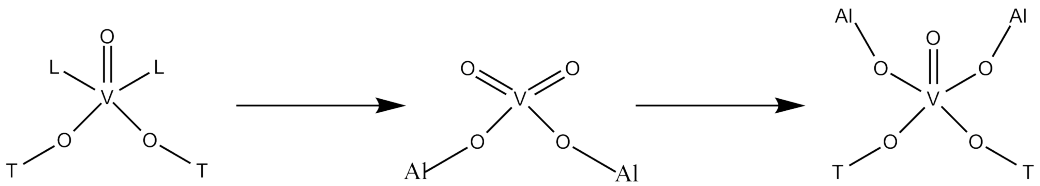

Figure 3.25: Illustration of the vanadium specie in VAPO-5\8(IV)

3.4 *In situ* studies on the redox properties of: VAPO-5,VAPSO-5 and ion exchanged zeolites

In order to study the possible redox mechanism that is proposed for reduction of NOx with hydrocarbons, *in situ* XANES was conducted. Interesting samples were selected for further investigation after the EXAFS refinements. The *in situ* measurement was done by using the *in situ* cell and experimental setup, illustrated in figure 2.3 and in figure 2.2 . Figure 3.26 show the XANES and the pre-edge area for VAPO-5\8(IV) with the prop/O_2 flow, and an *in situ* study with hydrogen (H_2) flow. As figure 3.26 show, there are no changes in the XANES with prop/O_2 flow. Table 3.14 show the pre-edge fit of the VAPO-5\8(IV) in prop/O_2, and in H_2. Since there were no visible changes in the XANES for VAPO-\8(IV), during the in *in situ* experiment in prop/O_2. It was concluded that the vanadium was not reduced by propene. Therefore there were no further heating of the sample in prop/O_2. Several articles have reported that VAPO-5 are reduced in the presence of hydrogen.[27,34] Thus this was investigated with *in situ* XANES. As figure 3.26 show, the XANES for vandium in H_2 did not show any distinct changes either. Although the bar chart show changes in the pre-edge area, this is not a true observation. Table 3.14 show the refined pre-edge fit for VAPO-5\8(IV) in hydrogen. The pre-edge areas show small changes, and the change that are evident can be assigned to the uncertainty they hold. Therefore a bar chart is not always the best way to show the pre-edge area, as it is very sensitive to small changes.

Figure 3.27 show the pre-edge position vs the pre-edge area for the calcined VAPO-5\8(IV) compared to the different models for vanadium. The pre-edge position for the sample in room temperature is shifted towards lower energies, than for the other reaction stages. The pre-edge position for the other reaction stages has approximately the same pre-edge position as for tetravalent vanadium models. Although as shown previously, these models are not ideal for the VAPO-5 and VAPSO-5 samples.

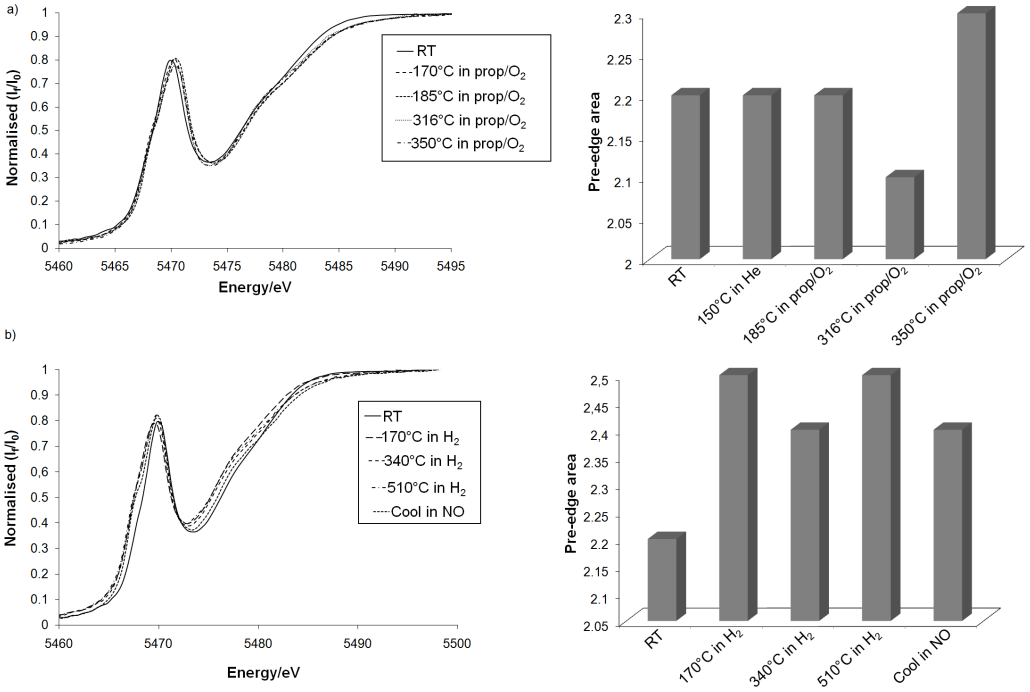

Figure 3.26: The XANES in situ study on the calcined VAPO-5\8(IV) with a) heating in propene and oxygen, b) heating in hydrogen

Figure 3.28 show that in the normalised XANES of VAPSO-5\4(IV), the sample in room temperature is shifted towards higher energies and the pre-edge area is lower than in the other reaction stages. The reaction stages from 170°C in prop/O_2 and to the cooling in NO show an increase in the pre-edge area. At the same time the K-edge position is shifted towards higher energies. The difference in the pre-edge position and the pre-edge area from the VAPSO-\4(IV) in room temperature and the other reaction stages, could be assigned to the heating in the reaction gases causes a chemical shift due to a change in the coordination number. As mentioned under section 1.9.1, the intensity of the pre-edge is increased when the coordination number is lowered. The effect of the oxidation state, does not apply here, as the pre-edge would decrease if vanadium was exposed to a reduction agent. However in this case the pre-edge continues to increase in the presence of propene and continues to increase, when the gases was switched to NO. As the coordination number changes, the local geometry might also change.

Table 3.14: The refined fit of the pre-edge area and position for the calcined VAPO-\8(IV)

Sample		Pre-edge			K-edge
	Reaction stage	Pre-edge centroid	Area	R-factor	
VAPO-5\8(IV)	RT	5468.8(2)	2.2(2	0.00077	5476.08
	150°C in Helium	5469.9(2)	2.2(2)	0.00112	5476.36
	185°C in prop/O_2	5470.0(2)	2.2(2)	0.00126	5476.42
	316°C in prop/O_2	5469.9(2)	2.1(2)	0.00115	5476.32
	350°C in prop/O_2	5470(0)	2.3(2)	0.00178	5476.34
VAPO-5\8(IV)	150°C in He	5469.6(2)	1.03(6)	0.00250	5481.39
	170°C in H_2	5469.2(2)	2.5(2)	0.00115	5474.99
	340°C in H_2	5469.3(2)	2,4(2)	0.00144	5475.42
	510°C in H_2	5469.3(2)	2.5(2)	0.00158	5475.18
	Cool in NO	5469.5(2)	2.4(3)	0.00183	5475.92

Position of the K-edge increases also to higher energies. Thus it is concluded that the VAPSO-5\4(IV) experiences a change in the chemical environment due to a change in the coordination number. This appears in the XANES during the *in situ* measurement.

Figure 3.29 verifies what is found in the in situ study of VAPO-5\8(IV) and VAPSO-5\4(IV). The figure show that some water is released before 100°C in the VAPO-5\8(IV), and at 100°C in the VAPSO-5\4(IV). However it show that hydrogen is not released or absorbed by either of the samples. This result conclude that VAPO-5 and VAPSO-5 is not reduced by hydrogen, although several articles has reported otherwise.[27]

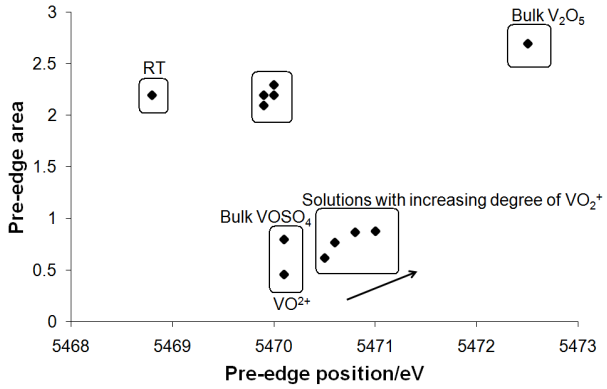

Figure 3.27: The pre-edge position vs the pre-edge area of VAPO-5\8(IV) in propene and oxygen

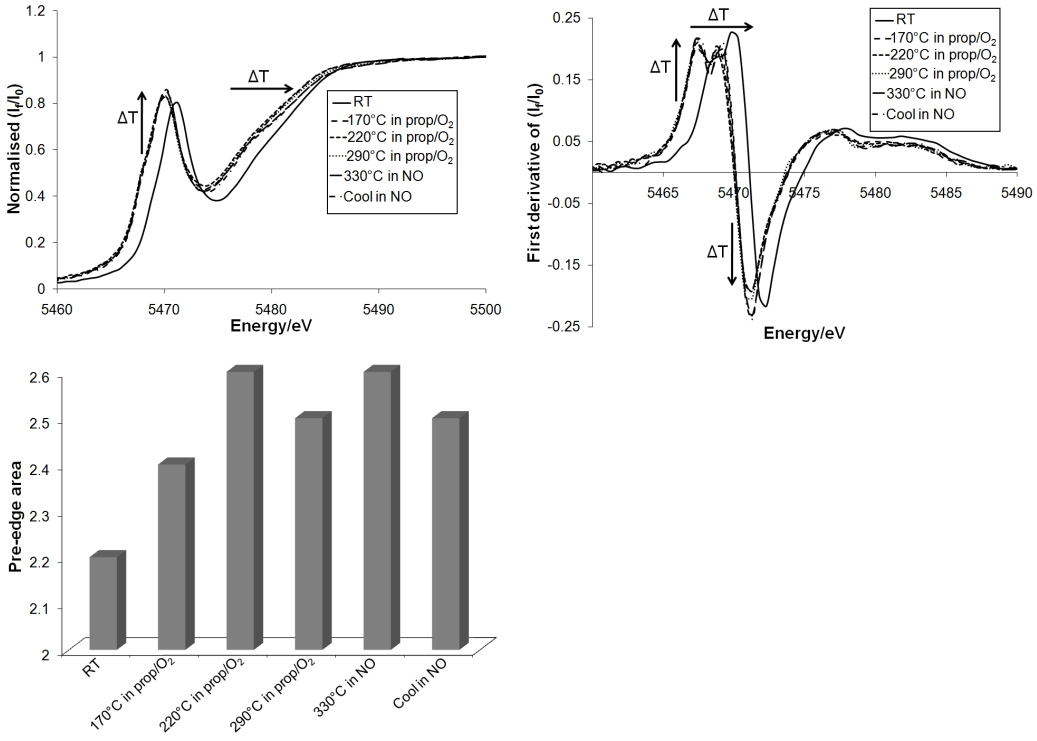

Figure 3.28: The normalised XANES and the first derivative of the VAPSO-5\4(IV).

The *in situ* study of VAPO-5\10(IV) is shown in figure 3.30. As the figure show the pre-edge intensity of VAPO-5\10(IV) at 150°C in prop/O_2 is lower than for room temperature. When the sample is further heated in prop/O_2 the pre-edge intensity increases. It decreases from 240°C to 320°C. It seems

Table 3.15: The refined pre-edge area at the different reaction stages for the calcined VAPSO-5\4(IV).

Sample		Pre-edge			K-edge
	Reaction stage	Pre-edge centroid	Area	R-factor	
VAPSO-5\4(IV)	RT	5471.0(2)	2.2(2)	0.00144	5477.4
	170°C in prop/O_2	5469.9(2)	2.4(2)	0.00099	5475.6
	220°C in prop/O_2	5469.8(2)	2.6(2)	0.00091	5476
	290°C in prop/O_2	5469.8(2)	2.5(2)	0.00097	5475.1
	330°C in NO	5469.9(2)	2.6(2)	0.00118	5475.6
	Cool in NO	5469.9(2)	2.5(2)	0.00128	5476.2

as the pre-edge intensity decreases and increases when the temperature is increased in the presence of prop/O_2. Which suggests it follows the same reaction mechanism proposed in section 1.3.3. Thus vanadium is reduced by propene and the reoxidised by oxygen. There are no shift in the pre-edge position which indicates thatnvanadium is only partially reduced from pentavalent vanadium to tetravalent vanadium,until it is reoxidised. It is reported that vandium is only partially reduced when it is incorporated into the lattice.[27]

As a comparison to the the behaviour of vanadium that is incorporated in the synthesis of VAPO-5 and VAPSO-5, an *in situ* study was done on ion exchanged ZSM-5 (V:ZSM-5). As previously mentioned in section 1.4.2, when the metal is ion exchanged it is at the surface of the zeolite, and thereby exhibit other properties. This was interesting in the comparison of VAPO-/VAPSO-5 with V:ZSM-5. Since the VAPO-5 and VAPSO-5 did not give an obvious reduction in the presence of prop/O_2, it could be because the vanadium was incorporated into the framework of VAPO-5 and VAPSO-5. Figure 3.31 show the in situ study on V:ZSM-5 ion exchanged with 0.1M

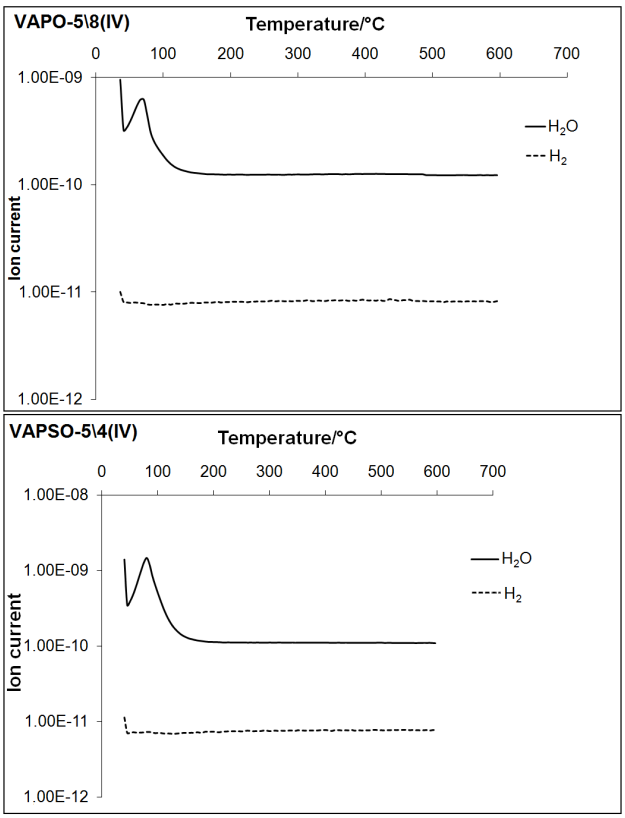

Figure 3.29: The temperature programmed reduction of VAPO-5\8(IV) and VAPSO-5\4(IV)

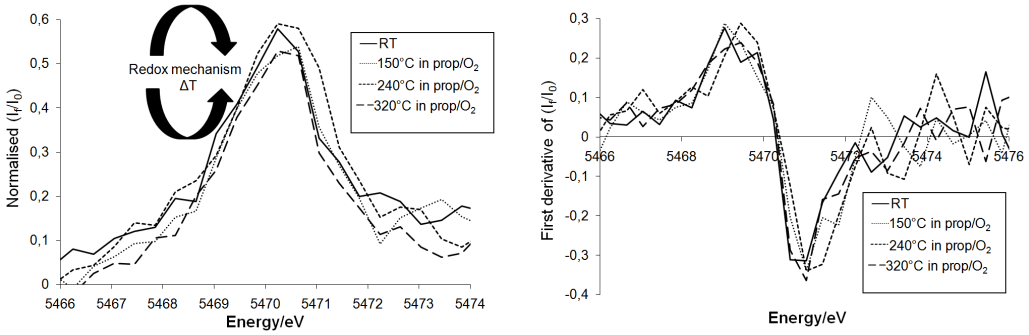

Figure 3.30: The Normalised pre-edge and the derivative of the calcined VAPO-5\10(IV) in the different reaction stages.

$VOSO_4$ in an autoclave. This sample was chosen because it had an increased vanadium content, which gave a larger signal in the XANES. As figure 3.31 show, the room temperature V:ZSM-5 is shifted towards higher energies.

The intensity of the pre-edge is slightly lower than for the one in 200°C in prop/O_2. The highest pre-edge is that of 200°C in prop/O_2 and it decreases subsequently with the reaction stage. The decrease in the pre-edge intensity could be due to:

- Vanadium is reduced
- The coordination number increases
- Vanadium is rearranged and changes its geometry, thereby decreases the 3d-4p mixing.
- The effect of the ligand, due to ligand exchange

In table 3.16 the refined pre-edge fit is shown.

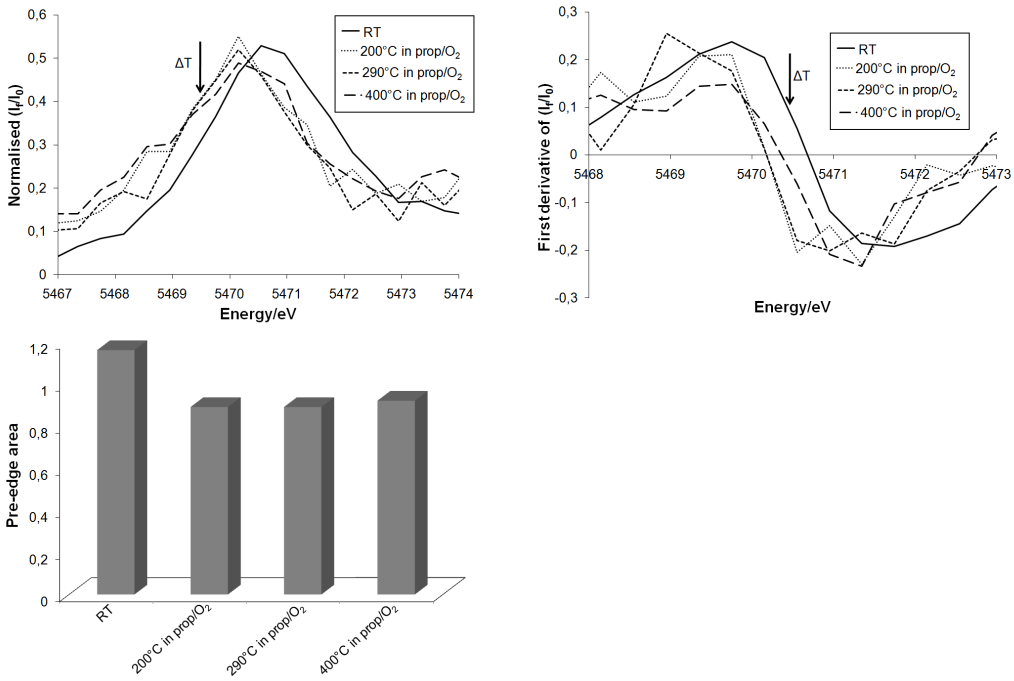

Figure 3.31: The normalised pre-edge and the first derivative of the pre-edge, in the *in situ* study of V:ZSM-5

Figure 3.31 also show the pre-edge fit of the V:ZSM-5. This pre-edge refinement is not quite representable as a result, as the figure show, the pre-edge

Table 3.16: The refined fit of the pre-edge area and position for the V:ZSM-5

Sample	Reaction stage	Pre-edge centroid	Area	R-factor
V:ZSM-5	RT	5470.7(2)	1.16(7)	0.00198
	200°C in prop/O_2	5470.1(3)	0.89(9)	0.00414
	290°C in prop/O_2	5470.1(3)	0.89(8)	0.00256
	400°C in prop/O_2	5470.0(3)	0.92	0.00219

shape is not uniform due to the data collection at SNBL. Hence the pre-edge area in the table is not consistent with the qualitative study of the normalised pre-edge intensity. According to what have been observed for the vanadium in solution (referring to Section 3.2.2), when the pre-edge position is equal for the vanadium samples, it is the oxidation state that dominates the pre-edge intensity. Hence it is concluded that vanadium is reduced in prop/O_2.

The results from the in situ experiments of VAPO-5, VAPSO-5 and V:ZSM-5, show how the vanadium is bonded to the surface affect its properties. As VAPO-5\8(IV) show no distinct changes neither in prop/O_2 or H_2, it indicates that vanadium is incorporated into the framework of AlPO-5. Also in the VAPSO-5\4(IV) where the oxidation state is not influenced, only the coordination number or the geometry. VAPO-5\10(IV) showed however a redox cycle in the presence of propene. The different behaviuors of vanadium in the VAPO-5 can also be seen in context with what is found from the EXAFS results (Section 3.3.3). Where the calcined VAPO-5\8(IV) and calcined VAPO-5\ show different atoms in the third shell. This can account for their different behavious in the presence of prop/O_2.

3.5 Activity measurements for the selective catalytic reduction of NOx

The activity for the selective reduction of NOx was done at the University of Newcastle as described in section 2.5. The VAPO-5\10(IV) was chosen because as shown in the in situ experiment in section 3.4, it showed a redox cycle in the presence of prop/O_2. Unfortunately it was not investigated in the presence of NOx, as during the in situ experiment it was believed that vanadium was not reduced. The data was very noisy and therefore, the small changes that happened, was not easily to observe. The VAPSO-5\4(IV) was chosen because of the changes seen in the *in situ* measurement. Although vanadium was not reduced, the coordination number was altered in the presence of propene and NO, thereby it might reduce NO.

Figure 3.32 show the conversion of NOx with a VAPO-5, VAPSO-5 and AlPO-5 mixed with 5wt%V_2O_5. The AlPO-5 mixed with V_2O_5 was done to compare the difference with the synthesised samples. Since it is already acknowledged that V_2O_5 is a catalyst for the reduction of NOx, using ammonia as the reducing agent.[2] As the figure show the AlPO-5 mixed with 5wt% V_2O_5 showed the highest activity of 3.2%. VAPO-5\10(IV) showed the lowest activity with an activity of 1.58%. Empty reactor was tested to see the contribution, since the reactor walls might have pollutants, which contributes to the activity. As seen the empty reactor has an activity ranging from 1-0 as the temperature was raised. Therefore the conversion of NOx over VAPO-5\10(IV) can be said to be zero. The low activities in the converison of NOx can be accounted for by the observations of the *in situ* measurements. As seen in figure 3.30 VAPO-5\10(IV) participates in a redox cycle with propene and oxygen. Which means that when the NO is flowed over the sample, vanadium might be in an oxidised state. Hence it will not participate in a redox reaction with NO. As for VAPSO-5\4(IV) the reduction of vanadium was not observed as seen in figure 3.28. On the other hand it changes its coordination number, and it did show some conversion,

eventhough this was very small.

It should have been done FT-IR on these samples, to study if they have acid sites, and thereby be desirable in acid catalysis. Unfortunately the time limit resulted in other priorities. The ion exchanged V:ZSM-5, which is shown in figure 3.31, showed reducibility in prop/O_2, without being reoxidised. Therefore it should have been done activity measurents on this sample, but because of technical difficulties, therefore was not done. It is thereby concluded that VAPO-5 and VAPSO-5 is not desireable for the reduction of NOx with propene as the reduction agent.

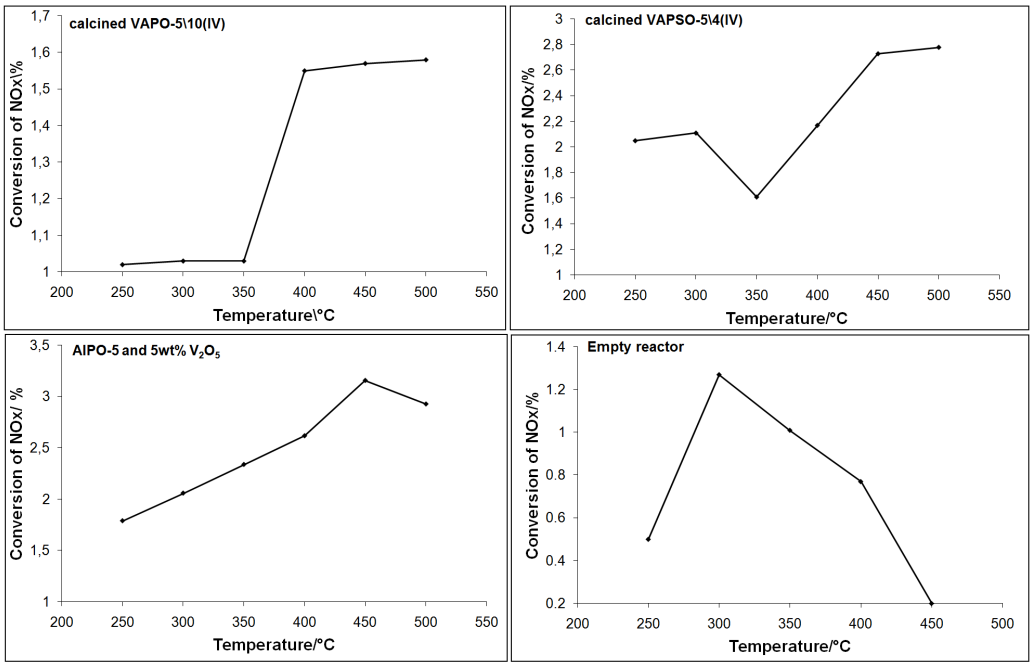

Figure 3.32: The conversion of NOx over VAPO-5\10(IV) and VAPSO-5\4(IV)

Chapter 4

Concluding remarks: Synthesis and characterisation of VAPO-5 and VAPSO-5

- Increased vanadia loading leads to a decrease in the surface area
- Tripropylamine gave the highest vanadium content, and had a shorter crystallisation time than TEA and DCHA. Hence this is the best template.
- As seen in the EXAFS and XANES the calcined VAPO-5\8(IV) show a distorted tetrahedra geometry;Whereas VAPO-5\10(IV) showed a square pyramidal geometry. Thereby they behave differently when exposed to the gas mixtures.
- The model proposed by Montes *et al* and Wei *et al* have been verified by EXAFS and XANES. The model proposed by Rigutto *et al* and Yu *et al* was ruled out, as they are contradicting with the EXAFS and XANES analysis.
- Vanadium is incorporated into the framework of AlPO-5 and is not reduced in the presence of hydrogen, although it has been reported otherwise.[33,27]
- Activity measurement showed no remarkable conversion of NOx over VAPO-5 and VAPSO-5, which is also seen in the *in situ* experiment. Hence the VAPO-5 and VAPSO-5 samples are not suitable catalysts for the reduction of NOx with hydrocarbons as the reducing agent.

Chapter 5

Experimental: Precipitation of V_2O_5 in zeolites H-ZSM-5 and H-Y

5.1 Precipitation of V_2O_5 particles in H-ZSM-5 and H-Y

The method of depositing V_2O_5 particles on H-ZSM-5 and H-Y was a combination of what has been done in the articles: Selective Catalytic Reduction of NO by NH_3 Over Vanadium Containing Zeolites[58] and Characterisation of zinck oxide nanoparticles encapsulated into zeolite-Y. An in situ combined X-ray diffraction.[59]. Table 5.1 show the different zeolites which were changed with the different parameters.

The procedure was as follows. H-ZSM-4 and H-Y was weighed (Zeolyst International, 4g), the solution of 0.05M V_2O_5 and 0.1M $VOSO_4$ (120ml) was added to each of the zeolites. and the mixture stirred for 24h. In order to increase the pH, different bases and acids were used as shown in table 5.1 For some of the mixtures the ion exchange was done twice to increase the vanadium content[60]

Table 5.1: Ion exchange of H-ZSM-5 and H-Y with different vanadium solutions and with different pH.

Zeolite	V-Source	pH	Base/Acid	Comments
H-Y(30)	0.1M $VOSO_4$	2.2	H_2SO_4	Onefold ion exchange
H-Y(30)	0.1M $VOSO_4$	5	1M NaOH	Onefold ionen exchange
H-Y(30)	0.05M V_2O_5	0.5	1M H_2SO_4	Onefold ion exchange
H-Y(30)	0,05M V_2O_5	2	1M NaOH	Onefold ion exchange
ZSM-5(80)	0.05M V_2O_5	0	1M H_2SO_4	Twofold ion exchange
ZSM-5(80)	0.1M $VOSO_4$	0.8	1M H_2SO_4	Twofold ion exchange
ZSM-5(30)[a]	0.05M V_2O_5	9	5M NH_3	Twofold ion exchange
ZSM-5(30)	0.1M $VOSO_4$	2.5, 3.5, 9.3,6.3	5M NH_3	Twofold ion exchange
H-Y(80)[b]	0.1M $VOSO_4$	9.2	5M NH_3	Onefold ion exchange
H-Y(80)[b]	0.05M V_2O_5	9.7	5M NH_3	Onefold ion exchange
H-Y(30)[c]	0.1M $VOSO_4$	9.4	5M NH_3	Twofold ion exchange
H-Y(30)[c]	0.05M V_2O_5	9	5M NH_3	Twofold ion exchange

[a] This sample is characterised further and is called V_2O_5/ZSM-5
[b] The ion exchange was executed in autoclaves at 150°C
[c] The H-Y(30) was ion exchanged first for 24h two times, and then 5M NH_3 was added for 30min. H-Y which was ion exchnaged with $VOSO_4$ will be called V_2O_5/Y for further characterisation techniques.

5.1.1 XRD

XRD was done at the institute of Material Technology at NTNU in Trondheim. A Siemens D-5005 diffractometer operated at 50keV and 40mA with a constant slit opening and a dstep size of 0.02° converting eange of 10-60° 2Θ with a counting time 5seonds per step. The instrumental broadening is

0.090. These parameters was especially designed to detect nanoparticles.

5.1.2 TGA

The operational setup is as described in Section 2.4.5.

5.1.3 XAS

X-ray absorption data were collected in the fluorescence and transmission mode at the vanadium K-edge at the Swiss Norwegian Beamlines (SNBL, BM01b) using a 13 element Ge multi channel detector.The beamline is equipped with a Si-111 double crystal monochromator and chromium mirrors to reflect high intensity glitches. Data were collected in the multibunch filling mode providing a maximum current of 200 mA. The vanadium samples was filled in a sample holder with kapton windows. The EXAFS spectra were measured with 5 eV steps below the edge, 0.2 eV steps in the edge region, and steps equivalent to 0.03 $Å^{-}1$ increments above the edge (region borders were 5400, 5450, and 5500 eV). The scan ended at 6000eV. For EXAFS Several XAS scans were collected and summed. The XANES scan ended at 5500eV. All XANES spectra were energy corrected against a vanadium-foil calibration (5465 eV). In ion chamber I_0 it was 20%N_2 and 80%He in ion chamber I_1 and I_2 it was 90%He and 10%Ar.

In situ measurements

The same in situ cell and experimental setup that was used in section 2.4.4 was used in this experiment. Also the same paramter files were used as described in section 2.4.4.

Selective oxidation of propene

The samples were placed in an in situ cell developed for combined XAS and Raman data collection. The samples were heated to 250°C in 5% O_2/He with a totalt flow of 15mil/min, and then cooled to 150°C. The samples were then heated to 400°C in 0.25% C_3H_6 and 1.5% O_2, with a total flow of 15ml/min, while collecting XANES and Raman. A mica window of one side of the cell allows Raman data collection simultaneously at each temperature. The samples were then cooled and a Raman scan was collected at room temperature.

Raman

The employed Raman instrument was a dispersive spectrophotmeter Renishaw RA100, with a 514nm Ar-ion laser and a 1200 line mm^{-1} grating. A standard Raman RP20V prope was connected to the insturment by optical fibres. The focusing of the Raman laser on the sample was obtained using the video camera on the RP20V head with a final optmixation by cyclic fast aquisitions of the Raman spectrum. A Raman spectra was done at several temperatures, by doing several aquisitions which was summed to lower the fluorecence radiaton.

Mass spectrometer

The outlet of the in situ cell was connected to a mass spectrometer, Pfeiffer Vacuum OmniStar. The Pfeiffer Vacuum OmniStar gas analysis system is a high performance, flexible quadrupole mass spectrometer in a compact benchtop package. OmniStar is capable of simultaneously monitoring up to 64 gases from 100% to below 10ppb with available mass ranges of 1-100, 1-200 and 1-300 ammu. Dual filaments are standard with the OmniStar for maximum up-time as well as a secondary electron multiplier detector for fast, low level measurements. Pressure is constantly monitored via a Pfeiffer

Vacuum Full Range gauge and the filaments and detector are interlocked based on a used defined trip level. Integral bakeout and inlet heaters are included to reduce backgrounds and prevent condensation.

Chapter 6

Results and discussion: Precipitation of V_2O_5 particles on the zeolites H-ZSM-5 and H-Y

6.1 Precipitation of V_2O_5 particles in H-ZSM-5 and H-Y

As described in section 5.1 H-ZSM-5 and H-Y was ion exchanged and the pH was regulated to see the effect of the environment on the vanadium species. The results from the ion exchange is summed up in table 6.1 below. Table 6.1 clearly show that the oxidation state of vanadium is sensitive to changes in the pH. This can be seen in connection with the phase diagram for vanadium as shown in figure 1.18

It is escpecially the alkaline solutions that are interesting, as the pH is raised. In the beginning of the experiment the solutions were already acidic, hence the contribution of the sulphuric acid was minimal. When NaOH was used as a base to raise the pH, the color changed although the pH did not raise. To raise the pH to approximately 9, 5M NH_3 had to be used.

As seen in the table the H-ZSM-5 and H-Y with 0.1M $VOSO_4$ became black after the pH was 9. This is because the vanadium became reduced by the ammonia and formed $[V(H_2O)_6]^{3+}$[61] which is trivalent vanadium. The reducibility of vanadium is not that strong for pentavalent vanadium, when

Table 6.1: Ion exchange of H-ZSM-5 and H-Y with different vanadium solutions and with different pH.

Zeolite	V-Source	pH	Base/Acid	Color	wt% V
H-Y(30)	0.1M $VOSO_4$	2.2	H_2SO_4	Blue	
H-Y(30)	0.1M $VOSO_4$	5	1M NaOH	Green	
H-Y(30)	0.05M V_2O_5	0.5	1M H_2SO_4	Yellow	
H-Y(30)	0,05M V_2O_5	2	1M NaOH	Yellow	
ZSM-5(80)	0.05M V_2O_5	0	1M H_2SO_4	Yellow	
ZSM-5(80)	0.1M $VOSO_4$	0.8	1M H_2SO_4	Blue	
ZSM-5(30)	0.05M V_2O_5	9	5M NH_3	Bright yellow some orange precipitate	3.93
ZSM-5(30)	0.1M $VOSO_4$	2.5, 3.5, 9.3,6.3	5M NH_3	From green to blue-grey,brown and finally black, respectively to the pH	
H-Y(80)[a]	0.1M $VOSO_4$	9.2	5M NH_3	Green/brown	
H-Y(80)[a]	0.05M V_2O_5	9.7	5M NH_3	The solution was transparent	
H-Y(30)[b]	0.1M $VOSO_4$	9.4	5M NH_3	Brown	2.19
H-Y(30)[b]	0.05M V_2O_5	9	5M NH_3	Yellow and orange precipitate	

[a] The ion exchange was executed in autoclaves at 150°C
[b] The H-Y(30) was ion exchanged first for 24h two times, and then 5M NH_3 was added for 30min.

the pH is raised, some orange precipitate is observed. This can be seen in context with the phase diagram shown in figure 1.18 in which the pH is raised and then V_2O_5 is precipitated around pH≈2.[1] In figure 6.1 the ion exchange of ZSM-5(80) and ZSM-5(30) are shown.

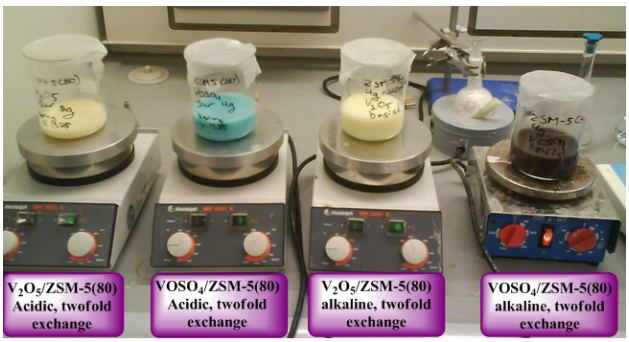

Figure 6.1: The ion exchange of H-ZSM-5(80) and H-ZSM-5(30).

The ion exchange that was executed in the autoclaves gave a quite different result than when it was stirred at room temperature. It is acknowledged that the metal content is increased when the ion exchange is done with thermal treament. When the pentavalent solution was taken out of the oven, it was transparent. This is most likely the ion VO_3^- which is a vanadate and is dependent on the pH and the vanadium concentration. If figure 1.18 is studied, the ion VO_3^- is the same as HVO_4^{3-}, which is dominant at pH=13-14 and with high vanadium concentration. If the pH had been taken after the hydrothermal treatment, the pH might have been higher. As it has been observed with the other ion exchanged zeolites, it took a while before the pH increased, therefore the pH has most likely increased in the oven.

6.2 A combined XAS/Raman *in situ* study on oxidation of propene over V_2O_5/ZSM-5 and V_2O_5/Y

The motivation to study oxidation of propene over V_2O_5/ZSM-5 and V_2O_5/Y was because vanadium is reported to exhibit activity towards the oxidation of propene.[15,14] By depositing particles of V_2O_5 on zeolites it can possibly be a bifunctional catalyst. The channels and cavities of the two zeolites respectively is as mentioned in section product selective and intermediate selective. As explained in section 1.3, there is a demand for more selective catalysts. V_2O_5/ZSM-5 and V_2O_5/Y was chosen to be investigated by combined Raman/XANES *in situ* study, as they had higher vanadium content than the other samples.

The colors of the ion exchanged V_2O_5/ZSM-5 was yellow to orange prior to calcination, as shown in figure 6.2. This in an indication of pentavalent vanadium, and the color of V_2O_5 is brick red to orange. After the sample was calcined, the color became bright yellow. By calcining the V_2O_5/ZSM-5 the idea was to sinter the possibly present V_2O_5 particles. For the ion exchanged zeolite Y, the color was yellow, and as mentioned this is an indication of pentavalent vanadium.

Elemtal analysis was done for the two ion exchanged samples and is shown in table 6.2. As the table show, the V_2O_5/ZSM-5 had the highest vanadium content followed by V_2O_5/Y. A regular ion exchanged ZSM-5 with a solution of V_2O_5 is shown to compare the effect of twofold ion exchange and the pH environment. Table 6.2 show that a twofold ion exchange dramatically increases the vanadium content.

The XRD diffractogram shown in figure 6.3, show no traces of V_2O_5. Thus if there were any V_2O_5 particles they were too small to be detected by the X-ray diffractometer.

Figure 6.2: A picture of the V_2O_5/ZSM-5 and V_2O_5/Y and bulk V_2O_5. The bulk $V-2O_5$ is shown to the left at the top. The as prepared V_2O_5/ZSM-5 is shown on the top to the left. The calcined V_2O_5/ZSM-5 is shown to the right from the top. The as prepared and calcined V_2O_5/Y is shown at the bottom left and right respectively.

Table 6.2: The vanadium content in V_2O_5/ZSM-5, V_2O_5/Y and V_2O_5:ZSM-5 found by ICP-MS.

Sample	Vanadium content wt%	RSD %
V_2O_5/ZSM-5	3,93	2
V_2O_5/Y	2,19	1,2
V_2O_5:ZSM-5	0,025	1,5

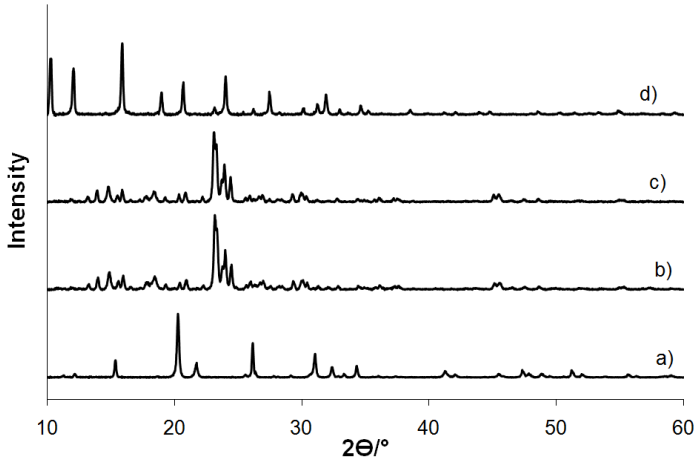

Figure 6.3: The X-ray diffractogram for a) Bulk V_2O_5, b) as synthesised V_2O_5/ZSM-5, c) calcined V_2O_5/ZSM-5, d) calcined V_2O_5/Y

6.2.1 Raman spectra of V_2O_5/ZSM-5 and V_2O_5/Y

The Raman spectra shown in figure 6.4,show that V_2O_5/ZSM-5 are similar to bulk V_2O_5.

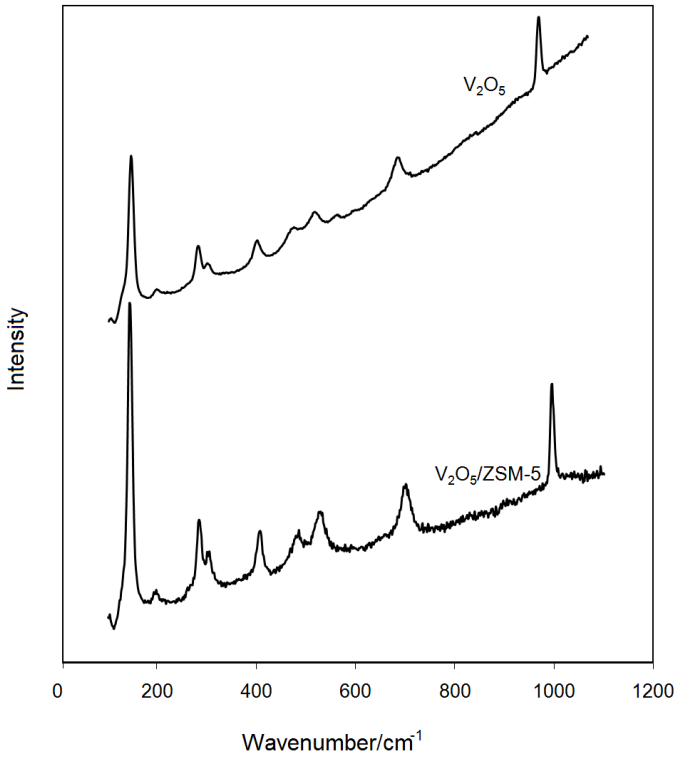

Figure 6.4: Raman of bulk V_2O_5 and V_2O_5/ZSM-5.

Table 6.3 show the Raman band of bulk V_2O_5 as a reference, and the V_2O_5/ZSM-5 at the different reaction stages. The V_2O_5/ZSM-5 was also compared when it was heated in helium. The Raman band at 174.83cm^{-1} is not present at room temperature, but it becomes apparant at 80°C in oxygen, it continues to increase at 135°C, and it disappears at 160°C The same peak is not present when the same sample was heated in helium. The Raman band at approximately 308cm^{-1} is not evident in the bulk V_2O_5. The Raman band at 999cm^{-1} can be assigned to the symmetric stretch of vanadyl groups in V_2O_5.[17] The peaks that are present in the bulk V_2O_5, but not in the sample is not reported in literature. Surface VO_4 is reported to have a band at

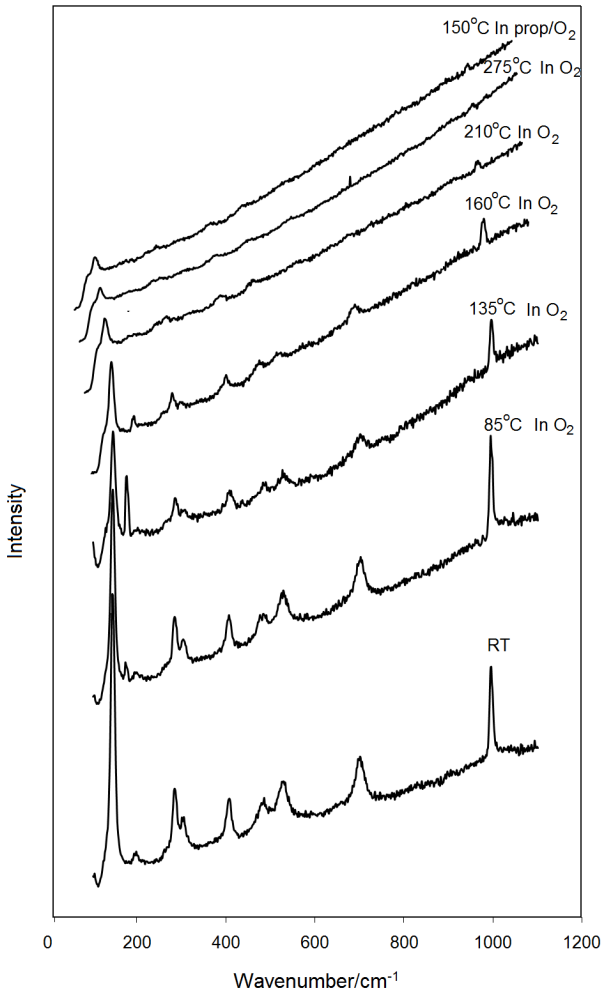

Figure 6.5: The Raman sepctra of the *in situ* measurement of V_2O_5/ZSM-5

1035 and 935/900cm^{-1} [16,17], although this is not reported here. It was not found out which vanadium species the band at 174cm^{-1} could be assigned to, as it was not reported in any articles. Although some have claimed that Raman spectroscopy may not be reliable for discriminating monomeric and polymeric vanadyl species, it still can be used to identify crystalline V_2O_5.[17]

The same procedure for the *in situ* measurement was done for $VOSO_4$/Y. In figure 6.7 the Raman spectra for the measurement is illustrated. As the

Table 6.3: The Raman bands for V_2O_5/ZSM-5 compared with the bulk V_2O_5

Peak Position/cm^{-1}						
bulk V_2O_5	RT	80°C in O_2	135°C in O_2	160°C in O_2	RT in He	504°C in He
147.21	144.84	144.77	145.42	146.63	148.93	148.54
		174.83	176.58			
200.77	195.74	198.97		198.34	200.46	200.72
						266.65
287.17	284.52	284.14		286.79	287.83	287.84
	303.66	304.11			308.07	308.225
409.88	405.47	405.35		408.18	408.58	408.57
483.75	482.06	479.65		484.18	485.499	484.22
531.14	527.03	527.10		527.14	530.81	530.31
575.63						
702.73	699.95	699.74		702.31	705.06	704.23
999.72	996.41	995.63		997.886	999.036	998.83

Table 6.4: The Raman bands of V_2O_5/Y, bulk V_2O_5/ $VOSO_4$

Peak position			
bulk $VOSO_4$	bulk V_2O_5	RT	40°C in O_2
123.913	147.21		
154.816	200.766		
		264.084	266.29
213.31	409.883		
279.54	483.75	492.55	488.14
320.37	531.14	509.11	509.11
478.20	702.73		703.36
649.28	999.72		
1004.67			
1027.85			
1074.21			

figure show, the Raman in room temperature does not resembles neither bulk V_2O_5 or $VOSO_4$. When the sample was heated in oxygen, some of the peaks that are evident in bulk V_2O_5 arised on the sample. The Raman bands at 264.08cm^{-1} for room temperature and heating in O_2 is not part of the characteristic peaks for bulk V_2O_5.

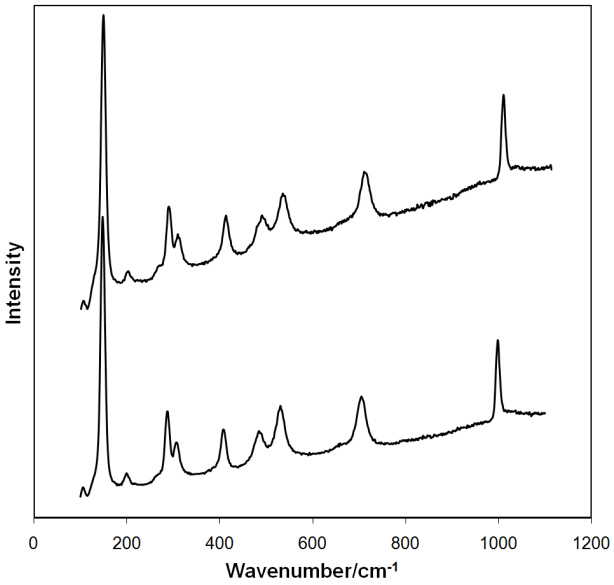

Figure 6.6: Raman spectra of V_2O_5/ZSM-5 when heated in helium.

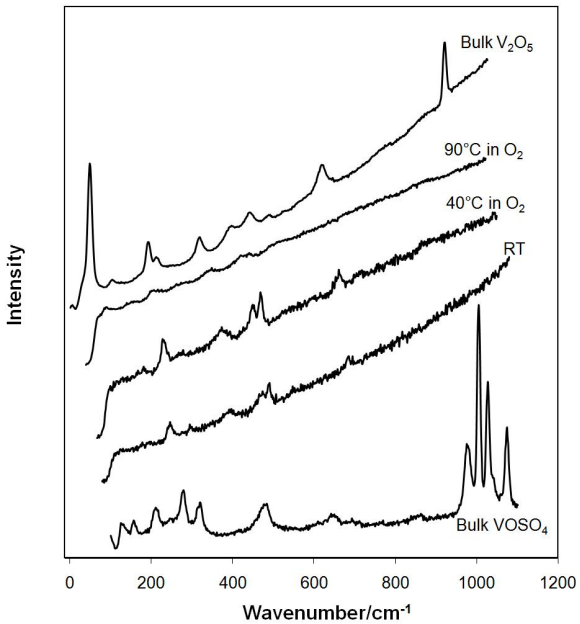

Figure 6.7: The Raman spectra of V_2O_5/Y heated in O_2

6.2.2 XAS investigation of V_2O_5/ZSM-5 and V_2O_5/Y

In situ XANES was collected simultaneously as Raman and mass spectra. First the V_2O_5/ZSM-5 sample was investigated in prop/O_2 flow. According to the redox cycle the catalyst should be reduced during the flow of propene and oxygen, which should be evident in the XANES. Figure 6.9 show that during the oxidation of propene the XANES did not show any pronounced alteration in the oxidation state. To distinguish the different XANES scan, it was nescessary to study the pre-edge as the edge had too much noise. It has been shown earlier in section 3.2.2 that the pre-edge area linearly decreases with decreasing oxidation state. The pre-edge area were calculated and is illustrated in figure 6.9. The peak fit results as also shown in table 6.5, show that the pre-edge area decreases in heating in oxygen. When the sample is heated in prop/O_2, the pre-edge area increases. The pre-edge area decreases and then increases on further heating with prop/O_2.

As the XANES data were collected, the reducibilty were not visible. Therefore the same sample was treated with hydrogen while XANES and Raman data were collected. Figure 6.9 show the XANES for V_2O_5/ZSM-5 heated in hydrogen. As seen with heating in oxygen the pre-edge area is decreased when heating in helium. When the sample was further heated in hydrogen the pre-edge area increased and at 450°C it decreased. The pre-edge refinements are shown in table 6.5. As the table show the pre-edge position is approximately the same for all the reaction stages.

Temperature programmed reduction was done on the sample to investigate the reducibility, as seen in figure 6.8. The temperature programmed reduction does not show a decrease in the hydrogen curve, which means it is not absorbed by the sample. Some water is lost before 100°C.

The decrease in the pre-edge area when the sample was heated in oxygen could be seen in context with the theory shown in section 1.9.1. The pre-edge feature in bulk V_2O_5 has been assigned to the dipole transition of the hybridisised orbital 3dV-2pO. When the pre-edge is decreased in the pres-

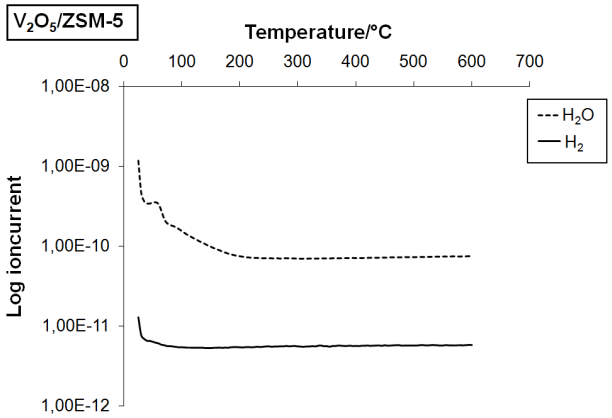

Figure 6.8: The temperature programmed reduction in the presence of hydrogen for V_2O_5/ZSM-5.

ence of oxygen, the change in oxygen state is excluded. The most likely assumption is that as oxygen flows over $V_2O{-}5$/ZSM-5 it is bonded to the surface, and breaks the double bond, which results in a larger molecular cage. Thereby a smaller pre-edge area. As mentioned in section 1.9.1 the smaller the molecular cage (interaction with the ligand), the larger the intensity on the pre-edge.The pre-edge is also sensitive to the local geometry, and by introducing oxygen to the V_2O_5/ZSM-5, it could also change the geometry, for reasons mentioned above, and thereby reducing the 3dV-2pO mixing.

When the pre-edge area is increased during the flow of prop/O_2 the original bond arrangement might be partially restored. It does not restore its original form, since the pre-edge area is slightly lower than in room temperature. The reaction mechanism proposed under section 1.3.3 show that propene is oxidised, and the catalyst is reduced by losing an oxygen atom. Since the rate limiting step is the formation of the allyl intermediate (the surface reaction), the reduction happens too quicly to give a good indication of the redox mechanism. Although as the in situ measurement progressed, according to the peak fit analysis, it seems as if vanadium reduces and oxidises. This is in accordance with the redox mechanism.

Figure 6.10 show the in situ XANES measurement in prop/O_2 over V_2O_5/Y. The pre-edge area is decreased in heating in oxygen to 90°C. When the

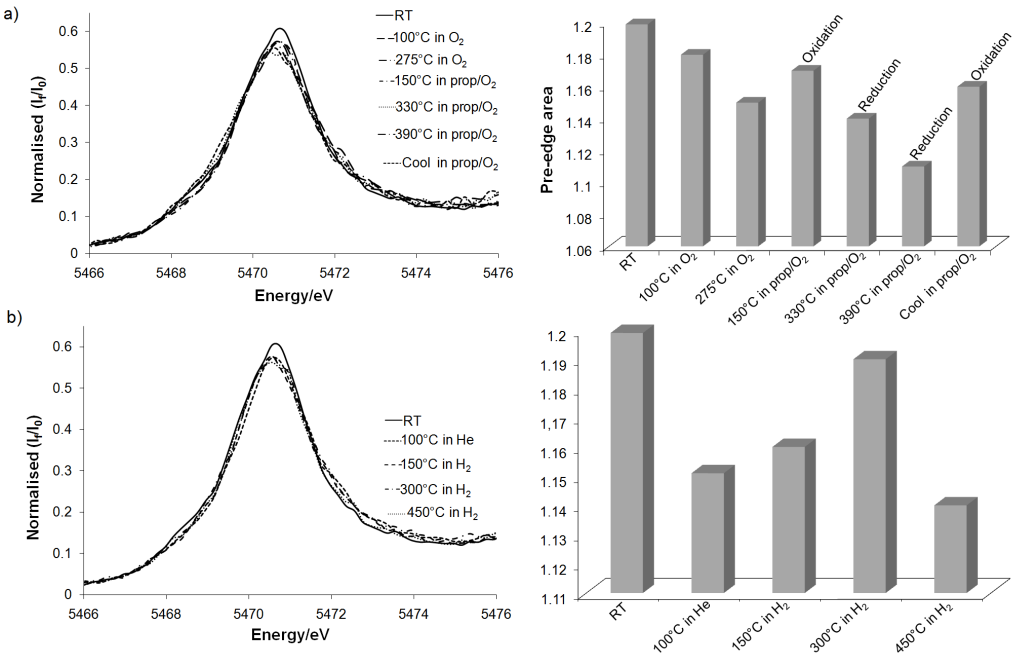

Figure 6.9: The XANES measuremnt for a) V_2O_5/ZSM-5 in propene and oxygen and b) V_2O_5/ZSM-5 in hydrogen.

sample is further heated in oxygen to 272°C the pre-edge area increases and seems stable throughout the rest of the in situ experiment. By studying table 6.5, it shows that when the sample is further heated in oxygen, the pre-edge are is slightly increased, but not as pronounced as it appear from the bar chart.

Temperature programmed reduction was also done for V_2O_5/Y, to investigate the reducibility in hydrogen, as this was not done *in situ* as for V_2O_5/ZSM-5. The temperature programmed reduction is shown in figure 6.11. As also shown for V_2O_5/ZSM-5, there is no uptake of hydrogen.

The *in situ* XANES of V_2O_5/Y does show the same feature as observed for V_2O_5/ZSM-5, where the pre-edge is decreased when it is heated in oxygen. Although the pre-edge is slightly increased in further heating in oxygen, this can be assigned to the size of the particles as mentioned under section 6.2.1. Smaller particles may behave differently.

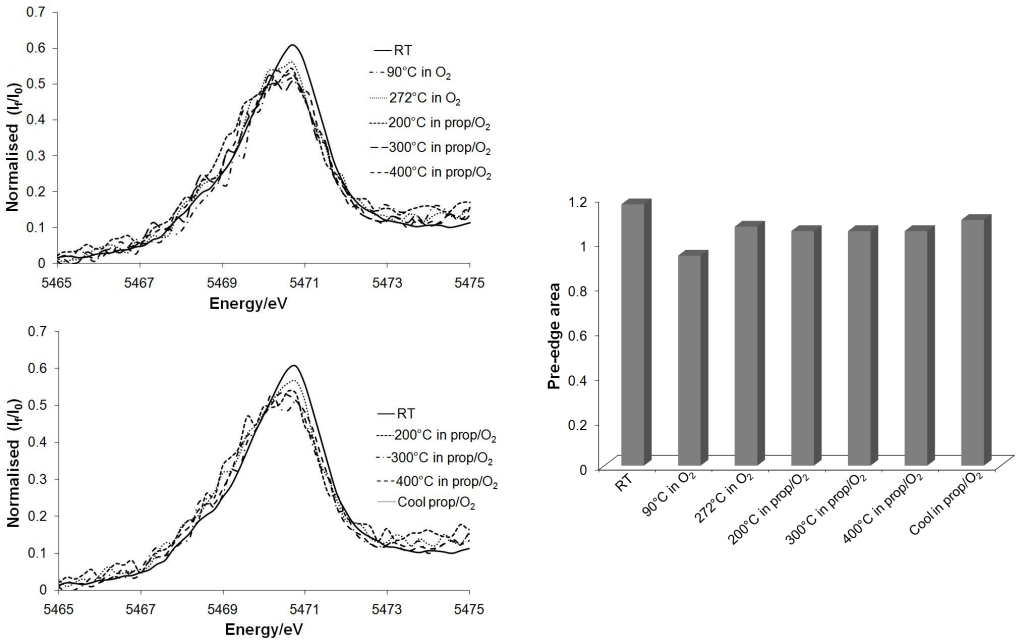

Figure 6.10: The *in situ* measurement for the sample V_2O_5/Y with heating in oxygen and propene, and then cooling in propene.

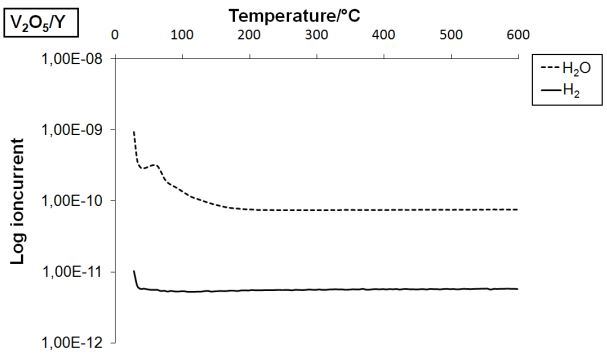

Figure 6.11: The temperature programmed reduction in H_2 for V_2O_5/Y

The EXAFS refinements is shown in table 6.6 and in figure 6.12. As seen in the table the first bond distance of approximately 1.63Å, is mutual for all of the samples. The bond dinstance of the as synthesised V_2O_5/ZSM-5 second shell is 2.31Å, and after it was calcined the bond distance had decreased to 1.84Å. The as synthesised V_2O_5/Y has a bond length of 1.87Å on the second shell, and it is not further deacreased if the uncertainty is taken into account.

The first shell has a bonding distance that corresponds to the double bond in V_2O_5, however table 6.6 show that the mulitplicity of the first shell is

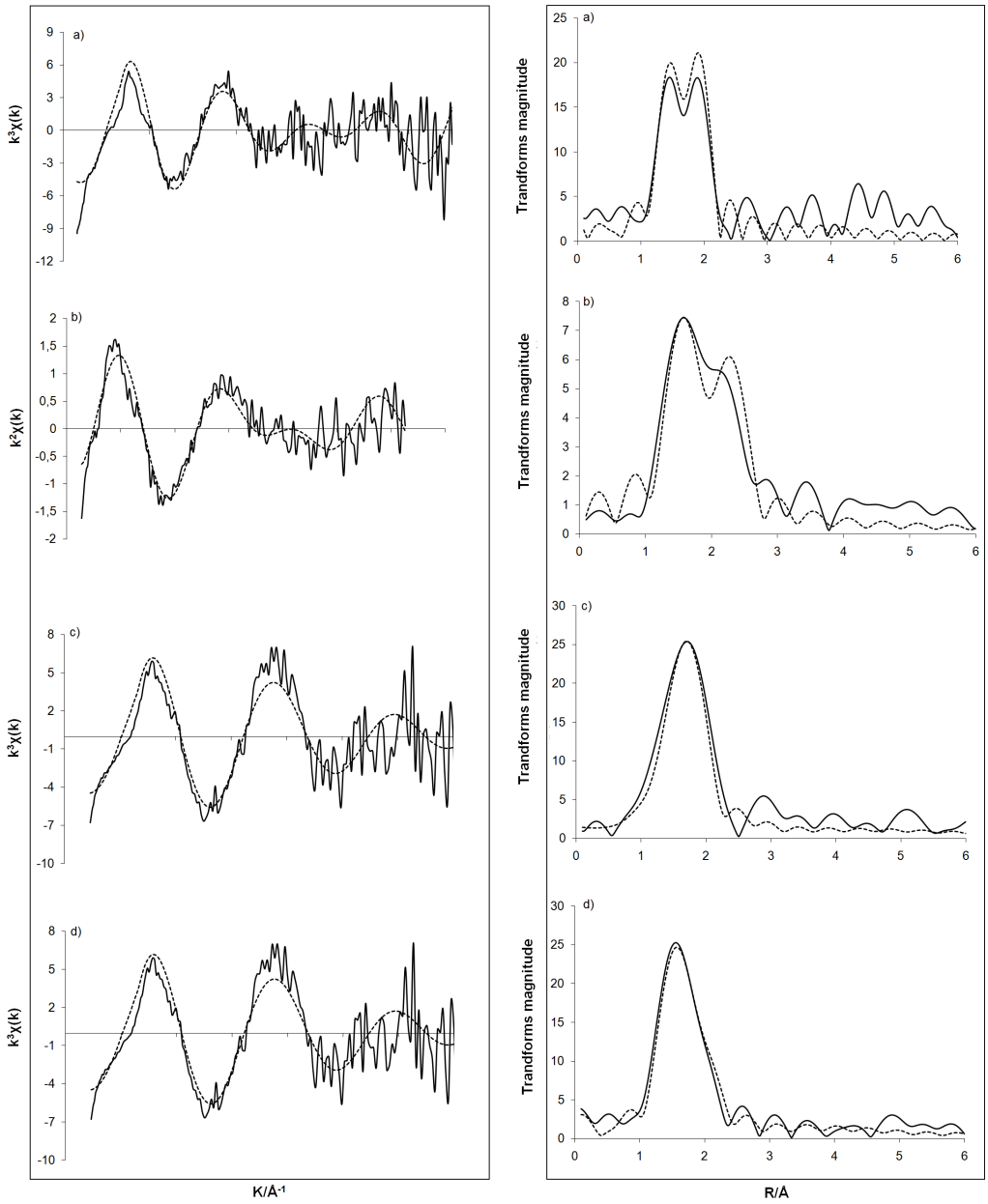

Figure 6.12: Experimental (-) and calculated (···) k^3 and k^2 weighted EXAFS and its Fourier Transform for a) calcined V_2O_5/ZSM-5 k=2-11, b) as synthesised V_2O_5/ZSM-5 k=3-10, c) calcined V_2O_5/Y k=2-9, d) as synthesised V_2O_5/Y k=2-9

To compare the Fourier transform of bulk V_2O_5 with the as synthesised and calcined V_2O_5/ZSM-5. It is seen that the bond lengths of the two first shells of bulk V_2O_5 is the same as for the calcined V_2O_5/ZSM-5, although the rest of the Fourier transform is not similar. To observe particles in the EXAFS it must be observed V-V distances, otherwise they are not observed by EXAFS. As seen in table 6.6 no V-V distances were observed, which means that V_2O_5 particles was not observed with EXAFS.

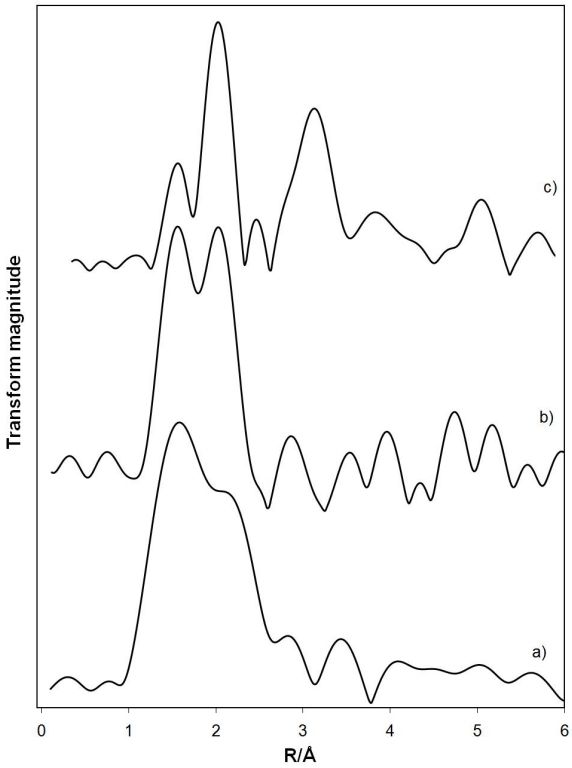

Figure 6.13: The Fourier transform of a) as synthesised V_2O_5/ZSM-5, b) calcined V_2O_5/ZSM-5, c) bulk V_2O_5

The EXAFS results show that vanadium has the bond distance of approximately 1.63Å for the samples. This could be assigned to the double bond, that is reported to have bond lenth of 1.58Å in bulk V_2O_5. However the multiplicity is $\geq$1, and chemically the vanadium should only have one double bond. This was investigated in EXCURVE98. The AFAC was set to

1, and the Debye-Waller was still constant. The parameters were refined, and revealed a mutiplicity of 1 for the first shell. This corresponds to the double bond seen in V_2O_5. The second shell where the bond length is approximately 1.85Å has a multiplicity of approximately 3, which is also found for bulk V_2O_5 in the EXAFS refinements in section 3.3.1.

Table 6.5: The pre-edge refinements on V_2O_5/ZS-5 in prop/O_2 and H−2

Sample	Reaction stage	Pre-edge centroid	Pre-edge area	R-factor
V2O5/ZSM-5	RT	5470.6(1)	1.2(0)	0.00219
	100°C in O_2	5470.6(1)	1.18(4)	0.00222
	275°C in O_2	5470.6(1)	1.15(5)	0.00315
	150°C in prop/O_2	5470.6(1)	1.17(5)	0.00248
	330°C in prop/O_2	5470.5(1)	1.14(5)	0.00226
	Cool in prop/O_2	5470.5(1)	1.16(4)	0.00226
	100°C in He	5470.7(1)	1.15(4)	0.00182
	150°C in H_2	5470.6(1)	1.16(4)	0.00185
	300°C in H_2	5470.6(1)	1.19(4)	0.00217
	450°C in H_2	5470.6(4)	1.14(4)	0.00174
V_2O_5/Y	RT	5470.4(1)	1.17(5)	0.00317
	90°C in O_2	5470.4(1)	0.94(1)	0.00279
	272°C in O_2	5470.3	0.97(3)	0.00327
	200°C in prop/O_2	5470.1(2)	1.05(6)	0.0034
	300°C in prop/O_2	5470.2(2)	1.05(6)	0.00391
	400°C in prop/O_2	5470.2(2)	1.05(6)	0.00381
	Cool in prop/O_2	5470.2(2)	1.10(6)	0.00341

Table 6.6: Paramters from the least square EXAFS analysis by using AFAC 0.53 calculated by the model compound V_2O_5

Sample	Shell	N	R/Å	$2\sigma^2$/Å^{2a}	Ef/eV	R/%
V_2O_5/ZSM-5 as synthesised	V-O	2(2)	1.63(2)	0.0003	13(2)	43.13
	V-O	3.8(7)	2.31(3)	0.0003		
V_2O_5/ZSM-5 calcined	V-O	2.4(4)	1.63(2)	0.0003	2(2)	54.15
	V-O	1.6(2)	1.84(2)	0.0003		
$VOSO_4$/Y as synthesised	V-O	3.2(3)	1.67(2)	0.0003	0(1)	34.64
	V-O	2.8(3)	1.87(2)	0.0003		
$VOSO_4$/Y calcined	V-O	2.0(4)	1.63(4)	0.0003	1(2)	43.53
	V-O	3.1(6)	1.80(3)	0.0003		

[a] The Debye-Waller factor was set to 0.0003 because it always became negative, when the data was refined. This value is according to the article Characterization of Metal-Incorporated Molecular Sieves[53]

6.2.3 Mass spectra

Results from the mass spectra of V_2O_5/ZSM-5 revealed that acrolein was formed during the reaction, which is shown in figure 6.14. As seen in the figure, when acrolein was no longer formed, the CO_2 increased dramatically. The mass spectra of V_2O_5/Y showed no acrolein formation. The increase in the propene is because the gases reached the sample. When the gases flowed over the sample between cycle 7000-20000, CO_2 was formed along with the propene content. The color of the two samples after the experiment was black. Due to the mass spectrometer acrolein with an extra proton was observed.

The duration of the formation of acrolein over V_2O_5 was limited, and this is explained by a simple observation. As the color of V_2O_5/ZSM-5 had become black, it indicates that the sample coked. The coke blocked the active sites, thus the increase in the CO_2 over V_2O_5/ZSM-5 show complete oxidation. V_2O_5/Y show complete oxidation when the gases enters the sample. V_2O_5/Y also lead to coke formation, however there is no indication when this ocurred, since the complete oxidation ocurred when the gas entered the sample.

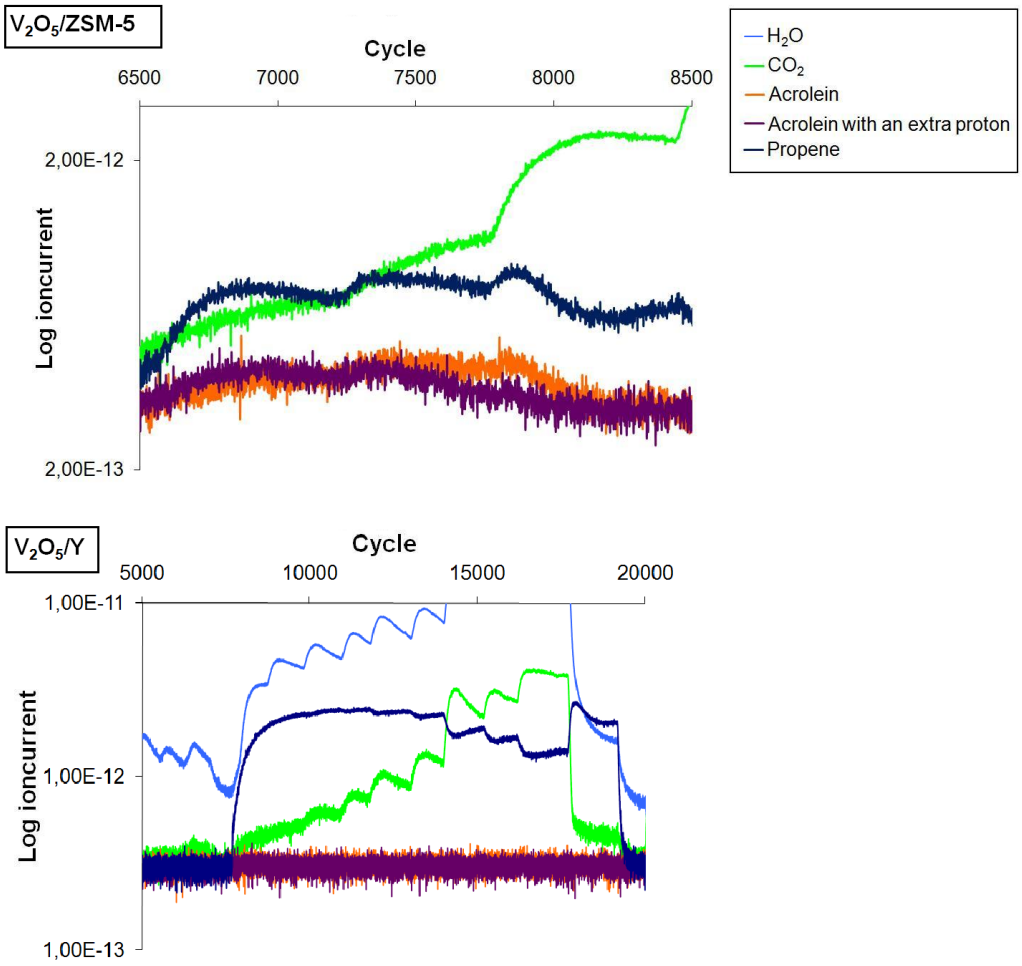

Figure 6.14: The mass spectra during the in situ experiment in prop/O_2 flow

6.2.4 Summary

It is possible to deposit V_2O_5 particles onto zeolites by ion exchange with VO^{2+} and $VO_2{}^+$ solutions which is described under section 5.1 in an alkaline environment. The V_2O_5/ZSM-5 catalyst is active towards the formation of acrolein, as seen from the mass spectra. The V_2O_5/Y sample did not show formation of acrolein, on the contrary it went straight to complete oxidation. This can be seen in relation with the type of support as ZSM-5 and Y has different structural properties. The particles could be trapped inside the supercage of the zeolite Y, when they are sintered, since the pore opening is smaller. Thereby the particles are not able to be excited. This can lead to pore blockage, and this could be a reason for V_2O_5/Y does not form acrolein. ZSM-5 it has straight channels which make it possible for the particles to travel to the surface of the zeolite, when they are sintered. It could also be the preparation of the samples, since they were prepared differently, they are not completely comparable. It could also be the size of the particles, as seen in the Raman spectra in figure 6.4 and 6.7. Raman detects crystalline V_2O_5 on V_2O_5/ZSM-5. The V_2O_5/Y sample does not show the distinct peaks for crystalline V_2O_5 in the beginning of the in situ experiment, as it is heated, some of the peaks that are detected in V_2O_5 becomes evident. This is explained as the V_2O_5 particles in V_2O_5/Y might be very small, as they are heated they agglomerates, and displays in the Raman spectra. The EXAFS does not detect V_2O_5 particles, and it does not show up on the X-ray diffractogram, however they appear in the Raman spectra. Hence Raman is more sensitive towards the small nanoparticles, which proves the importance of Raman in experiments like this.

Chapter 7

Concluding remarks: Characterisation of V_2O_5/ZSM-5 and V_2O_5/Y

- By ion exchange of H-ZSM-5 and H-Y with solutions of vanadium in an alkaline environment. It is possible to deposit $V_{2}o_{5}$ particles onto H-ZSM-5 and H-Y.
- XRD and EXAFS did not show the reosence of V_2O_5 particles, however they were detected by Raman. Thus Raman is more sensitive for detecting small particles.
- The combined Raman/XANES *in situ* experiment for the oxidation of propene showed that V_2O_5/ZSM-5 produced acrolein. V_2O_5/Y did not produce acrolein, and the reaction lead to complete oxidation at once the gas mixture reached the sample.

Chapter 8

Future work

This work consist, as mentioned, of two parts. The first part mainly focused on the synthesis and characterisation of VAPO-5 and VAPSO-5. The second part is focused on V_2O_5 particles on zeolites for the oxidation of propene. As showed in Section 3.5 the VAPO-5 and VAPSO-5 is not desirable catalysts for the reduction of NOx. However they should be investigated as catalysts for oxidation of hydrocarbons for the oxidation catalysts, as they are reported to have good activity for oxidation of hydrocarbons.[4]

The synthesis of VAPSO-5 should be further investigated, as the VAPSO-5\4(IV) showed a high vanadium content according to what was added in the synthesis. However the vanadia loading could no be increased due to instability of the structure. Therefore the synthesis conditions should be investigated, to increase the vanadia loading in VAPSO-5, when the silicon content is high. Since it has been reported that VAPO-5/VAPSO-5 as catalysts increses its activity with increased vanadium content.[62]

The V_2O_5/ZSM-5 and V_2O_5/Y should be further investigated to find out what the activity for the oxidation of propene is depended upon. They should also be further investigated to find out the particle sizes. Increased vanadia loading could be correlated with the activtiy for the oxidation of propene.

Bibliography

[1] R.J.H. Clark. *Comprehensive inorganic chemistry.* Pergamon Press, first edition edition, 1973.

[2] J.A. Dumesic N.Y Topsøe, H. Topsøe. Vanadia/titania catalysts for selective catalytic reduction (scr) of nitric oxide by ammonia. *Journal of Catalysis*, 151:226–240, 1995.

[3] Larry Kevan Martin Hartmann. Transition metal ions in aluminophosphate and silicoaluminophosphate molecular sieves: Location, interaction with adsorbates and catalytic properties. *American Chemical Society*, 1999.

[4] Zhongmin Liu Zhaochi Feng Qin Xin Can Li Joanqiang Yu, Meijun Li. Comparative study of the vanadium species in vapo-5 and vapso-5 molecular sieves. *Journal of Physical Chemistry*, 2002.

[5] Costas Pliangas Susanne Brosda Demetrois Tsiplakides Costas G. Vayenas, Symeon Bebelis. *Elechtrochemical Activation of Catalysis-Promotion, Elechtrochemical Promotion and Metal Support Interaction.* Springer-Verlag, 2001.

[6] U.S Environmental Protection Agency. Health and environmental impacts of nox. `http://www.epa.gov/air/urbanair/nox/hlth.html`, 2008.

[7] State of Environment Norway. Gøteborgprotokollen. `http:`

//www.miljostatus.no/Tema/Luftforurensning/Sur-nedbor/Goteborgprotokollen/, 2009.

[8] A. Guerro-Ruiz G.L. Haller M. Fernàndez-Garcìa C. Màrquez-Alvarez, I. Rodriquez-Ramos. *J.Am.Chem.Soc.*

[9] J. Weitkamp Y. Traa, B. Burger. *Micr. and Mes.Mat.*

[10] R.K. Grasselli. Fundamental principles of selective heterogeneous oxidation catalysis. *Topics in Catalysis*, 21:79–88, 2002.

[11] E. Ruckenstein D.B. Dadyburjoer, S.S. Jewur. Selective oxidation of hydrocarbons on composite oxides. *Catalysis Reviews*, 19:293–350, 1979.

[12] A. Holmen. *Heterogen katalyse.* Institutt ofr kjemisk prosessteknologi, 2006.

[13] Jonathan Rourke Mark Weller-Fraser Armstrong Peter Atkins, Tina Overton. *Inorganic Chemistry.* Oxford University Press, 2006.

[14] I.E. Wachs C. Zhao. An operando raman, ir, and tpsr spectroscopic investigation of the selective oxidation of propylene to acrolein over a model suported vanadium oxide monolayer catalyst. *Journal of Physical Chemistry*, 112:11363–11372, 2008.

[15] L. Savary J.C. Lavalley M.M. Bettahar, G. Costentin. Review on the partial oxidation of propane and propylene on mixed metal oxide catalysts. *Applied Catlysis A: General*, 145:1–48, 1996.

[16] I.E. Wachs C. Zhao. Selective oxidation of propylene over model supported v_2o_5 catalysts: Influence of surface vanadia coverage and oxide support. *Journal of Catalysis*, 257:181–189, 2008.

[17] M. Pinault C. Wang-F. Fang L. Pfefferle G.L. Haller G. Du, S. Lim. Synthesis, characterisation, and catalytic performance of hughly dispersed vanadium grafted sba-15 catalyst. *Journal of Catalysis*, 253:74–90, 2008.

[18] R.R. Rosin A.T. Bell G.T. Went, L.J. Leu. The effects of structure on the catalytic activity of v_2o_5/tio_2 for reduction of no by nh_3. *Journal of Catalysis*, 134:492–505, 1992.

[19] Pingyun Feng Yang Peidong, Xianhui Bu. *Chemistry of Nanostructure Material*. World Scientific, 2003.

[20] A.Dyer. *Zeolite Molecular Sieves*. John Wiley and Sons, 1988.

[21] A.K. Sengupta S. Sengupta. *Encycploaedia of Chemical Processing*. Taylor and Francis, 2006.

[22] M.E. Davis. What are Zeolites?

[23] G.L. Price. Faujasite-AKA Zeolite Y.

[24] S. Bahtia. *Zeolite Catalysis Principles and Application*. CRC Press, 1990.

[25] H. van Bekkum M.S. Rigutto. Vanadium site in vapo-5: Characterization and catalytic properties in liquid-phase alkene epoxidation and benzylic oxidation. *Journal of Molecular Catalysis*, 81:77–98, 1993.

[26] R.M. Krishna Z. Chang, R. Koodali and L.Kevan. Photoinduced charge separation of methylphenothiazine in vanadium- and titanium-containing alpo-5 and alpo-11. *J.Phys.Chem*, 104:5579–5585, 2000.

[27] C.J Lai K.J. Chao A. C. Wei J. F. Lee H.Y.Cheng, E.Yang. Density functional theory calculation and x-ray absorption spectroscopy studies of structure of vanadium.containing aluminiumphorphate vapo-5. *Journal of Physical Chemistry*, 104:4195–4203, 2000.

[28] H.B. Gray C.J. Ballhausen. The electronic strucutre of the vanadyl ion. *Inorg.Chem.*, 1:111–122, 1962.

[29] B.M. Weckhuysen D.E. Keller and D.C. Koningsberger. Application of axafs spectroscopy to transition-metal oxides: Inluence of the nearest and next nearest neighbour shells in vanadiun oxides. *Chem.Eur.J*, 13:5845–5856, 2007.

[30] Jim Clark. Vanadium. http://www.chemguide.co.uk/inorganic/transition/vanadium.html, 2003. Chemguide- Helping you understand chemistry.

[31] Metha-Synthesis Cooperation. Chemical enity data page. http://www.chemthes.com/entity_datapage.php?id=4001, 1999–2009.

[32] R.P. Messmer D.H. Maylotte J. Wong, F.W. Lytle. K-edge absorption spectra of selected vanadium compounds. *Physical review B*, 30:5596–5610, 1984.

[33] A.C. Wei and K.J. Chao. Structural characterisation of metal ions incorporated in molecular sieve frameworks. *J.Ch.Chem.Soc*, 47:33–40, 2000.

[34] Brendan Murray Mysore Narayana Consuelo Montes, Mark E. Davis. Isolated redox centers within microporous environments. 2. vanadium-containing aluminophosphates molecular sieve five. *Journal of Physical Chemistry*, 94, 1990.

[35] Mark T. Weller. *Basic crystallography, Inorganic Materials Chemistry.* Oxford University Press, 1994.

[36] Boon K.Teo. *EXAFS:Basic Principles and Data Analysis.* Springer-Verlag Berlin Heidelberg New York Tokyo, 1986.

[37] Matt Nevwille. Xafs: X-ray absorption fine-structure. http://cars9.uchicago.edu/xafs/NSLS_2002/Newville.pdf, 2002.

[38] Douglas P. Hoffmann David M. Hercules Martin J. Fay, Andrew Proctor. Unravelling exafs spectroscopy. *Anal.Chem*, 60:1225–1243, 1988.

[39] T.Yamamoto. Assignement of pre-edge peaks in k-edge x-ray absorption spectra of 3d transition metal compounds: electric dipole or quadrupole? *X-Ray Spectrom.*, 37:572–584, 2008.

[40] S.R.Bare. Xanes measurements and interpretation. http://cars9.uchicago.edu/xafs/APS_2005/Bare_XANES.pdf, 2005.

[41] P. Brant S.D. George and E. Solomon. Metal and ligand k-edge xas of organotitanium complexes: Metal 4p and 3d contributions to pre-edge intensity and their contributions to bonding. *J.Am.Chem.Soc*, 127:667–674, 2005.

[42] D.K. Misemer S. Doniach K.O. Hodgson F.W. Kutzler, C.R. Natoli. Use of one-electron theory for the interpretation of near edge structure in k-shell x-ray absorption spectra of transition metal complexes. *J.Chem.Phys.*, 73:5596–5610, 1980.

[43] G.E. van Dorssen D.C. Koningsberger, B.L. Mojet and D.E. Ramaker. Xafs spectroscopy; fundamental principles and data analysis. *Topics in Catal.*

[44] M. Newville B. Ravel. Athena, artemis, hephaestus: data analysis for x-ray absorption spectroscpy using ifeffit. *Journal of Synchrotron Radiation*, 2005.

[45] N.Hearn J.Skalny. *Handbook of Analytical Techniques in Concrete Science Technology.*

[46] F.J. Holler S.R. Crouch D.A. Skoog, D.W. West. *Fundamentals of Analytical Chemistry.* Brooks/Cole, 2004.

[47] V.S. Ramachandran. *Handbook of Analytical Techniques in Concrete Science Technology.*

[48] S. Cradock E.A.V. Ebsworth, D.W.H. Rannkin. *Structural Methods in Inoragnic Chemistry.*

[49] J.Clark. The Mass Spectrometer, 2000.

[50] R.M. Silverstein, F.X. Webster, and J.K. Kiemle. *Spectrometric Identification of Organic Compounds.* Wiley and Sons, INC.

[51] V.N. Shetty N. Venkatathri. *Catal.Comm.*

[52] M. Stockenuber K.Mathisen and D. Nicholson. In situ xas and ir studies on cu:sapo-5 and cu:sapo-11: the contributory role of monolinear copper (i) species in the selective catalytic reduction of nox by propene. *Phys.Chem.Chem.Phys*, 2009.

[53] H.C. Wu J.F. Lee K.J. Chao, A.C. Wei. Characterization of metal-incorporated molecular sieves. *Catalysis Today*, 49:277–284, 1999.

[54] A.N. Fitch M. Stockenhuber K.Mathisen, D.G. Nicholson. Selective catalytic reduction of NOx over microporous cuapo-5: structural characterisation by xas and xrd. *J.Mater.Chem.*, 15:204–217, 2005.

[55] Robert A. Schoonheydt Bert M. Weckheysen, Ina P. Vannijvel. Chemistry and spectroscopy of vanadium in vapo-5 molecular sieves. *Zeolites*, 15:482–489, 1995.

[56] W.M. Baker M. Balasubramanian J. McBreen A.N. Mansour, P.H. Smith. In situ xas investigation of the oxidation state and local structure of vanadium in discharged and charged v_2o_5 aerogel cathodes. *Electrochemica Acta*, 47:3151–3161, 2002.

[57] R.J. Arnott J.M. Longo. Structure and magnetic properties of $voso_4$. *Journal of Solid State Chemistry*, 1:394–398, 1970.

[58] T. Liese M.Wark, A. Brückner and W. Grünert. Selective catalytic reduction of no by nh_3 over vanadium-containing zeolites. *J.Catal.*, 175:48–61, 1998.

[59] N. Morgante S.Cristol C.R.A. Catlow J.M. Thomas G.N. Greaves F.Meneau, G. Sankar. Characterisation of zinc oxide nanoparticles encapsulated into zeolite-y: An in-situ combined x-ray diffraction, xafs, and saxs study. *Nucl.Instr. and Meth. in Phys. Res. B*, 199:499–503, 2003.

[60] T. Romotowski J. Komorek and E.M. Serwicka. Zsm-5 zeolite modified with vanadyl ions. *Zeolites*.

[61] Metha-Synthesis Cooperation. Chemical enity data page. `http://www.chemthes.com/entity_datapage.php?id=4002`, 1999–2009.

[62] H.O. Pastore A.A.Teixeira-Neto, L.Marchese. Vanadium-modified Molecular Sieves: Preparation, Characterization and Catalysis. *Quim.Nova*, 32:463–468, 2009.